

**AUTOMATED NANOMATERIAL INTEGRATED  
REPAIR PATCH PRODUCTION AND ITS  
IMPLEMENTATION FOR CARBON FIBER -  
REINFORCED COMPOSITES**

**by**

**HİLAL ŞENUYSAL**

**Submitted to  
the Graduate School of Engineering and Natural Sciences  
in partial requirements for the degree of  
Master of Science**

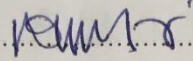
**SABANCI UNIVERSITY**

**July 2018**

AUTOMATED NANO MATERIAL INTEGRATED REPAIR PATCH PRODUCTION  
AND ITS IMPLEMENTATION FOR CARBON FIBER REINFORCED COMPOSITES

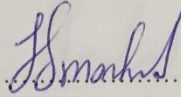
APPROVED BY:

Prof. Dr. Mehmet Yıldız

.....

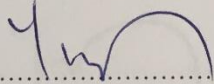
(Thesis Supervisor)

Dr. Jamal Seyyed Monfared Zanjani

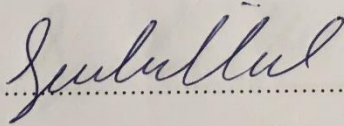
.....

(Thesis Co- Supervisor)

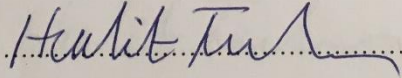
Prof. Dr. Yusuf Ziya Mencelođlu

.....

Asst. Prof. Serkan Ünal

.....

Prof. Dr. Halit Süleyman Türkmen

.....

DATE OF APPROVAL: 24.07.2018

© Hilal Şenuysal 2018

All Rights Reserved

## **ABSTRACT**

### **AUTOMATED NANO MATERIAL INTEGRATED REPAIR PATCH PRODUCTION AND ITS IMPLEMENTATION FOR CARBON FIBER REINFORCED COMPOSITES**

**HİLAL ŞENUYSAL**

Materials Science and Nano Engineering, M.Sc. Thesis, July,2018

Thesis Supervisor: Prof. Dr. Mehmet Yıldız

Co- Supervisor: Dr. Jamal Seyyed Monfared Zanjani

Keywords: Carbon Fiber Reinforced Composites, Graphene, Electrospraying, Repair Patch,  
Tapered Sanding, Acoustic Emission

Fiber reinforced composites are commonly preferred as primary and secondary structures in aerospace, energy, automotive industries due to its superior structural properties and lightweight. However, composite materials have certain limitations such as low impact resistance, delamination strength, fracture toughness and repairability. This study puts forward the applicability and the striking improvements in mechanical properties which provided by graphene in the composites.

The first chapter of this thesis includes a brief literature overview for nano-reinforcement of composite materials. In the second chapter, three different nano-material integrated arrangements were investigated. These systems can be categorized as the nano-reinforcement integration on the fibers, in the matrix, and both the fibers and the matrix. Notable enhancements were achieved in flexural, tensile and fracture toughness of the graphene-integrated composite structures, and microscopy images for the fracture surfaces are provided to support these results.

The third chapter presents comprehensive information on the design of the electro spraying device with multiple nozzles and its manufacturing processes. Electro spraying is a highly efficient method in nano-material coating field, which is fast, user-friendly and low-cost. The new multiple-nozzle electro spraying device is aimed to lead the nanomaterial integration for the mass production in the composite technologies research center.

In the last chapter, outcomes of the previous studies on TEGO integration on composites were used for the development of composite repairs. Repairing procedures were employed as matrix and interface reinforced repair patches. Two different sanding methods were tested to find the most efficient method. Shear properties of the repair patches were remarkably improved because of the interface and matrix modification with graphene-implementation.

To conclude, graphene as a reinforcer was successfully employed for the improvement in mechanical properties of healthy and repaired composite structures.

# ÖZET

## OTOMATİK NANO MALZEME TAKVİYELİ TAMİR YAMASI ÜRETİMİ VE KARBON FİBER-TAKVİYELİ KOMPOZİTLERE UYGULANMASI

HİLAL ŞENUYSAL

Malzeme Bilimi ve Nano Mühendisliği, Yüksek Lisans Tezi, Temmuz, 2018

Tez Danışmanı: Prof. Dr. Mehmet Yıldız

Yardımcı Danışman: Dr. Jamal Seyyed Monfared Zanjani

Anahtar Kelimeler: Karbon Fiber Takviyeli Kompozitler, Grafen, Elektrospreyleme, Tamir Yaması, Konik Zımparalama, Akustik Emisyon

Fiber takviyeli kompozitler, üstün yapısal özellikleri ve hafif ağırlığı nedeniyle havacılık, enerji, otomotiv endüstrilerinde birincil ve ikincil yapılarda yaygın olarak tercih edilmektedir. Bununla birlikte, kompozit materyaller düşük darbe direnci, delaminasyon mukavemeti, kırılma tokluğu ve tamir edilebilirlik açısından gibi belirli sınırlamalara sahiptir. Bu nedenle, kompozit malzemelerin mekanik özelliklerini geliştirmek için birçok girişimde bulunulmuştur, bunlardan birisi de kompozit içindeki fiber veya reçine fazlarına nano ölçekli takviye entegrasyonudur. Yakın dönem araştırmaları, grafen-takviyeli kompozit malzemelerin takviyesiz olanlara göre daha fazla avantaja sahip olduğunu göstermektedir. Tezin ilk kısmında grafen ve nano-takviyelendirme üzerine bir literatür araştırması yapılmıştır. İkinci bölümde, üç farklı nano-malzeme takviye düzenlemesi araştırılmıştır. Grafen, arayüz ve matris değiştirici olarak kullanılmıştır. Nano-takviyeli numunelerin eğilme, çekme ve kırılma tokluğu test sonuçlarında dikkate değer gelişmeler gözlenmiştir. Ek olarak, grafenin iletkenlik özelliği nedeniyle, nano malzeme takviyeli kompozitler hem elektriksel hem de termal iletkenlik değerleri kazanmıştır. Üçüncü bölümde, elektrospreyleme cihazının çoklu enjektörler ile tasarlanması üzerine kapsamlı bilgi verilmiştir. Elektrospreyleme, nano-malzeme kaplama için hızlı, kullanıcı dostu ve düşük

maliyetli olan yöntemlerden biridir. Yeni çoklu enjektörlü elektrospreyleme cihazı, kompozit teknolojileri araştırma merkezinde seri üretim hattındaki kompozit malzemelere nano malzeme kaplanmasına öncülük edecektir.

Son bölümde, kompozitlerin nano-takviyelendirilmesi hakkında ilk bölümde elde edilen olumlu sonuçlar, tamir yama metodunun geliştirilmesi için kullanılmıştır. Matriks ve arayüzleri nano- takviyeli tamir yamaları üretilmiş ve tamir prosedürüne dahil edilmiştir. Tamir edilen kompozit malzemelerin mekanik özellikleri açısından en verimli yöntemi bulmak için iki farklı zımparalama yöntemi test edilmiştir. Tamir yamalarındaki arayüz ve matriks modifikasyonundan dolayı, nano-takviyeli yamalar ile tamir edilmiş kompozit parçaların kayma testi sonuçları dikkate değer ölçüde iyileştirilmiştir. Sonuç olarak; bir güçlendirici olarak grafen, kompozit yapı ve tamir işlemlerinin mekanik özelliklerinin iyileştirilmesi için başarıyla kullanılmıştır.

*To my beloved grandmother Şükriye.*



## ACKNOWLEDGEMENTS

I would like to express my gratitude to my thesis advisor Prof. Dr. Mehmet Yıldız for his excellent advises and support and encouragement throughout the research.

A very special gratitude goes out to my co-supervisor Dr. Jamal Seyyed Monfared Zanjani. I have been lucky to have a co-supervisor who spared his time to my work and cared about to my problems and responded to my questions promptly.

I would also like to thank all my colleagues, friends and lab members in Kordsa – Sabanci University Composite Technologies Center of Excellence. Without their knowledge and support this work would not have been possible.

Special thanks to Dr. Serra Topal for reviewing my thesis with her valuable comments and suggestions.

My sincere appreciation goes to Cihan Kan from Turkish Technic. His expertise, invaluable guidance, affectionate attitude, understanding added considerably to my experience.

Many thanks to Dursun Bayraklı and his team for providing necessary composite laboratory facilities with me in Turkish Technic.

I owe to my deepest thanks to my dear mother, father and aunt. They have always supported me through morally and emotionally. Special thanks go to my lovely sisters Hale and Şenay for providing me continuous encouragement and inspiration to my life. I am so lucky being a part of this family.

The last but not least, I want to thank to myself. I learned a lot about my capabilities, forbearance, determination and curiosity limits during this journey. I am very glad to pursue my dreams.

# TABLE OF CONTENTS

ABSTRACT .....	i
ÖZET... ..	iii
ACKNOWLEDGEMENTS.....	vi
TABLE OF CONTENTS .....	vii
LIST OF FIGURES .....	x
LIST OF TABLES .....	xiv
CHAPTER 1. STATE OF THE ART .....	1
CHAPTER 2. MECHANICAL ENHANCEMENTS IN GRAPHENE OXIDE INTEGRATED CARBON FIBER REINFORCED COMPOSITES	
2.1 INTRODUCTION .....	4
2.2 EXPERIMENTAL .....	5
2.2.1 MATERIALS .....	5
2.2.2 PREPARATION OF TEGO SOLUTION FOR ELECTROSPRAYING AND RESIN INTEGRATION PROCESSES.....	6
2.2.3 INTEGRATION OF TEGO BY ELECTROSPRAYING METHOD .....	7
2.2.4 MANUFACTURING OF REINFORCED CARBON FIBER COMPOSITES .....	8
2.2.5 CHARACTERIZATION.....	9
2.3 RESULTS AND DISCUSSION .....	12
2.3.1 DIFFERENTIAL SCANNING CALORIMETER(DSC)TEST METHOD... ..	12
2.3.2 NON-DESTRUCTIVE TESTING METHOD .....	15
2.3.2.1 ACTIVE THERMOGRAPHY TEST.....	15
2.3.2.2 PENCIL - LEAD BREAKAGE TEST WITH ACOUSTIC EMISSION.....	17
2.3.2.3 IN- PLANE ELECTRICAL CONDUCTIVITY TEST .....	19
2.4.2 MECHANICAL TESTS.....	21
2.4.2.1 MODE I FRACTURE TOUGHNESS TEST.....	21

2.4.2.2 TENSILE TEST.....	29
2.4.2.3 EVALUATION OF ACOUSTIC EMISSION FOR MODE I FRACTURE TOUGHNESS AND TENSILE TESTS.....	37
2.4.2.3 COMPRESSION TEST.....	45
2.4.2.4 FLEXURAL PROPERTIES - 3 POINT BENDING TEST.....	50
<b>CHAPTER 3. DESIGN OF MULTIPLE- NOZZLE ELECTROSPRAYING DEVICE</b>	
3.1 INTRODUCTION .....	56
3.2 EXPERIMENTAL.....	56
3.2.1 EQUIPMENTS .....	57
3.2.2 WORKING PRINCIPLE OF THE ELECTROSPRAYING UNIT.....	58
3.2.3 DESIGN OF THE MULTIPLE NOZZLE ELECTROSPRAY UNIT.....	58
<b>CHAPTER 4. REPAIR OF CARBON FIBER MONOLITHIC PLATES</b>	
4.1 INTRODUCTION .....	65
4.2 EXPERIMENTAL.....	66
4.2.1 MATERIALS.....	66
4.2.2 CHARACTERIZATION.....	66
4.2.3 PREPARATION OF GRAPHENE INTEGRATED EPOXY RESIN.....	66
4.2.4 PREPARATION OF MECHANICAL TEST SPECIMENS.....	68
4.2.5 MECHANICAL TEST RESULTS OF TEGO INTEGRATED RESIN.....	69
4.2.6 MANUFACTURING OF THE CARBON FIBER REINFORCED COMPOSITE PLATES .....	72
4.3 REPAIR OF THE COMPOSITE PLATES.....	75
4.4 MECHANICAL TESTS.....	81
4.4.1 SHEAR TEST.....	82

## CHAPTER 5. CONCLUSIONS

5.1 MECHANICAL ENHANCEMENTS IN GRAPHENE OXIDE INTEGRATED CARBON FIBER REINFORCED COMPOSITES .....	87
5.2 DESIGN OF MULTIPLE NOZZLE ELECTROSPRAY DEVICE.....	88
5.3 REPAIR OF CARBON FIBER MONOLITHIC PLATES .....	89

## BIBLIOGRAPHY

## LIST OF FIGURES

Figure 2.1 Biaxial router Electro spraying device with New Era NE -300 syringe pump.....	8
Figure 2.2 Composite manufacturing by vacuum infusion method (a) first batch (b) second and third batches.....	9
Figure 2.3 Optical Microscope images of (a, c) neat carbon fiber (400 $\mu\text{m}$ , 100 $\mu\text{m}$ ) (b, d) TEGO-coated carbon fiber (400 $\mu\text{m}$ , 100 $\mu\text{m}$ ).....	10
Figure 2.4 SEM images of TEGO deposited dry fiber (a) 5 $\mu\text{m}$ (b) 10 $\mu\text{m}$ (c) 50 $\mu\text{m}$ (d) 100 $\mu\text{m}$ .....	10
Figure 2.5 Heat-flow-type DSC schematic setup.....	13
Figure 2.6 The Mettler Toledo TGA/DSC3 device.....	13
Figure 2.7 Thermography images of (a) Neat (b) CFRP/INT (c) CFRP/MTX (d) CFRP/INT+MTX composite plates.....	16
Figure 2.8 Acoustic emission test setup.....	17
Figure 2.9 Mean values of elastic modulus for the different arrangements of nano-integration in composite plates.....	18
Figure 2.10 Electrical conductivity test system.....	20
Figure 2.11 Electrical conductivity test results.....	20
Figure 2.12 Various failure mechanisms in fiber reinforced composites during mode I fracture toughness test .....	22
Figure 2.13 Mode I fracture toughness test.....	23
Figure 2.14 The configuration of the mode I fracture toughness energy test setup with acoustic emission sensors.....	23
Figure 2.15 Fiber bridging during mode I fracture toughness test.....	25
Figure 2.16 Optical microscope images (100 $\mu\text{m}$ ) of (a) CFRP/INT and (b) CFRP/INT+MTX (c) Neat (Reference) (d) CFRP/MTX.....	27
Figure 2.17 (a) Fiber bridging and (b) interfacial failure in CFRP/INT system.....	28
Figure 2.18 Representative load vs. crack mouth opening displacement (CMOD) graph of Mode I fracture toughness energy test.....	28

Figure 2.19 Schematic for the tensile test, and the test specimen with biaxial strain gage attached and aluminum tabs.....	30
Figure 2.20 (a) Tensile stress-strain graph consisting of CFRP with different nano-reinforcement configurations; (b) close-up view of the tensile stress-strain curves.....	32
Figure 2.21 Optical microscope images of (a), (b) fiber cracking of neat specimen after tensile test (c) holes on CFRP/INT (d) holes on CFRP/INT+MTX.....	34
Figure 2.22 Tensile specimen with shattered and failure with splits failure.....	35
Figure 2.23 Representative Poisson's ratio vs. axial strain graph for each CFRP arrangement with different nano- reinforcement configurations.....	36
Figure 2.24 Representative scatter plot of partial power 4 vs. weighted peak frequency of (a) neat (b) CFRP/INT (c) CFRP/MTX and (d) CFRP/INT+MTX for mode I fracture toughness test.....	39
Figure 2.25 The average number of hits for mode I fracture toughness test with three micro damage types for each arrangement .....	41
Figure 2.26 Representative scatter plot of partial power 2 vs. weighted peak frequency of (a) neat (b) CFRP/INT (c) CFRP/MTX and (d) CFRP/INT+MTX for tensile test.....	42
Figure 2.27 The average number of hits for tensile test with three micro damage types for each arrangement.....	44
Figure 2.28 Schematic for the compression test specimen.....	46
Figure 2.29 Schematic representation of (a) in-phase buckling, and (b) kink- band formation under axial compressive loading .....	46
Figure 2.30 Stress - strain curves of the axial compression test of the four different composite arrangements .....	47
Figure 2.31 Optical microscope view of the hole formations and fiber misalignment in CFRP/INT from the axial compression test specimen.....	48
Figure 2.32 Optical microscope image of the CFRP/INT specimen cross section.....	48
Figure 2.33 (a) Delamination growth and fiber kink formation in CFRP/MTX (b) detailed view of fiber kink formation.....	49
Figure 2.34 Optical microscope image of cross section view of CFRP/MTX damaged specimen, arrows indicating the path of advancing crack.....	49

Figure 2.35 Three-point bending test.....	50
Figure 2.36 Representative flexural stress - strain graph.....	52
Figure 2.37 Apparatus with the mounted specimen used to imitate the loading of 3-point bending test.....	53
Figure 2.38 Optical microscope images of the damaged (a) CFRP/INT, (b) CFRP/MTX specimens.....	53
Figure 2.39 Optical microscope image of the (a) CFRP/INT+MTX (b) Neat specimens...54	
Figure 2.40 The percentage improvement of mechanical properties of each system.....	55
Figure 3.1 The design of Multiple-nozzle electro spray unit in SolidWorks software .....	58
Figure 3.2 The pump stand .....	59
Figure 3.3 Completed assembly of the first design pump stand .....	60
Figure 3.4 New design for six-channel pump stand from Kestamid and fiber material in SolidWorks .....	60
Figure 3.5 New design for six channel pump stand from Kestamid and fiber material.....	61
Figure 3.6 Electro spray profiles with six needles.....	62
Figure 3.7 Homogeneous spraying profile .....	62
Figure 3.8 Final design of the pump stand with the syringes mounted.....	63
Figure 3.9 Automated electro spraying unit with the computer system and heat blanket controllers .....	63
Figure 4.1 Aluminum molds used in the production of test specimens.....	67
Figure 4.2 The prepared (a) reference and (b) TEGO reinforced tensile test specimens.....	67
Figure 4.3 The reference test samples (a) during tensile test and (b) three point bending test.....	68
Figure 4.4 The tensile stress-strain curves obtained (a) reference state, after the stirring of the tensile test specimens at (b) 5000 rpm, (c) 10000 rpm and (d) 12000 rpm.....	69
Figure 4.5 The flexural stress-strain curves obtained (a) reference sample, after mixing at high speed of (b) 5000 rpm, (c) 10000 rpm and (d) 12000 rpm of high-shear mixing .....	70
Figure 4.6 Homogeneous distribution of graphene in epoxy.....	72

Figure 4.7 Stacking sequence of the prepregs.....	73
Figure 4.8 25 x 25 CFRC Plate.....	74
Figure 4.9 Hot Press.....	75
Figure 4.10 Taper ratios.....	76
Figure 4.11 Metal stencils for marking sanding outlines.....	77
Figure 4.12 Taper sanding method.....	77
Figure 4.13 Taper sanding method (a) Top view (b) cross section view.....	78
Figure 4.14 Water break test.....	78
Figure 4.15 Ply boundaries marked by silver pencil.....	79
Figure 4.16 (a) Ply boundaries (b) layup of the repair plies.....	80
Figure 4.17 Vacuum bagging steps.....	81
Figure 4.18 Shear test specimen with strain gage attached on its surface.....	82
Figure 4.19 Schematic of the shear stress distributions in (a) stepped sanded repair site, (b) tapered (scarf) sanded repair site.....	84
Figure 4.20 Representative Shear Stress -Strain graph .....	84
Figure 4.21 Damaged test specimens after completing the shear tests.....	85
Figure 4.22 Optical microscope images of the lateral view of (a) (a) m- prepreg tapered (b) f- prepreg tapered specimens.....	85
Figure 4.23 Optical microscope images of lateral view of (a) neat stepped (b) neat tapered specimens. ....	86



## LIST OF TABLES

Table 2.1 NANOGRAFEN® TEGO Grade-2 Data Sheet.....	6
Table 2.2 DSC resin test results.....	14
Table 2.3 DSC test results for different composite arrangements.....	15
Table 2.4 Improvements in the fracture toughness energy.....	24
Table 2.5 Mean values of the data from the void content tests.....	26
Table 2.6 Mean values of tensile test results.....	30
Table 2.7 Flexural properties of the test specimens.....	51
Table 4.1 Tensile and three- point bending test results.....	71
Table 4.2 Properties of the carbon fiber prepreg and epoxy.....	73
Table 4.3 Shear test results.....	83

# Chapter 1

## State of the Art

Composite materials are widely preferred in many industries such as aerospace, energy, automotive and electronic applications due to their superior properties compared to traditional materials[1]. Despite this considerable demand from the advanced materials industries, applications of composite materials have certain limitations due to their low impact resistance and delamination strength, especially for the unidirectional or biaxial fiber reinforced composites, and low fracture toughness due to the brittle resin material hosting the fibrous reinforcement [2, 3]. Therefore, there have been numerous attempts to improve the mechanical properties of composite materials and one recent and promising outcome is the nano-material integration in materials. Nano material integrated composites have shown considerable advantages over their non-modified counterparts, facilitating the reinforcing mechanisms and load transfer from the matrix to the reinforcing agents as a result of the high surface-to-volume and high aspect ratios of the nano-materials[4]. Therefore, the combination of nano-material and polymeric composite materials results in structures with excellent toughness, strength and other complementary properties such as electrical and thermal conductivities [5]. An emerging nano-material for composite interface modifications is Graphene, which consists of single-layer carbon sheets with a hexagonal packed lattice structure. Carbon nanotubes (CNTs) is another nano-material attracting significant attention, which is not focused in this study.

Regarding the integration of nanoparticles to various phases of composite materials, agglomeration is a commonly experienced issue, which reduces the efficiency of the integration methods (i.e. electrospraying or dispersing in chemical solutions) and adversely affects the mechanical properties of the resulting composite [6,7] by drawing the values below those of well dispersed nano- integrated or even neat structures[8]. Therefore, new solutions to improve the current graphene integration methods are required to avoid reduced performances of nano-modified composites. One recognized method to produce

nanocomposites is integrating graphene into the polymeric matrix. However, this method's success is highly dependent on the processing parameters, chemistry and rheological behavior of the polymers or resins. Another methodology, electrospraying, is one of the innovative methods for selective integration of graphene into the composite structure, in which the nano-particles are sprayed on the dry fabric preform to increase the surface area of the single fibers without altering their superior properties.

In the first part of this thesis, these two approaches and their combination were employed to examine the effect of graphene on the mechanical performance of composites to create a composite structure with a broad range of desired properties, suitable for niche applications in harsh environments. Three different arrangements were developed to examine the effect of thermally exfoliated graphene oxide (TEGO) on the mechanical properties of the resulting composite material. Mode-I fracture toughness energy, tensile, compression, and three-point bending tests were conducted on the reference (neat), fiber interface-modified, modified-resin and multiscale modified composite plates. Additionally, electrical conductivity tests were conducted to prove the conductivity characteristics of the graphene nano-reinforced composites. In the first arrangement, TEGO was implemented in the composite by electrospraying method on the fibers. TEGO as an interface modifier has increased the bonding between matrix and fibers and consequently improved the interfacial strength. In the second arrangement, TEGO was dispersed into the hardener of the epoxy system to enhance the matrix properties and load distribution. In the last arrangement, TEGO was used as both matrix and interface modifier.

In the second part, a large-scale fully autotomized electrospraying system was designed for industrial applications and manufactured with multiple nozzles for the electrospraying of the nanomaterial onto the large surface areas of the fibers. The designed device enables a fast, easy-to-use and cost-effective process and paves the way to the industrial processing of nanocomposites at the research center. All the working parameters such as the rate of spraying, the route, speed and position are adjustable. For this purpose, Poysan B100150 CNC Router was modified into the electrospraying system with a protective cabin including its safety measures. High voltage applied to the tip of spraying nozzle overcomes the surface tension, thus significantly reducing the size of the jet of the TEGO solution, resulting in atomized TEGO solution with finely dispersed nanophase. The dry fiber

preform that is sprayed is continually heated with heating blankets under the spraying platform, to evaporate the Dimethylformamide (DMF) that is used as the nano-phase solvent.

In the last part, the well-known methodology for repairing composite materials, the scarf repairing, was improved with the employment of TEGO integrated repair patches. The proper maintenance and prevention of serious damage in composite structures is a long-known limitation for their widespread applications especially in the aerospace and wind energy applications [9]. Despite the several methods proposed for repairing damaged composites, the performance of the repaired structures is lower than that of healthy or sound material. In the third part of this thesis, a common repair methodology with high efficiency was improved through utilizing nanomaterial-integrated repair patches. These patches were produced from the nano-integrated fiber preforms with the use of the developed multiple-nozzle electrospray unit. As a first step, two repair methods, the tapered and stepped sanding, were performed on the damaged composite plates, and their performances were compared by means of mechanical testing. The results revealed that the shear modulus, also the maximum load carrying capacity of the stepped sanded repaired plates were lower with respect to the taper sanding, so the latter method was preferred as the main repairing technique for the rest of the study. Acoustic emission as a structural health inspection technique was also used to differentiate the failure types in the repaired composites. Remarkable enhancements were obtained from the shear tests as the interface modifiers dominated the mechanical behavior of the fiber and polymer phases during shear loading.

To conclude, this study brings a new understanding to the impact of graphene as a nano-reinforcement on the mechanical performance of the Carbon fiber reinforced polymeric composite materials. Furthermore, it proposes a nano-modified repair methodology, nano-integrated scarf repairing, to achieve higher efficiency and more reliable mechanical performance in the repaired composite structures, making this study a unique one in the literature.

## Chapter 2

### Mechanical Enhancements in Graphene Oxide Integrated Carbon Fiber Reinforced Composites

#### 2.1 Introduction

This section provides comprehensive information on the selective integration of thermally exfoliated graphene oxide (TEGO) as a nano reinforcement into carbon reinforced epoxy composite structures. The long-known poor mechanical properties of the fiber reinforced polymer composites in the transverse directions, which result in low impact resistance, delamination strength and fracture toughness [2, 3], paved the way to countless research on the improvement of the fiber phase, matrix phase and fiber-matrix interfaces. The mechanical properties of the fiber reinforced polymer composites are dependent to the type of the fiber, resin material and the strength of interfacial bonding between fiber-matrix, which controls the load transfer from the matrix to the load-carrying fibers [2, 4]. While some methods focus on increasing the surface roughness of the fibers for an improved interface bonding to the matrix [11-12], other methods deal with the integration of nano materials at the fiber-matrix interface for enhanced bonding. The latter solution, “nano-integration”, recently attracted considerable attention since it does not alter the fiber structure in any way. Due to its high carrier mobility at room temperature ( $\sim 10\,000\text{ cm}^2\text{ V}^{-1}\text{ s}^{-1}$ ) [13], large theoretical specific surface area ( $2630\text{ m}^2\text{ g}^{-1}$ ) [14], high Young’s modulus ( $\sim 1\text{ TPa}$ ) [15] and thermal conductivity ( $3000\text{--}5000\text{ W m}^{-1}\text{ K}^{-1}$ ) [16], graphene has surpassed carbon nanotubes (CNTs) with its wider areas of application; and is also selected in this study as nano reinforcement agent for the investigation of its impact on overall mechanical performances of the composite structures. For this purpose, three different arrangement systems of the nano-integration were studied. In the first configuration, both sides of dry Carbon fiber preform (unidirectional, 6K, provided from Kordsa Global company) were coated with TEGO by using electrospraying method. Coating the surface of carbon fibers with TEGO primarily increases the surface roughness of the carbon fibers, thus increases the total surface area, which will lead to an improved interfacial interaction between fibers and matrix. In the second

configuration, TEGO was incorporated in the epoxy resin system by means of mechanical and planetary mixing in the polymer, and composite specimens were produced with non-modified carbon fibers. This case would reveal the effect of nano reinforcement in the resin material, and distinguishing its impact on the overall composite from the case of TEGO effect on fiber phase. In the third case, a combination of the above-mentioned configurations was implemented: the upper and lower surfaces of carbon fabrics were coated with TEGO through electro spraying, and the epoxy resin was modified with TEGO through dispersion, to obtain a hybrid composite structure with superior performance. It is anticipated that the integration of the TEGO as an interface modifier would enhance the efficiency of load transfer to the matrix. On the other hand, integration of TEGO into the matrix would enhance matrix-dominant mechanical characteristics. The methodologies developed and utilized for producing nano-composites will pave the way for industrial applications with an easily scalable process as it offers production of lighter, durable and reliable structures.

## **2.2 Experimental**

### **2.2.1 Materials**

Thermally exfoliated graphene oxide (TEGO, Grade-2) as a nano-reinforcing agent was kindly provided by the company NANOGRAFEN<sup>®</sup> for research purposes. N, N-dimethyl formamide (DMF, Sigma Aldrich, 99%) was used to prepare TEGO dispersion for the electro spraying process. Biresin<sup>®</sup> CR120 epoxy resin and Biresin<sup>®</sup> CH 120-6 hardener system was used to manufacture the composite plates. Biresin<sup>®</sup> epoxy hardener system is generally preferred for the production of high performance fiber reinforced composites with 115 °C glass transition temperature. The unidirectional 6K carbon fiber with heat set thermoplastic coated yarn which supplied by Kordsa was used in composite production. Paint<sup>™</sup> SPI #5001-AB Flash-Dry Conductive Silver Paint with high electrical conductivity was used to eliminate the contact resistance in electrical conductivity measurements.

### 2.2.2 Preparation of TEGO Solution for Electrospaying and Resin Integration Processes

The distribution of the TEGO in the DMF plays an important role in the mechanical properties of the composites with nano-modified interfaces, as it directly affects the electrospaying performance and homogeneity of the covering nano-particles. Poorly dissolved TEGO in DMF creates clusters of graphene particles on the dry fiber and sometimes even in the nozzle systems, being sprayed with sudden and large droplets on the dry fabric, thereby forming stress concentration regions in the resulting composite plate. The quality of the dispersion plays a crucial role in the electrospaying process, since a homogeneous distribution is required to achieve a uniform spraying and a well-covered fiber surface. The dispersion quality of the TEGO is primarily related with the carbon/oxygen ratio of graphene and the viscosity of the epoxy resin-hardener mixture. The main reason of choosing TEGO as a reinforcer is its boosted exfoliation ratio with the thermal process, which removes the oxygen groups from the surface of the graphene oxide, approaching to the original graphene structure [17].

**Table 2.1** NANOGRAFEN® TEGO Grade-2 Data Sheet.

Appearance	Dark Gray
Bulk Density	0,022 g/mL
Average number of layers	23
Solubility	Partially soluable in water, homogeneous dispersion in DMF, THF, other organic polar solvents and epoxy hardener (apply sonication process for homogenous dispersion).
Oxygen content	<4,0%

Initially, TEGO particles were dispersed into the DMF (0.1 wt.%) using a probe sonicator (Qsonica, Q700) for 30 minutes. Then the dispersion was stabilized by a water bath sonication (VWR USC- TH Ultrasonic Bath) for at least 5 days at 40°C to achieve a well-dispersed TEGO in DMF. TEGO weight percentage for this type of nano integration is specified as 0.01 wt. %. The coated fabrics were later used for composite production, and this group is referred as CFRP/INT.

For the second arrangement, 0.05 wt.% TEGO was dispersed in the Biresin<sup>®</sup> CH 120-6 hardener, which has a lower viscosity than the resin used. The same sonication procedure to prepare the DMF dispersion was followed at 40°C to disperse thermally exfoliated graphene oxide in the hardener. This group of specimens will be recalled as CFRP/MTX in the rest of the text, and the TEGO weight percentage of CFRP/MTX is 0.01 wt. %. In the last arrangement, multi-scale reinforced composite system was prepared with electrospayed carbon fiber preforms, and TEGO-integrated resin material. The total weight percent of TEGO in the CFRP/INT + MTX composite (the last group of specimens with TEGO integration both at the interface and the matrix) is 0.02 wt.%.

### **2.2.3 Integration of TEGO by Electrospaying Method**

Electrospaying is an efficient method for spraying the conductive nanoparticles to achieve a very fine dispersion and a uniform coverage on the target surface. This method utilizes high voltage as its driving force and is applied to the metallic syringes via the connected crocodiles, whereas the aluminum platform is grounded to complete the circuit. During the process the chemical solution consisting of properly dispersed nano particles inside a solvent goes through atomization under the voltage difference between the nozzle (syringe) system and the targeted surface. With atomization, the TEGO/DMF solution is pulverized into electrically charged droplets at the tip of the metal nozzle [18].

The prepared solution was then loaded into a syringe with a metallic nozzle and sprayed on both sides of the 40 x 30 cm dry carbon fabric using a lab-scale automated electrospaying device, which can be viewed in Figure 2.1. A New Era NE -300 syringe pump was used to keep the flow rate constant at 100 ml min<sup>-1</sup> during the electrospaying process. The syringe pump was mounted on a biaxial router and spraying was performed along x and y axes over the carbon fabric at an optimized speed, while the height of the nozzle was fixed 15 cm away from fabric surface. A Gamma High Voltage Electrospinning series ES 30P Models DC power source was used to supply constant 15 kV electrical voltage. As previously stated, high voltage enables atomization of the sprayed chemical solution while passing through the syringe and allows a stable distribution of nano-phase on the targeted fiber surfaces.



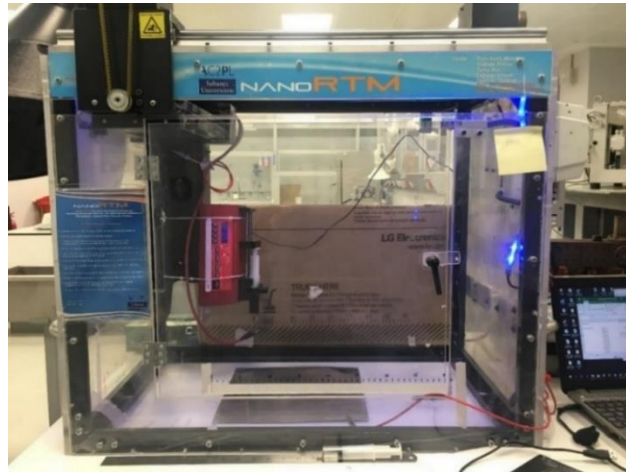
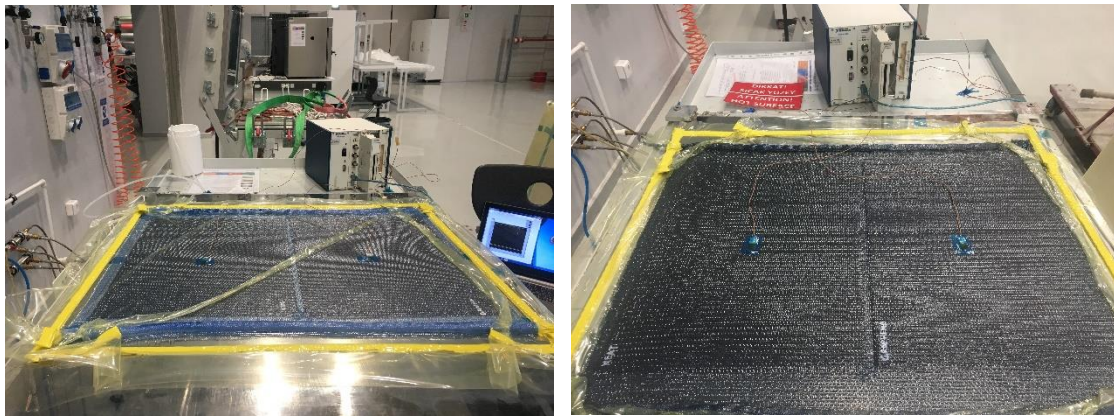


*Figure 2.1* Biaxial router Electro-spraying device with New Era NE -300 syringe pump.

#### **2.2.4 Manufacturing of reinforced carbon fiber composites**

In this part of the study, TEGO integrated carbon fiber reinforced composites were manufactured with vacuum infusion technique. Initially, the Aluminum molds were prepared by cleaning its surfaces with XTEND CX-500 Mold Cleaner liquid. Following, Axel XTEND AMS Semi- Permanent Mold Sealer and Releaser were applied onto the mold surfaces, respectively. Four-layers of carbon fibers were stacked in  $0^{\circ}/90^{\circ}/0^{\circ}/90^{\circ}$  orientation. A Teflon film was placed between the 2<sup>nd</sup> and 3<sup>rd</sup> fabric layers during production for the future mode-I fracture toughness energy tests. Peel ply and a flow mesh were put onto the stacks. Spirals were utilized to obtain a steady-flow of the resin. For the last step, vacuum bagging was applied, avoiding excessive force on the stacked layers. Vacuum was then applied through a pump to detect if there was a leakage in the bagging. Subsequently, the layers were left under vacuum for 60 minutes. Meanwhile, the resin and hardener were mixed and degassed for 10 minutes to remove any entrapped air bubbles in the mixture. After the impregnation of the epoxy/hardener mixture, TEGO-integrated carbon fibers were cured at  $120^{\circ}\text{C}$  for 15 hours on the heating table. In the first batch, vacuum infusion was employed by flowing degassed neat resin/hardener mixture through the TEGO integrated fibers (CFRP/INT) and neat fibers

simultaneously. In the second and third batches, CFRP/MTX and CFRC/INT+MTX were impregnated by TEGO- epoxy- hardener system with vacuum infusion (Figure 2.2.).



(a)

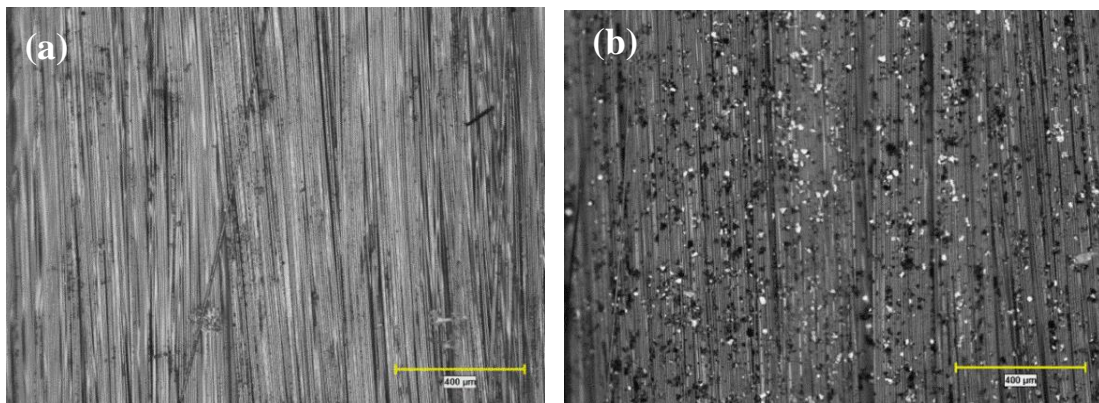
(b)

**Figure 2.2** Composite manufacturing by vacuum infusion method (a) first batch (b) second and third batches.

Thermocouples were used to follow the changes in the temperature during the curing process. Two K-type thermocouples were placed on top of the vacuum bag for each plate. The remaining ones were placed on the heating surface and on the table to follow the temperature values of both the table and the ambient conditions.

### 2.2.5 Characterization

The surface morphologies of the neat and graphene sprayed fabrics were examined by Nikon Eclipse LV 100ND optical microscope (Figure 2.3) and Leo Supra 35VP Field Emission Scanning Electron Microscope (SEM) (Figure 2.4).





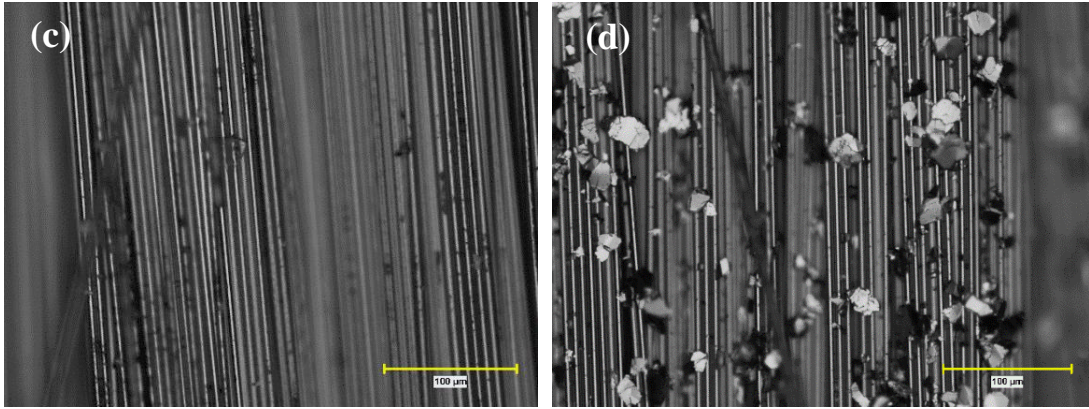


**Figure 2.3** Optical Microscope images of (a, c) neat carbon fiber (400 μm, 100 μm) (b, d) TEGO-coated carbon fiber (400 μm, 100 μm).

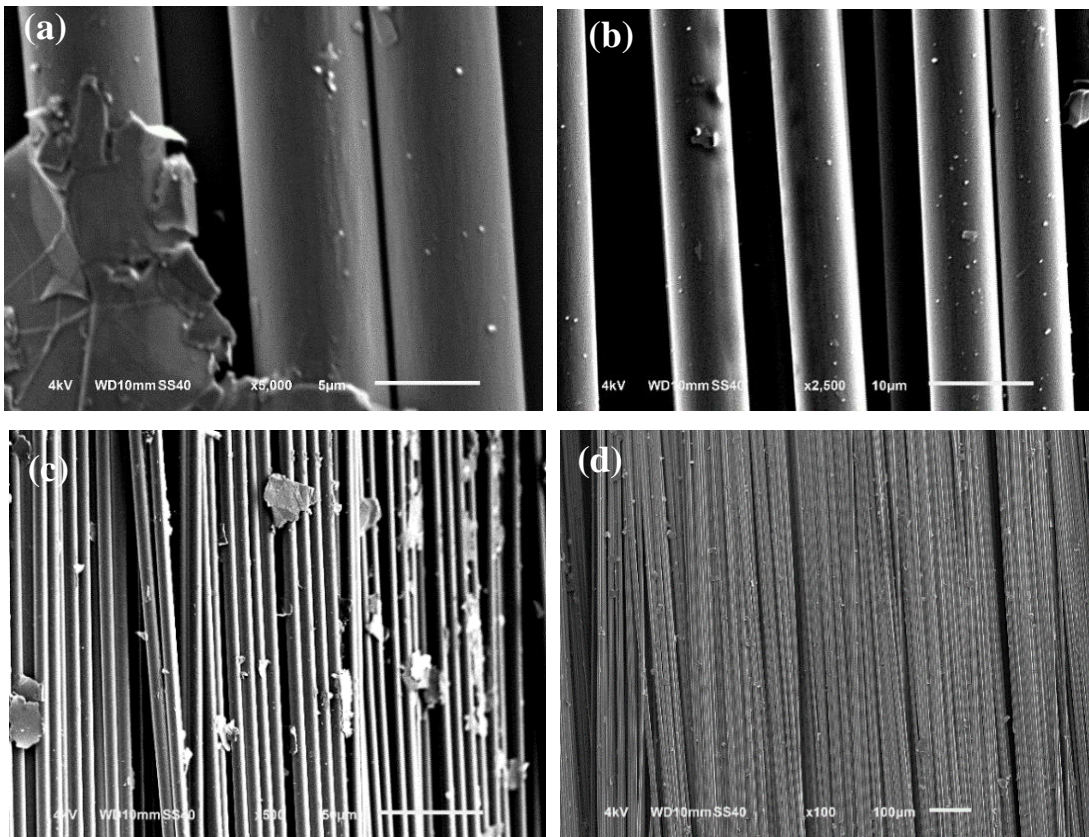


**Figure 2.4** SEM images of TEGO deposited dry fiber (a) 5 μm (b) 10 μm (c) 50 μm (d) 100 μm.

The greatest advantage of this method, as stated earlier, is it's not influencing the structure of the fabric, i.e. the fibers retain their initial morphologies after TEGO deposition on them. This can also be viewed from the optical microscope and SEM images of dry fiber preforms, provided in Fig. 2.3 and 2.4. Comparing the images of neat fibers to the TEGO integrated ones, the total surface area of the modified system increases drastically. TEGO particles remain on the surface of the fibers with Van der Waals forces and electrostatic interactions after the electrospraying process [19]. Figure 2.4 (a) and (c) show how graphene nano particles are attached on fiber surfaces. The increase in the total surface area of fibers with an enhancement in surface roughness leads to a remarkable strengthening at the interface and the bonding of fibers to matrix.

The following tests were conducted to the produced composite batches:

- i) Active thermography and acoustic emission (AE) (non-destructive inspection)
- ii) Thermogravimetric Analysis (TGA) and Differential Scanning Calorimetry (DSC)
- iii) Mode-I fracture toughness energy (EN 6033)
- iv) Tensile test (ASTM 3039)
- v) Compression test (ASTM D6641/D 6641M)
- vi) Three-point bending test (ASTM D790-3)

Active thermography was used for detecting in-plane defects that might have occurred during production of the samples. Moreover, pencil – lead breakage test with acoustic emission (AE) test was conducted to examine the Young's Modulus of the composite. Thermogravimetric Analysis (TGA-details provided in the Appendix) and Differential Scanning Calorimeter (DSC) were conducted to examine thermal stability of the specimens and the effect TEGO on heat of curing of uncured resin, respectively. To investigate the mechanical characteristics of each specimen group, mechanical tests listed above were performed on INSTRON 5982 Universal Test Machine (UTM). The fractographic analysis was performed to investigate the failure mechanisms developed in the composite specimens after each test type. After three-point bending test, the damaged specimens were located into a special apparatus to imitate the same bending behavior and apparatus was dipped into a fast-curing resin/hardener system to fix the damaged part in resin [20]. Detailed explanations of this procedure are provided in Section 2.4.

## **2.3 Results and Discussion**

### **2.3.1 Differential Scanning Calorimeter (DSC) Test Method**

Differential scanning calorimetry (DSC) is a method in which the difference between the required amount of heat to raise the temperature of a sample by 1°C is measured and evaluated as a function of time and temperature in comparison with a reference sample. This analysis provides numerical data on the exothermic and endothermic processes by measuring the absorbed or released energy by the sample during its heating or cooling. The following properties of any material can be evaluated by DSC: melting temperature, reaction energy and temperature, glass transition temperature, crystal phase transition temperature and energy, precipitation energy and temperature, denaturation temperatures, oxidation induction times, specific heat or heat capacity values. Additionally, exothermal energy during polymer curing (as in the case of epoxy adhesives), thus the curing rate and degree can be measured with DSC. It is also useful to specify the glass transition or softening temperatures for the polymeric or glassy substances, also the transitions from crystal to amorphous states. These are directly dependent to the thermal history of the material, the amount and type of the (nano or micro) filler. This test is also preferred to specify the thermal stability and reaction kinetics, or to verify an unknown material to be an expected one.

The experimental setup is shown schematically in Fig. 2.5 for the heat-flow type of DSC analysis. The methodology consists of two samples one of which is a reference, known material, both receiving an equal amount of heat and the temperature difference ( $\Delta T$ ) is zero at the initial state. When there is an endothermic or exothermic heat flow through the sample a signal is processed by the DSC device. The measured parameter is the heat flow rate as a function of temperature and time and has a unit of mW (mJ/sec). The related equation for the measurement of heat flow is provided below. In DSC test, Mettler Toledo TGA/DSC 3+ differential scanning calorimeter was used, which can be seen in Figure 2.6.

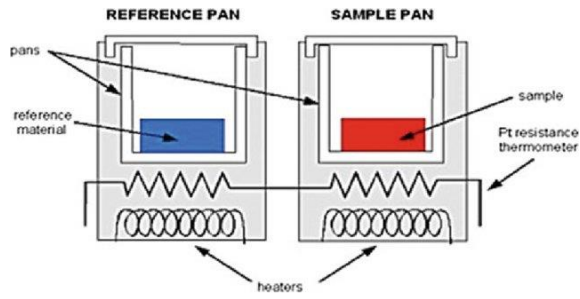


**Figure 2.5** Heat-flow-type DSC schematic setup [98].

$$\frac{dH}{dt} = C_p \frac{dT}{dt} + f(T, t) \quad (2.1)$$

$\frac{dH}{dt}$  : heat flow signal

$C_p$  : heat capacity of the specimen

$\frac{dT}{dt}$  : heating rate

$F(T, t)$  : kinetic heat flow, in terms of time and temperature



**Figure 2.6** The Mettler Toledo TGA/DSC3+ DSC device.

Two different DSC tests were conducted on the samples taken from the resin material and composite specimens. Purpose of the initial DSC test is to interpret the effect of TEGO on heat of curing of the uncured resin. Secondly, DSC test was used for the post cure enthalpy measurement and comparison with the neat sample. At the same time, glass transition temperature ( $T_g$ ) of both uncured and cured resin materials were measured.  $T_g$  is a transition

temperature of the polymer from rubbery state to glassy state and it is critical for the aerospace applications of polymeric composites.

For the first experiment set, two different batches which neat epoxy system and TEGO integrated epoxy system were prepared. 50 g Biresin<sup>®</sup> CR120 resin and 15 g Biresin<sup>®</sup> CH 120-6 hardener was mixed with Thinky ARV- 310 planetary vacuum mixer for one minute. Then, it was placed into the DSC device for analysis. The experiment was conducted under Nitrogen atmosphere.

The heating cycle of the first method was:

1. One heating ramp from room temperature to 200°C to see the heat of curing.
2. Cooling down from 200°C to the room temperature.
3. Again, heating the sample from the room temperature to 200°C to measure  $T_g$ .

The results obtained from the first DSC test are provided in Table 2.2.

**Table 2.2** DSC resin test results.

Type of resin	$T_g$ (°C)
NEAT	111.61
TEGO integrated	113.02

These results identify that the nano-phase integration clearly affects the glass transition temperature of the resin material, which is also reported in the literature [95,96,97]. The increase in  $T_g$  values is accepted as an indication of the Hydrogen bonds that are formed in the polymer chains. These increases not only inform about the vital changes in the polymer chain dynamics, but also significant achievements in the thermal stability that are critical for many applications of composites [97].

Following these outcomes, the impact of TEGO on various nano-phase arrangements (in the fiber-matrix interface, in the matrix, and both) was investigated with the second DSC test.

The heating cycle of the second method was:

1. Heating up the specimens from room temperature to 250 °C to see if there were uncured resin areas in the composite plate.

**Table 2.3** DSC test results for different composite arrangements.

Arrangement	T <sub>g</sub> (°C)
NEAT	118.71
CFRP/INT	119.22
CFRP/MTX	119.85
CFRP/INT+MTX	116.29

The Biresin® CR120, CH120-6 epoxy-hardener system is an aerospace-based resin in which the glass transition temperature is 120 ° C. The results of DSC test indicated that addition of TEGO into the matrix increases the T<sub>g</sub> roughly 2 degrees Celsius. Additionally, TEGO integration to the dry carbon fibers follows a similar trend as the neat one. However, the T<sub>g</sub> of the CFRP/INT+MTX was slightly decreased with respect to the reference specimen. Such a decrease in the T<sub>g</sub> was also reported in the work of Ramanathan et al [97] in which they used 0.1wt.% expanded graphene in the PMMA nanocomposites. The significant rises in T<sub>g</sub> values in nano-reinforced polymers are reported to happen in the case of functionalized nano-phases [97], which is not within the scope of the study.

To conclude, DSC test proved that the TEGO has no critical effect on curing temperature of the epoxy-hardener system.

Examining the DSC test results, no significant change was observed in the cure cycle of the neat resin and nano-phase arrangements.

## **2.3.2 Non-destructive testing method**

### **2.3.2.1 Active Thermography Test**

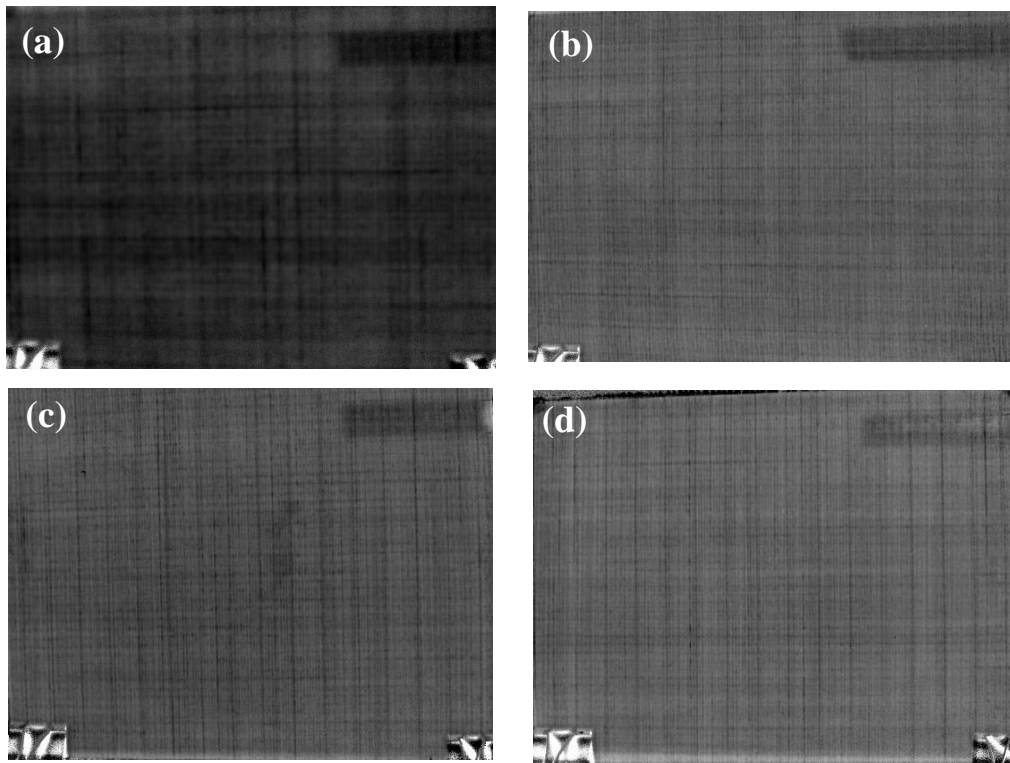
Thermography or thermographic analysis (TA) is a non-destructive test method that allows quick inspection of large areas for the detection of voids or other microstructural problems. Additionally, the thermographic analysis is capable of detecting the defects and



damages formed during production, which is very helpful for relating the former structural problems to the failure mechanisms that develop after the mechanical tests.

Active thermography was preferred in this study where an external heat source was used for heating the surface of the plate to examine the temperature decays with time [21, 22]. Thermal images were captured by FLIR X6580sc model infrared (IR) camera with a 640x512 resolution. 50 mm lens was used in IR camera and the camera was placed 40 cm away from the composite plates. The IR camera has a temperature range of 20 °C to 3000 °C with a capability of 1% accuracy.

The captured images were processed with Flir ResearchIR Max software to detect any imperfections or damage that had occurred prior to testing, such as delamination, debonding and cracks; together with dry points that might have remained in the materials [23].



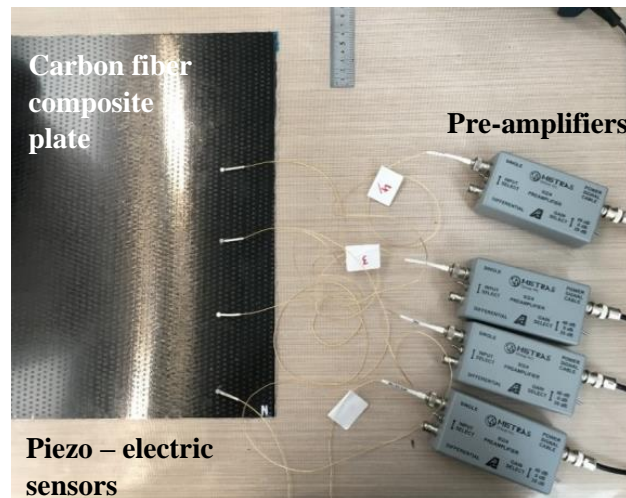
**Figure 2.7** Thermography images of (a) Neat (b) CFRP/INT (c) CFRP/MTX (d) CFRP/INT+MTX composite plates.

Figure 2.7 shows the resulting images of the thermography inspection, proving that there were no dry points, delamination or debonding neither on the surface nor the inner structure of the composite plates. Further, the Teflon film placed on the upper right corner of the plates

during the production (for the mode-I interlaminar fracture toughness test) can be observed in all samples.

### 2.3.2.2 Pencil - Lead Breakage Test with Acoustic Emission

Acoustic emission (AE) tests were performed on the nano- material integrated composite plates to investigate the effects of TEGO integration on the mechanical properties of the samples. The methodology of AE can be summarized as the transient elastic waves generated by one or more local sources in a material under tension, producing temporary transient elastic waves [24, 25] that are captured and processed by the receiver. The greater the applied force, the greater the elastic energy because of more elastic deformation. If the elastic limit of the material is exceeded, cracking or eventually breakage of the sample will occur. If there is a void like defect in the elastically loaded material, cracks will occur at these highly-stressed points and they lead to global failure. Rapid release of elastic energy is called the acoustic emission event. The AE produces an elastic wave that propagate in the material, which can be detected by suitable sensors immediately. During this test, the sound velocity measurements were received by placing the sensors at 8 cm distance from each other on the composite plate (Figure 2.8).



*Figure 2.8* Acoustic emission test setup.

Pencil - lead breakage is a method with an artificial source of acoustic waves, which is used to determine the elastic modulus without causing any destruction in the sample. In this

test, Mistras 0/2/4 preamplifier was used with single input and 20 dB gain which can also be seen in the figure above . In this test, the lead tip of the mechanical pencil is pressed onto the composite plate until the lead is broken. Deformation occurs at the surface of the plate during the pressing of the lead tip. When the lead tip is broken, the stress relaxation causes a certain displacement on the surface and accordingly AE waves start to propagate. For the evaluation of Young’s modulus, the related equation is provided below. Here, the time and distance are two important parameters, besides the density of the composite structure and speed of sound.

$$E = \rho V_s^2 \quad (2.2)$$

E: Elastic /Young’s Modulus (GPa)

$\rho$ : density (kg/m<sup>3</sup>)

V<sub>s</sub>: speed of sound (m/s)

The results of the pencil lead breakage tests are provided in Fig. 2.9 below. The mean values of the obtained data clearly show that the elastic behavior of the composite plates gradually increased with the different arrangements of TEGO-integration in the composites. As shown in Figure 2.9, the reference (neat) composite plate has the lowest value of elastic modulus, whereas 18.18% enhancement in the modulus occurred in the CFRP/INT+MTX system due to synergetic effect of both matrix and interface modifiers in the composite structure. Additionally, comparing the effect of TEGO nano reinforcement on the separate phases, the data shows improvement in the elastic moduli of the composite structures by 15.30 % and 11.95 % for CFRP/MTX and CFRP/INT, respectively.

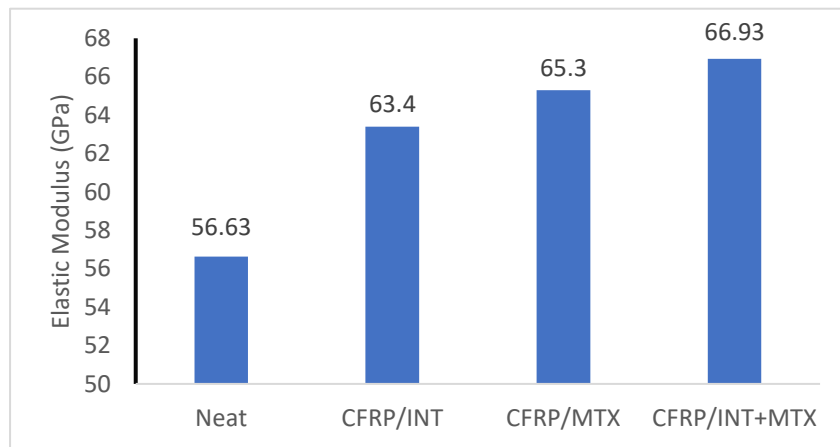


**Figure 2.9** Mean values of elastic modulus for the different arrangements of nano-integration in composite plates.

Another remarkable point is that the AE waves propagate faster in TEGO-integrated composites with respect to the reference neat composite. As the nano reinforcement strengthen the bonding between fibers and matrix, AE wave propagation was completed in remarkably shorter times. The young moduli evaluated with the tensile tests are provided in section 2.4.2.2. The elastic moduli of the neat, CFRP/INT, CFRP/MTX and CFRP/INT+MTX systems measured with destructive tests are 66 MPa, 69 MPa, 71 MPa and 69 MPa, respectively. The actual tensile test results differ roughly 5-15 % which is within an accepted range of error. The significance of this method was to evaluate Young's modulus without damaging the samples, which include lengthy and expensive production steps of nano material integration.

### **2.3.2.3 In- plane Electrical Conductivity Test**

One of the most crucial characteristics of graphene is its remarkable electrical conductivity due to its zero-band gap property [26]. Therefore, it is used for improving the electrical conductivity of the composite materials. Moreover, graphene has significantly high charge-carrier mobility of 2000–5000  $\text{cm}^2/\text{V s}$ . [27]. The combination of TEGO, fibers and polymer matrix pave the way for composites with genuine conductivity properties. These polymers can be utilized for different fields of applications such as electronic devices, conducting adhesives [28], long lasting batteries [29], and solar cells [30]. The conductivity of the material depends directly on the type of the fillers used for reinforcement. In the case of graphene, an uninterrupted layer is generated in the material, which supports the direct electron transfer [31].

To conduct the in-plane electrical conductivity tests on the four batches of composites (neat, fiber-matrix interface modified, resin-modified, and hybrid), two specimens from each composite plate were cut into 44 mm (length) x 10 mm (width) x 1.2 mm (thickness) dimensions. Edges of the specimens were ground with sandpaper until the fibers were exposed. After this step, specimens were covered with adhesive tapes, leaving small gaps from the edges. Those gaps specimen tips were painted with Flash Dry Silver Paint and left to dry. In electrical conductivity test, resistance of four different arrangements of nano material integration (the neat case, CFRP/INT, CFRP/MTX, CFRP/INT-MTX) was

measured with Tektronix DMM 4020 5-1/2 Digit multimeter (Figure 2.10). Electrical conductivity was calculated by;

$$R = \rho L/A \quad (2.3)$$

$$\sigma = 1/\rho \quad (2.4)$$

R: Electrical resistance

L: Length of the specimen

A: Cross sectional area

$\rho$ : Resistivity

$\sigma$ : Conductivity

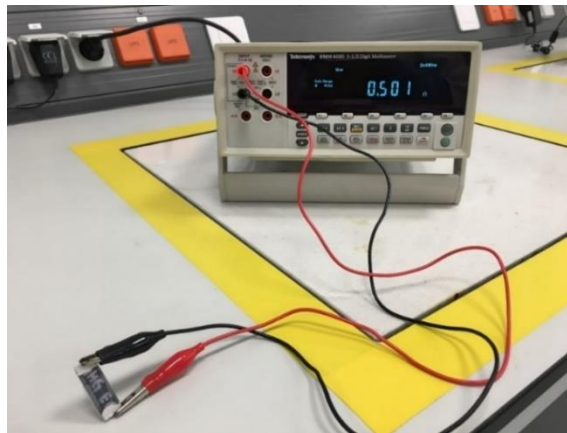


**Figure 2.10** Electrical conductivity test system.

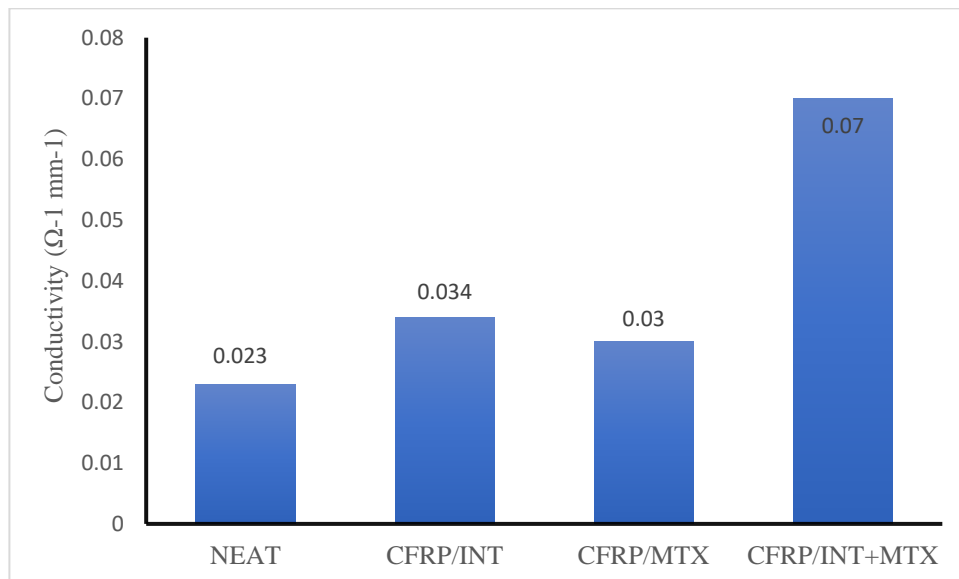


**Figure 2.11** Electrical conductivity test results.

Figure 2.11 depicts the results of the electrical conductivity tests for the four nano-reinforced composite arrangements. Neat CFRP plate has the lowest conductivity level ( $0.023 \Omega^{-1} \text{ mm}^{-1}$ ) as expected compared to the other systems. Carbon fiber is a conductive material by itself, however, introduction of an interface modifier, TEGO, increased the electron flow through the carbon fibers by a continuous interlayer maintaining direct electron transfer. In CFRP/MTX system, the conductivity increases to  $0.03 \Omega^{-1} \text{ mm}^{-1}$ , exceeding the neat level, however still less than the other two nano-modified arrangements (CFRP/INT or CFRP/INT-MTX). This indicates that the integration of TEGO into the matrix influences conductivity to an extent but not reaching the values achieved by TEGO-reinforced fibers (both CFRP/INT and CFRP/INT-MTX). This aspect can be explained with the TEGO forming conductive links between the Carbon fibers and creating new paths for electron flow [32]. The hybrid sample achieved the highest conductivity value, revealing that the combination of the matrix and the fiber nano-reinforcement by graphene oxide had a crucial role in electrical conductivity.

## **2.4.2 Mechanical Tests**

### **2.4.2.1 Mode I Fracture Toughness Energy Test**

Fracture toughness is an indicator of the stress level required by an existing imperfection in a material to advance further. Fracture toughness is an important property since it is not impossible to prevent the formation or advancement of these imperfections during the manufacturing, processing of the structure or its service life. These imperfections can be cracks, voids, metallurgical residuals, welding errors, design discontinuities or the combination of one or more of them. Since the engineers can never be sure of the perfection of a material, accepting the possibility of always-existing imperfections in a material and designing the structures accordingly is a lesson learned after numerous engineering catastrophes in history, which also made up of the Linear Elastic Fracture Mechanics (LEFM) approach. This approach considers the size and properties of the imperfection, the geometry of the host structure, loading conditions and fracture toughness as a material property, to measure its resistance against fracture [33].

While mode-I represents the most common case of loading (normal to the plane of crack) among the three modes of fracture, stress intensity factor  $K$  indicates the fracture toughness

of numerous materials. The critical fracture toughness value,  $K_{Ic}$ , is a material property independent of the material size or thickness. However, for the cases of thin plates, such as composites, other fracture parameters, such as energy release rate  $G$  or J-integral are evaluated with other tests. Materials with high fracture toughness energy indicates that more energy is required to completely fracture the material, leading to ductile fracture with considerable plastic deformation. Brittle fracture is observed in the materials which undergo little or no plastic deformation.

Composite materials may experience both brittle and ductile failure since they can have rather complex damage mechanisms which include interlaminar fracture, delamination, fiber-matrix debonding and fiber cracking [34]. Various types of failure mechanisms can be observed in fiber reinforced composites in Figure 2.12. Fiber breakage, matrix cracking and fiber bridging, and delamination can be listed as the common failure types occurring under Mode- I loading conditions in double cantilever beam test. These damage types might occur individually and concurrently.

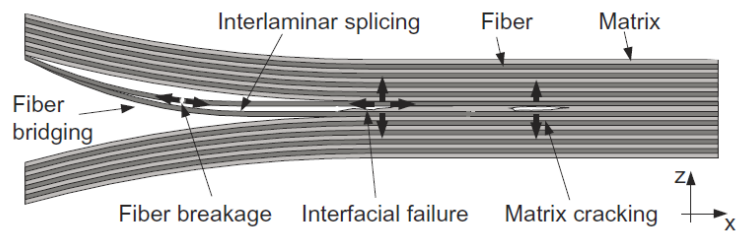


**Figure 2.12** Various failure mechanisms in fiber reinforced composites during mode I fracture toughness test [36].

At this point, mode-I fracture toughness energy test is a method to determine the resistance of a material to fracture, which plays crucial role in many design applications. Following the test standard of this test, EN 6033, composite plates were produced with Polytetrafluoroethylene (PTFE, Teflon) films of 120 mm x 10 mm x 0.02 mm dimensions in the mid-plane to facilitate the initiation of the first crack under the mode-I loading condition. Then, all specimens were cut and tabbed with aluminum hinges with 1 mm to 1.5 mm thickness range. All specimens were tested following the procedure described in the EN 6033 standard where the experiment is conducted under the cross-head speed of 10 mm/min until crack length reaches to 100 mm (Figure 2.13). Additionally, acoustic emission system

was used to identify the type of failure during these tests (Fig. 2.14). Two sensors were attached onto the specimen with a distance of 23 mm and 167 mm, respectively.

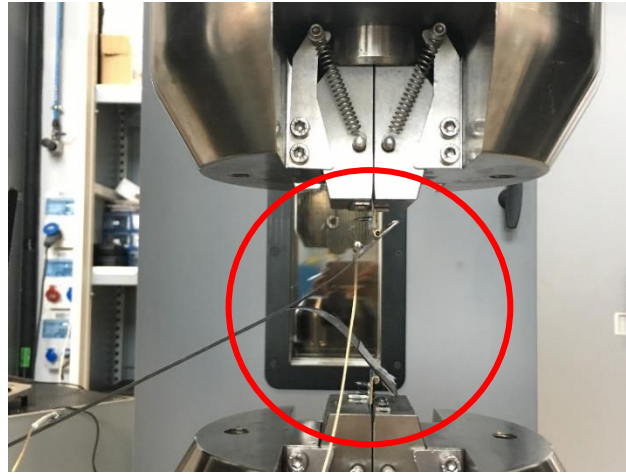


**Figure 2.13** Mode I fracture toughness test.

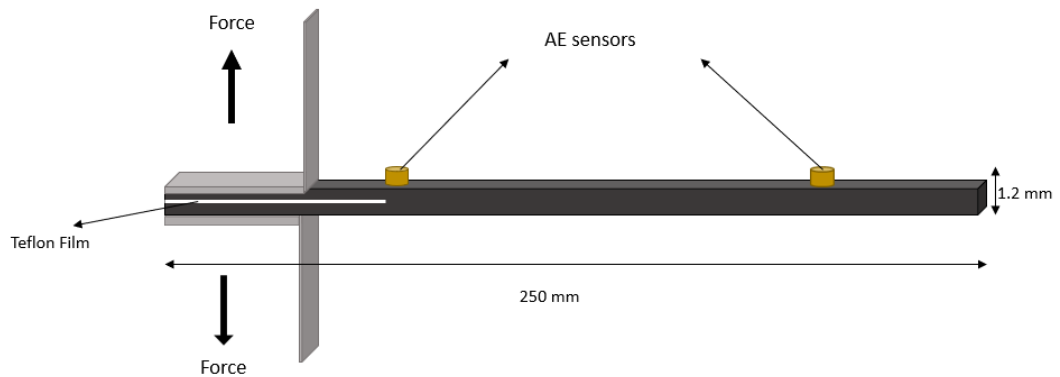


**Figure 2.14** The configuration of the mode I fracture toughness energy test setup with acoustic emission sensors.

For the calculation of the Mode I fracture toughness energy, the EN 6033 standard uses the following equation [39] ;

$$G_{IC} = \frac{A}{a \times w} \times 10^6 \quad (2.5)$$

$G_{IC}$  : fracture toughness energy, in  $J/m^2$ ;



A: the energy to achieve the total propagated crack length, in J, which is the area under the Load (N) and Cross Head Displacement (m) curve

a: the propagated crack length, in mm,

w: the width of the specimen, in mm.

**Table 2.4** Improvements in the fracture toughness energy.

<b>System</b>	<b>Interlaminar fracture toughness energy (J/m<sup>2</sup>)</b>	<b>Improvement (%)</b>
Neat	681	--
CFRP/INT	749	+ 10 %
CFRP/MTX	829	+ 21 %
CFRP/INT+MTX	672	- 1.5 %

Table 2.4 presents the average results of three mode I fracture toughness energy tests performed on the neat, CFRP/INT, CFRP/MTX, and CFRP/INT+MTX specimens. As expected, the neat specimens have low fracture toughness values with compared to the CFRP/INT, and CFRP/MTX cases due to the brittle nature of the unmodified matrix. The largest increase in fracture toughness energy from to neat level is observed in the CFRP/MTX, to be nearly 21%. These results suggest that the TEGO was dispersed into the matrix material uniformly and acted as crack arresting point , diverting the path of the propagating crack; thereby increased the amount of energy necessary for crack propagation. Moreover, the presence of TEGO in the matrix creates new paths for load transfer within the structure. As for the CFRP/INT system, there was a 10% increase in the interlaminar fracture toughness energy compared to the neat specimens. As was discussed with the SEM and microscopy images in the previous section, nano-phase integration on the fiber preforms led to rougher fiber surfaces with increased surface area. Therefore, fibers in CFRP/INT systems adhered better with the matrix material, bringing about an improvement in fracture toughness over the neat samples. The numerical data reveals that nano-phase integration is more effective in the CFRP/MTX than in CFRP/INT arrangement, suggesting that TEGO integration impacts the resin properties more dominantly that it does to fibers. With the addition of TEGO to the matrix material, the fracture toughness or crack propagation

resistance of the matrix increases, enabling improved load transfer onto the primary reinforcing fibers.

Unlike intuitively expected, CFRP/INT+MTX systems did not make any noticeable change or exhibit any notable improvement in fracture toughness energy values. This might be associated with the concept of agglomeration and localized accumulation of TEGO in the structure, as both the fiber surfaces and the matrix have nano-particles around/in them. This phenomenon can happen during various stages of the production of the composite plates: during the resin flow over the fibrous layers, or curing. The accumulated TEGO clusters can create a resistance to the uniform resin flow in the material, whereas the TEGO can agglomerate during the curing cycle since it was not functionalized chemically but only dispersed with mechanical mixing methods in the electrospaying solution. It is well known that when there is nonuniformity in the dispersion of nano-phases or any agglomeration present, fracture toughness and other mechanical properties drop since the net surface area for the load transfer decreases and these agglomerations behave as stress raisers in the structure [40].

When examining the fracture surfaces of the specimens subjected to mode-I fracture tests, it is observed that in all nano-phase integrated composite systems, the damage starts with fiber bridging (Fig. 2.15), grows with delamination and continues dominantly with the fiber breakage. The highest amount of fiber bridging occurs in CFRP/MTX specimens. The occurrence of fiber bridging mechanism is an indication for the improvement in fracture toughness since fiber bridging resists to the formation and progression of delamination leading to failure [38].



**Figure 2.15** Fiber bridging during mode I fracture toughness test.

In the microscopic images of both CFRP/INT and CFRP/INT+MTX systems, various size of holes can be seen within the microstructure as seen in Figure 2.16. The holes not being observed in the modified matrix systems show that these formations are clearly dependent to a damage phenomenon regarding the nano-modified interface. To understand the origin of these holes in terms of whether they are created during the manufacturing process or due to the damage formation, void content tests were conducted for each arrangement and no significant discrepancy was observed in the void content between nano-integrated and neat composites as tabulated in Table 2.5. This result bespeaks that the holes in question takes place during testing due to the damage formation.

**Table 2.5** Mean values of the data from the void content tests.

	Residual percentage (%)	Void Content (%)
NEAT	76.91	1.16
CFRP/INT	75.71	1.44
CFRP/MTX	76.71	1.06
CFRP/INT+MTX	76.40	0.95

Hole formations are related with the strong interaction and bonding between the graphene sheets covering the fibers and the epoxy resin system. Since the fiber surfaces are strongly bonded with the matrix, upon the formation of damage, graphene is separated from the surface of the reinforcing fiber due to the tension loading, and the plastic deformation in the resin material is interrupted, thus the fibers are broken and holes are left behind on the fractured surface. If the figure is examined in detail, one can notice that there is remnant reinforcing fibers across or over the holes, referred as bridge effect in literature. Rodbari et. al. suggested that the bridge effect can be seen in graphene integrated composites since the graphene has carboxylic acid functional groups in its structure, which creates intermolecular forces between its surface and reinforcing carbon fibers [41].

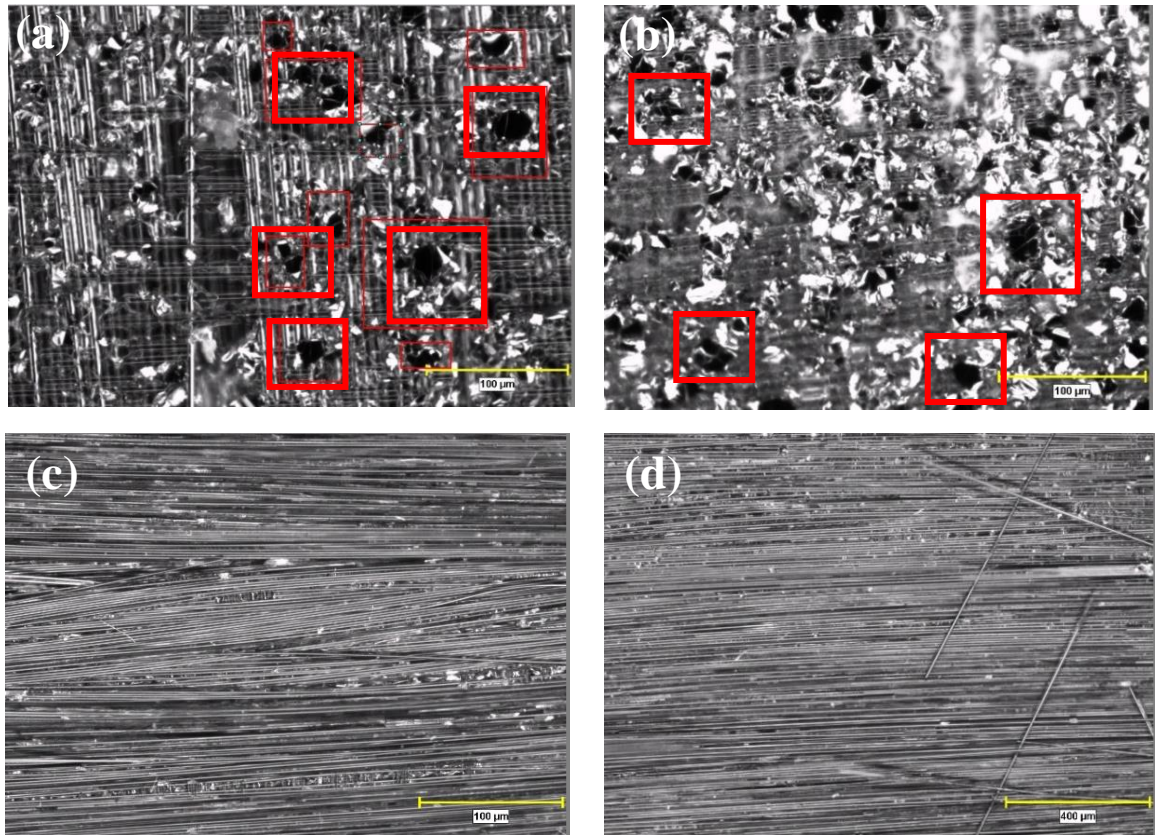


**Figure 2.16** Optical microscope images (100 μm) of (a) CFRP/INT and (b) CFRP/INT+MTX (c) Neat (Reference) (d) CFRP/MTX.

During fracture toughness energy tests, an interesting damage progression was observed only in CFRP/INT and CFRP/INT+MTX specimens where the damage or the fracture travels along the second ply and jumps onto the third ply, and switches between these plies as it progresses (Figure 2.17). For both CFRP/INT and CFRP/INT+MTX, the fracture path is rather rough and irregular. On the other hand, both neat and CFRP/MTX specimens (that have the highest  $G_{Ic}$  values, Table 2.2) exhibit planar fracture paths. This result clearly indicates that the TEGO integration improves the interfacial adhesion between the reinforcing fibers and the matrix material.

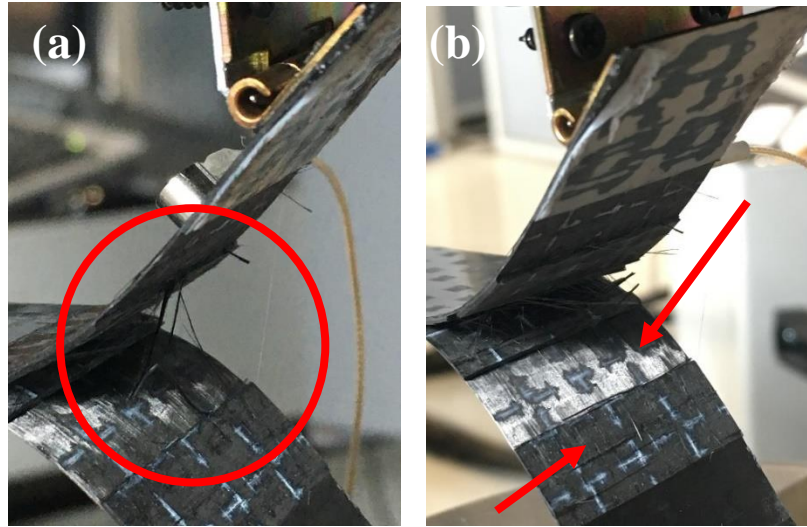


**Figure 2.17** (a) Fiber bridging and (b) interfacial failure in CFRP/INT system.

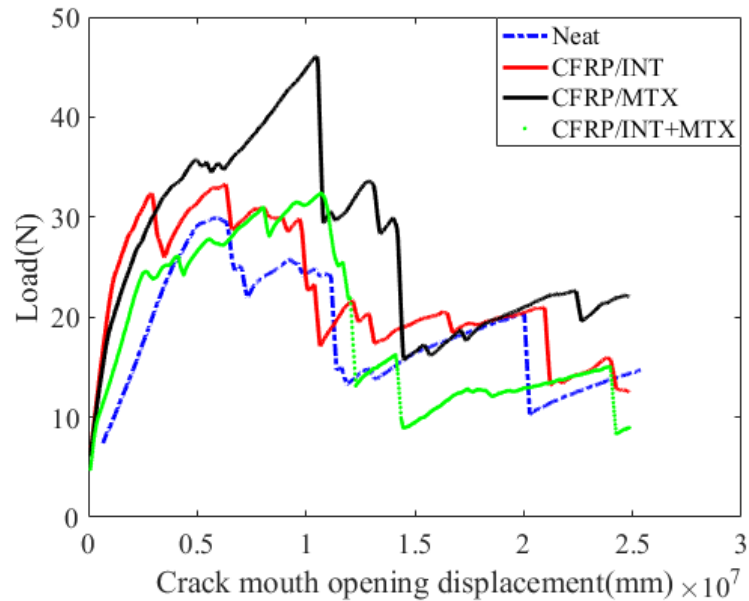


**Figure 2.18** Representative load vs. crack mouth opening displacement (CMOD) graph of Mode I fracture toughness energy test.

Figure 2.18 provides the load versus the crack opening displacement for all four composite configurations. The results indicate the critical aspect of matrix toughening with the help of nano-phase integration since the well dispersed TEGO can arrest matrix cracking thereby enable improved load transfer from the matrix to the fibers. An interesting observation is that at low loading levels, the fracture toughness of CFRP/INT is highest (i.e. CMOD being the least, as the resistance against crack advancement is the largest) of all the composite configurations proving that the TEGO integration enhances adhesion and hinders

the delamination. However, as the crack advances in the CFRP/INT system, it is observed that less load is required for damage propagation, which indicates the cracks in the matrix impacts the overall resistance to damage formation more dominantly than CFRP/INT+MTX arrangement. . A very sharp increase in the required load levels for a CMOD range between  $0.5-1 \cdot 10^{-7}$  mm, which is particularly significant for revealing the effect of TEGO in the plastic deformation behavior of the resin material, as it was not observed in the other TEGO arrangements. The load values of the CFRP/INT+MTX system being close to the neat specimens can be related to the agglomeration (as states in the previous discussion of the fracture energy curves of the composite systems) and wrinkling of the TEGO nano particles during the resin impregnation process. Wrinkles are known to occur on graphene sheets because of the instability of the 2D lattice structure. Large sized wrinkles in the large graphene sheets were also reported by other researchers [42]. The configuration of the wrinkled graphene sheets is preserved during the curing process of the epoxy system, as no chemical functionalization or further exfoliation of the nano-material was performed in this study. Therefore, stress concentration areas are formed due to the inhomogeneities and orderliness of the TEGO within the composite structure leading to decreases in efficiency of the load transfer, thus lowering the required load level for crack advancement.

The results of acoustic emission technique which was used during mode-I fracture toughness energy tests are provided in the next section, together with the AE results of the tensile tests.

#### **2.4.2.2 Tensile Test**

Tensile test is the most common mechanical test method to determine important material properties such as elastic modulus, Poisson's ratio, ultimate tensile strength, and strain at failure, among others. To compare the mechanical performance of the composite systems with each other and the neat material, tensile tests were conducted. In this study, all tensile test specimens were prepared and tested in accordance with ASTM D3039 standard [43]. Namely, the specimens were casted or cut into the dimensions of 250 mm (length) x 25 mm (width) x 1.2 mm (thickness). 50 mm x 25mm x 1 mm aluminum tabs were mounted on the ends of the samples for both surfaces through using Huntsman, Araldite® 2011 adhesive. To

ensure that test results are repeatable and reliable, three specimens for each composite configuration were tested. Biaxial strain gages manufactured by Micro – Measurements Company were used to measure both axial and transverse strain values to calculate Poisson’s ratio. The axial load was applied by INSTRON 5982 100 kN UTM to each composite specimen and the obtained data were processed with the related software. Moreover, acoustic emission system was used to identify the type of failure as used in mode I fracture toughness test. Two sensors were attached onto the specimen as 45 mm apart from each other. Figure 2.19 shows the tensile test specimen schematic and photo including the AE sensors attached.

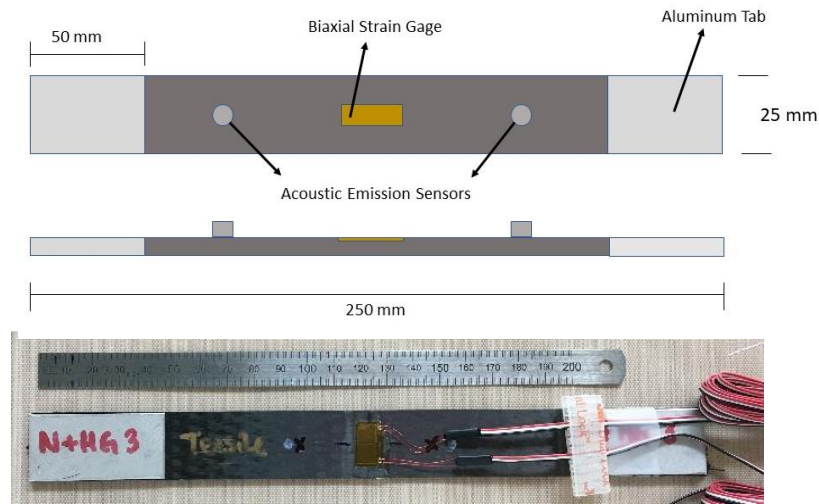


**Figure 2.19** Schematic for the tensile test, and the test specimen with biaxial strain gage attached and aluminum tabs.

**Table 2.6** Mean values of tensile test results.

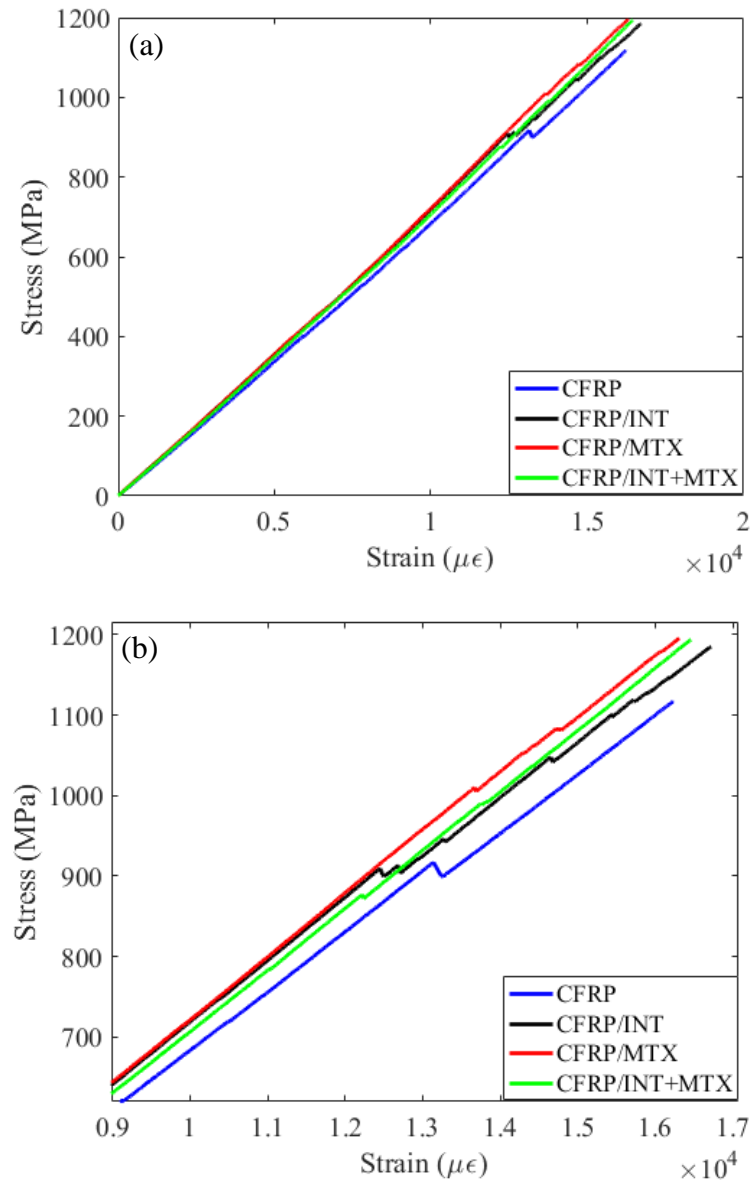
Type of Composite	Poisson's Ratio	Chord Modulus (MPa)	Max. Load (N) tensile	Extension at max. Load (mm)	Tensile Stress at max. Load (MPa)
NEAT	0.029	66951	33742	4.1	1117
CFRP/INT	0.041	69047	37065	4.24	1201
CFRP/MTX	0.032	71302	38561	4.39	1293
CFRP/INT+MTX	0.053	69675	39072	4.56	1268



Table 2.6 presents the measured and calculated values of Poisson's ratios, elastic moduli, tensile strengths for all the composite systems. For all the arrangements of nano-reinforced composites, tensile modulus and tensile strength values are higher than the neat composite specimens, as expected. For CFRP/INT specimens, there are 3 % and 10 % enhancement in tensile modulus and tensile strengths, respectively. These results reveal that the TEGO integration clearly enhanced the interfacial bonding strength of the interface-modified composite materials. Moreover, there are 6% and 14% improvement in tensile modulus and strength of the CFRP/MTX system, respectively. Comparing the results for CFRP/INT and CFRP/MTX shows that the matrix reinforcement is critical for obtaining higher elastic modulus for the composite system since the nano-integration elevates the load required for crack advancement in the matrix as discussed in the previous section, while improving the load transfer via the enhanced fiber-matrix interface in the CFRP/INT case raises the elastic modulus to some extent. The stress strain curves for all composite arrangements are provided in Figure 2.20 (a) and (b). The higher elastic modulus obtained from the nano-modified matrix system is also visible in this figure too (red line, close up view in Fig. 2.20 b).

In CFRP/INT+MTX, both from Table 2.6 and Fig. 2.20, 4% and 16% enhancement were observed in tensile modulus and strength compared to the neat system, however not as strikingly high levels of the other two nano-integrated systems. These results show that the enhancement in the matrix properties were dominant over the interface properties in tensile behavior of composites. This outcome is also inferred from the tensile properties of CFRP/MTX and CFRP/INT+MTX being close to each other. Additionally, TEGO has changed the matrix properties in a volumetric manner [44].





**Figure 2.20** (a) Tensile stress-strain graph consisting of CFRP with different nano-reinforcement configurations; (b) close-up view of the tensile stress-strain curves.

Examining the numerical values of tensile strengths in Table 2.6 further, the CFRP/MTX system has the highest tensile strength value (1293 MPa), implying that TEGO reinforcement improves the load transfer and bearing capacity of matrix which is also reported in the literature [45-47].

The drop-in stress seen in Figure 2.20 (b) is related to the notable damage formation in the composite material under loading. These drops appear the latest and in the smallest amounts in the CFRP/INT+MTX, not only a proof of TEGO integration increasing the load bearing capacity of the composite material, but also its durability against continuously forming damage in it. Considering the slopes of the curves, the CFRP/MTX system has the highest chord modulus value (Table 2.6), proving that the integration of the TEGO into the matrix is an efficacious way to make the composite structure stiffer compared to the other arrangements.

Experimental data presented in Table 2.6 also states that the load carrying capacity of the neat composite is the lowest compared to the other arrangements. Fiber breakage was commonly observed on the fracture surface (Figure 2.21 b). On the other hand, as seen in Figure 2.21 (c) and (d), holes prevail among the carbon fibers for which TEGO was used as an interface modifier (CFRP/INT and CFRP/INT-MTX). As previously discussed, holes were also observed in the optical microscope images of the failed CFRP/INT and CFRP/INT+MTX specimens of mode-I fracture toughness energy tests. Both the CFRP/INT and CFRP/INT+MTX systems show improvements in mechanical properties; however, the best results were obtained from the CFRP/ MTX arrangement.

From Table 2.6, is seen that the Poisson's ratio of CFRP/INT and CFRP/INT+MTX systems increased with respect to the neat sample, thanks to the interface modification of TEGO. It proves that the interphase modified composite materials are more ductile with respect to the neat and CFRP/MTX systems. During the tensile test, the matrix is the main load distributor across the fibers. When micro-damages such as matrix cracking occur during tensile testing, the axial load transfer from the matrix to the fibers will be degraded greatly, thus the load will no longer be uniformly distributed in the longitudinal direction and axial strain immediately reduces. Consequently, Poisson's ratio increases in both systems. This will be discussed further with the Poisson's ratio vs. axial strain curves of the nano-integrated composite systems.

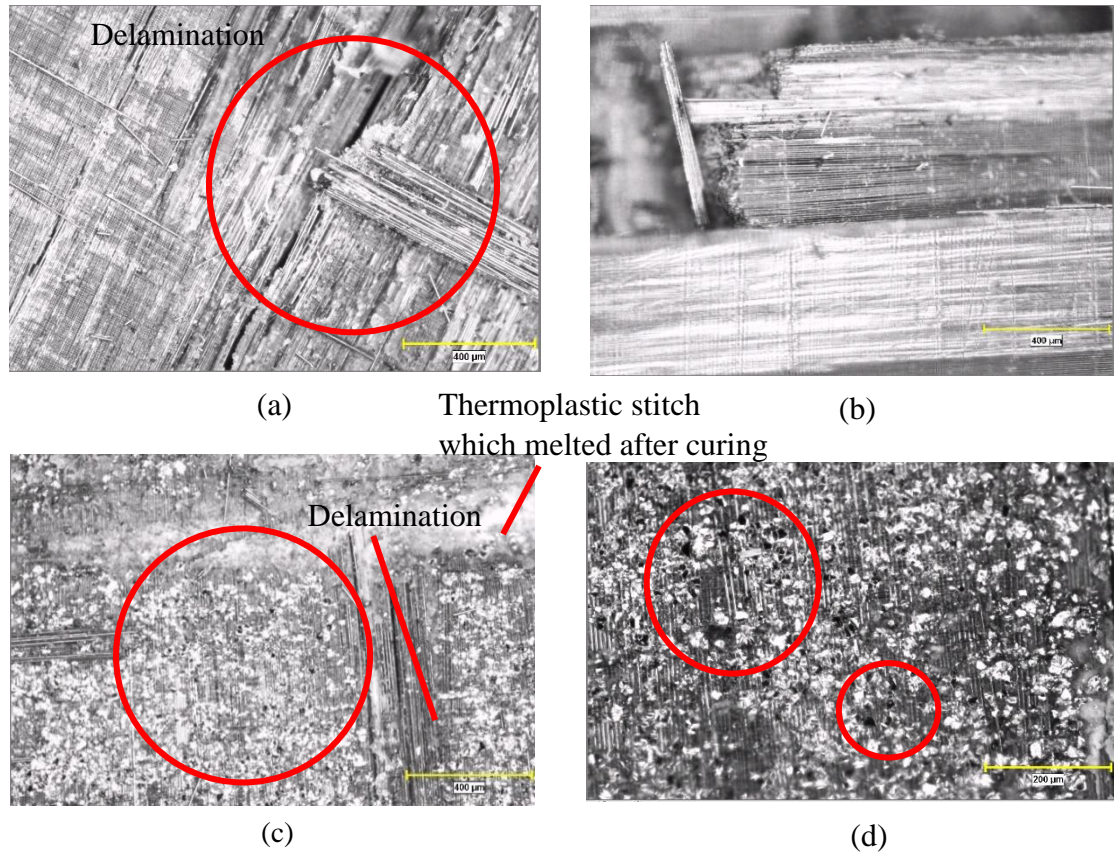


**Figure 2.21** Optical microscope images of (a), (b) fiber cracking of neat specimen after tensile test (c) holes on CFRP/INT (d) holes on CFRP/INT+MTX.

During the tensile tests, it was observed that the specimens fail with different fracture profiles from shattered to split types of failure (Figure 2.22).

It is common to observe both shattered and split types of failure in unidirectional composite specimens. It indicates  $90^\circ$  fiber orientation in our ply orientation had no effect on the type of failure. meaning that  $0^\circ$ -degree plies dominated the failure mechanisms under tensile loading.

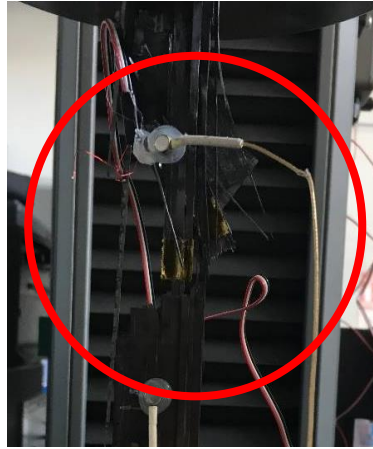


**Figure 2.22** Tensile specimen with shattered and failure with splits failure.

Another important finding of the tensile tests is the Poisson's ratio for the composite systems: The aim of evaluating Poisson's ratio is to understand the resistance of the material to deform along the longitudinal and transverse directions, or to the volumetric changes under tensile loadings. Brittle materials normally have the lowest Poisson's ratios due to their low molecular mobilities, thus their low capacity of plastic deformation. In contrast, ductile materials have opposite characteristics, ability to deform plastically in various directions. Here the Poisson's ratio values were evaluated with the well-known expression,

$$\nu_{xy} = -\frac{\epsilon_y}{\epsilon_x} \quad (2.6)$$

for which biaxial strain gages were employed to measure both axial ( $\epsilon_x$ ), and transverse ( $\epsilon_y$ ) strains simultaneously. Strain gages were directly connected to the data acquisition ports of INSTRON 5982 100 kN UTM platform to record the change in extension along the x-and y-directions.

Examining the evaluated values for the four arrangements in Table 2.4, the neat specimens have the lowest Poisson's ratio values. CFRP/MTX arrangement experiences an increase in the Poisson's ratio to an extent (0.032), however, both in CFRP/INT and CFRP/INT-MTX systems, there is a notable increase in Poisson's ratios (0.042 and 0.053). In other words, TEGO integration made the composite more ductile with respect to the neat composite system. According to molecular dynamics simulations in literature, graphene influences the enhancement of shock strength [48-50] and ductility [51-52] when integrated in composites. The variation of Poisson's ratio values with respect to the axial strain is presented in Figure 2.23.

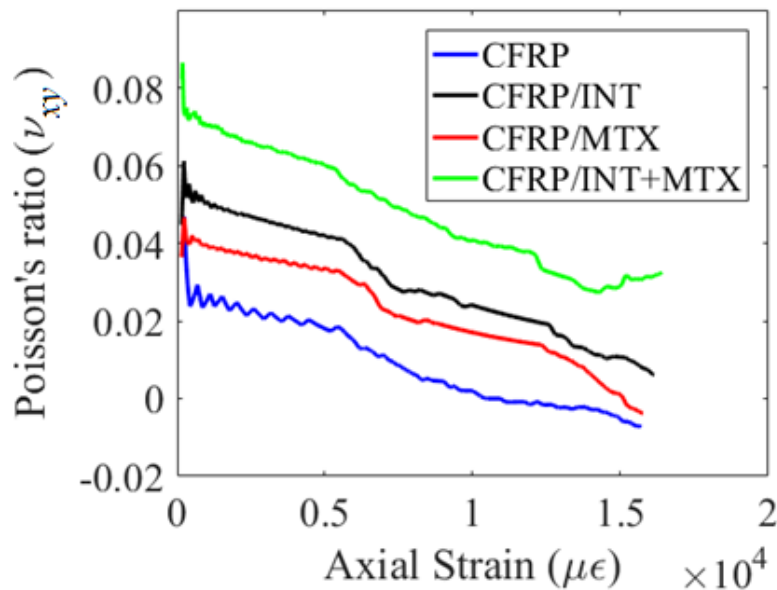


**Figure 2.23** Representative Poisson's ratio vs. axial strain graph for each CFRP arrangement with different nano-reinforcement configurations.

From the figure, it is seen that the reduction in Poisson's ratio with increasing axial strain follows the similar trend for all composite configurations, with minor exceptions. The difference between initial and final data points is approximately 0.04 and the axial strain of failure is also nearly the same for all specimens (approximately  $1.5 \mu\epsilon$ ).

However, for a fixed value of axial strain ( $\epsilon_x$ ), the highest  $\nu_{xy}$  (absolute) value is observed for CFRP/INT+MTX system, followed by the CFRP/INT sample, and the lowest one for the neat specimen. This indicates that the fiber-matrix interface modification with TEGO enables

the microstructure to achieve higher transverse strain values during axial loading; while this effect is limited for the matrix-modified CFRP/MTX specimens. Except the hybrid system, all composite arrangements suffer from a sharp drop in the Poisson's ratio at 0.55-0.65  $\mu\epsilon$ , indicating that the combined effect of fiber-matrix interface and matrix modification overcomes this critical level of axial strain. The initial sharp drop observed in all curves are associated with the initial matrix cracks which formed in all composites and the fluctuations are related to the connection of strain gages on the specimens. The last diverting part seen in CFRP/INT+MTX curve is due to the detachment of the strain gage from the specimen surface. The decrease in the Poisson's ratio can be associated with the formation of transverse cracks [92], which increase the elongation along the loading direction, and diminish the contraction along the lateral direction with the reduction in the transfer of axial load onto the lateral direction [93]. The detailed explanation was made with the acoustic emission results in Section 2.4.2.3.

To conclude, using graphene both as a matrix and as an interface modifier plays an important role in the mechanical performance of the carbon fiber reinforced composites. The load transfer mechanisms were enhanced upon the increase in the interfacial bonding between fibers and the matrix.

#### **2.4.2.3 Evaluation of acoustic emission for Mode I Fracture Toughness and Tensile Tests**

Acoustic Emission (AE) technique was employed during mode-I fracture toughness energy and tensile tests to identify the failure mechanisms of the specimens. Acoustic emission focuses on the number of clusters and the number of hits which are recorded during the destructive or nondestructive (artificial wave propagation) tests, all representing different failure types and micro crack formations, respectively. Micro damages that occur during destructive tests generate elastic waves, which are collected by the wide band piezo-electric sensors attached on the specimens. 40 dB was specified as the threshold level to eliminate the signals received below this value, and Bessel band pass filter was used to exclude the noise in the obtained signal. The selected filter range was defined between 20 to 800 kHz [91]. Defining a filter range allows focusing on the locations of high density signals. The

software used for the noise removal and feature extraction for the post processing of the raw signal data is titled as Noesis and was provided by the research center infrastructure. In this work, the targeted features were weighted peak frequency ( $f_{wp}$ ) and partial power 4 (PP4). The weighted peak frequency is calculated by the following formula.

$$f_{wp} = \sqrt{f_{peak} * f_{centroid}} \quad (2.7)$$

$f_{peak}$ : peak frequency represents the maximum frequency in the power spectrum

$$f_{centroid} = \frac{\sum \text{frequency} * \text{magnitude}}{\sum \text{magnitude}} \quad (2.8)$$

Partial power 4: percentage of energy at the selected frequency range

ELKI software was used for clustering the acoustic emission data. The k- mean elkan algorithm and Minkowski squared Euclidean distance function were applied to distinguish the failure mechanisms inside the specimens. The signals acquired from mode I fracture toughness tests make up three different clusters, which are shown in Figure 2.24. . These three clusters represent the matrix cracking, interface failure and fiber breakage, respectively. Each micro-damage that occurs during the tests create a signal with a different frequency range. As seen in Figure 2.24 (a, b, c, d), the first cluster varies in between 90 - 250 kHz, the second cluster varies between 250 - 450 kHz, and the last cluster varies between 450 - 650 kHz. Figure 2.24 allows for a comparison of the damage events and their happening density for each of the composite arrangements. The neat sample includes a high amount of matrix cracking (shown in red), followed by again a dense formation of damage in the fiber-matrix interface, which causes a fast degradation in load transferring capability of the composite; and finally, a high amount of fiber rupture leading to global failure. Comparing the CFRP/INT system with the neat case, the amount of damage events happening at the interface is significantly decreased, which is a clear indication of TEGO effect at the fiber-matrix interface. TEGO enabling a strong adherence to the matrix also effect the matrix cracking events partially, however that type of damage is more significantly prevented greatly in the CFRP/MTX (Fig. 2.24 c). The CFRP/INT+MTX system, on the other hand, provided  $G_{Ic}$  values close to the neat sample during the test, which is also reflected in the AE results. The nano-modification at both the interface and the matrix led to agglomerations and localized TEGO-dense regions, giving fracture toughness energy values close to neat values. So, the

enhancements observed in modified interface and matrix systems cannot be obtained in the samples of combined modification.

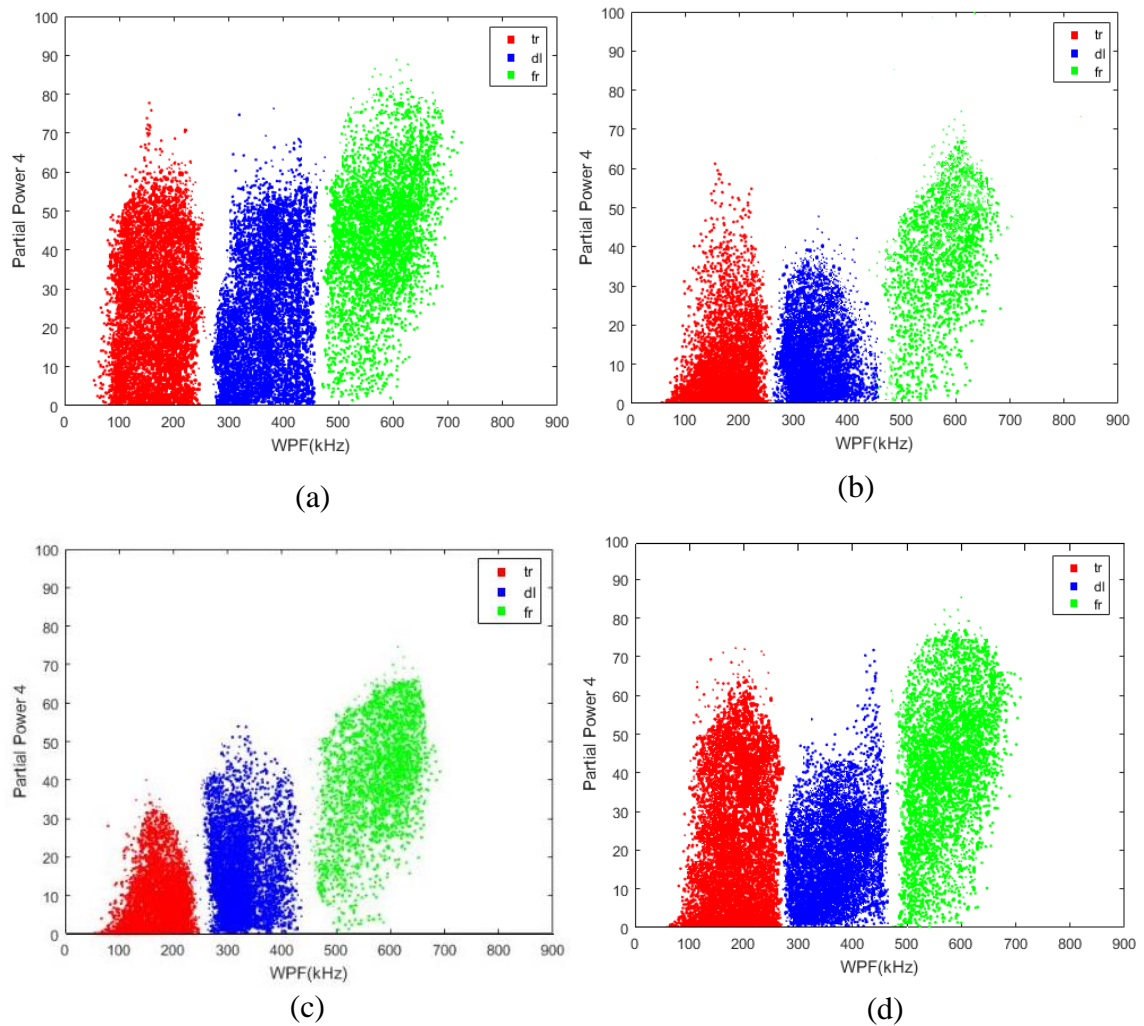


**Figure 2.24** Representative scatter plot of partial power 4 vs. weighted peak frequency of (a) neat (b) CFRP/INT (c) CFRP/MTX and (d) CFRP/INT+MTX for mode I fracture toughness test.

Additionally, partial power 4 (PP4) values which represent the energy release during failure declined for the cases of CFRP/INT and CFRP/MTX cases due to the TEGO integration into interface and matrix of the composite structure. Uniformly distributed TEGO sheets also absorb the released fracture energy during failure, as more fiber rupture events at higher PP4 regions are clustered for the CFRP/MTX samples compared to CFRP/INT ones. For the CFRP/INT+MTX arrangement, there was % 1.5 decrease in fracture toughness energy with respect to the neat specimen. Comparing Figure 2.24 (a) and (d), nearly the same cluster



formations are observed for both neat and CFRP/INT+MTX systems. As a difference, the second cluster, representing interface failure events, have a smaller size for the hybrid composite, but the total number of hits will give more information regarding this point.

Another interpretation for acoustic emission data is the relation between micro damage types and the number of hits. As seen in Figure 2.24, each dot represents a micro cracking event that formed during testing and each cluster are formed by the gathering of micro damage formations. Yilmaz et. al. calculated the number of hits with the following formula [99],

$$\hat{H}_t^s = \sum_{j=1}^{j=N} H_{t,j}^s / N \quad (2.9)$$

$\hat{H}_t^s$ : the cumulative hit number of  $j$ th specimen for all arrangements

$t$ : micro damage types such as  $tr$ : transverse cracking,  $dl$ : interface failure and  $fr$ : fiber rupture,

$s$ : arrangement type

$N$ : number of specimens,

Total number of specimens for each arrangement are 3.

The number of total hit number for each arrangement as follows:

$\hat{H}_t^{CFRP/INT+MTX} > \hat{H}_t^{Neat} > \hat{H}_t^{CFRP/INT} > \hat{H}_t^{CFRP/MTX}$ . For convenience, the mode-I fracture toughness energy test results (Table 2.2) are provided below. Considering  $G_{Ic}$  values of the systems, the total hit number (damage events) will be the highest for the lowest  $G_{Ic}$  values. These results of acoustic emission are consistent with the mechanical test results.

As seen in Figure 2.25, the number of hits, in other words, number of all types of damage events for both CFRP/INT and CFRP/MTX specimens are significantly less than the neat specimen. While the matrix cracking events (shown in dark blue) dropped sharply in CFRP/MTX samples, number of hits of the interface failure notably decreased for the case of CFRP/INT samples, due to the interface modification. As mentioned previously, the TEGO sheets that were electrosprayed on the surface of the carbon fibers increased the bonding between fiber and matrix, enabling fiber bridging under mode I fracture toughness tests, which indicates resistance to the formation and propagation of the delamination.

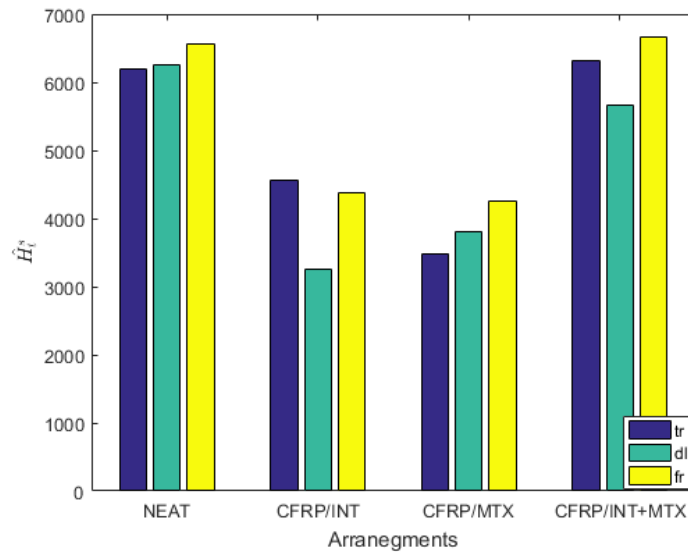


**Figure 2.25** The average number of hits for mode I fracture toughness test with three micro damage types for each arrangement.

On the other hand, in CFRP/MTX specimen, number of hits representing transverse cracking decreased because of the matrix modification. Dispersed TEGO sheets in matrix acts as crack arresting point and at the same time it creates new paths for load transfer within the composite structure. Comparing the fiber rupture failure type, nano-modified samples have again a smaller number of hits over the neat material.

Since the damage event clusters in the scattered plots for the hybrid composite (Figure 2.24 d) remained close to the neat specimen (Figure 2.24 a), comparing the number of hits for these two samples (Figure 2.25) will provide valuable numerical information. It was seen that the number of hits for the 3 clusters in the CFRP/INT+MTX sample are more than the neat specimen. Referring to Table 2.2, there wasn't any notable improvement in fracture toughness energy values of the CFRP/INT+MTX system, which was related to the agglomeration of TEGO in the microstructure, causing stress concentration areas and changing the flow regime of the resin during impregnation.

The scatter plots for all composite arrangements during the tensile tests are presented in Figure 2.26, and the number of hits for the three types of damage events in Figure 2.27 respectively. In Figure 2.26, the first cluster which represents the matrix cracking varies between 100 - 250 kHz, second cluster representing the interface failure varies between 300

- 400 kHz, and the last cluster varies between 400 - 500 kHz which represents the fiber rupture. The ranges of weighted peak frequencies for different types of damage events are higher than those of the mode-I fracture toughness energy tests, as the tensile test does not include any pre-crack formation (i.e. PTFE film insertion in the mid-layers) in the specimen, meaning that the test method has to damage a theoretically undamaged material with a higher level of load.

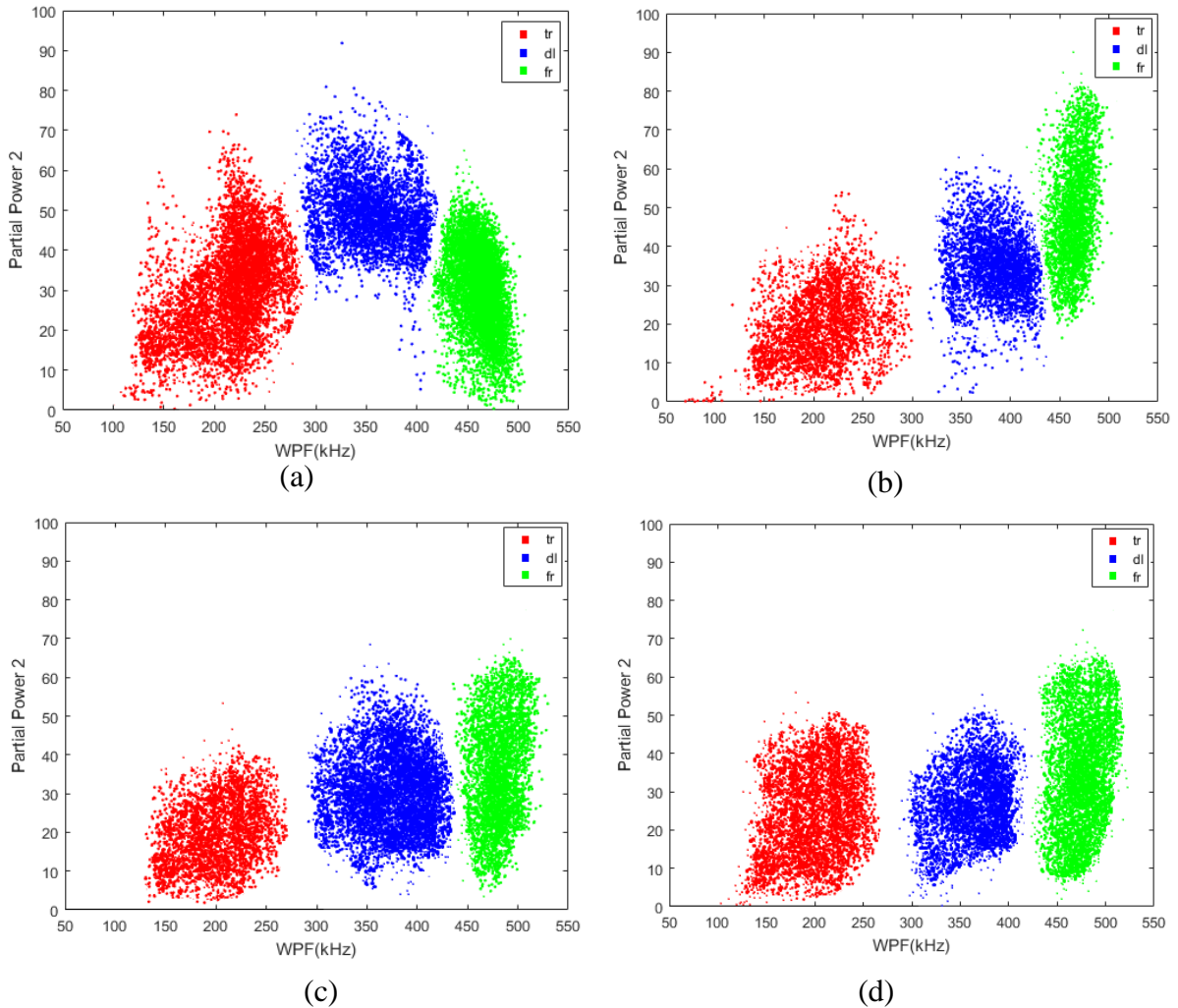


**Figure 2.26** Representative scatter plot of partial power 2 vs. weighted peak frequency of (a) neat (b) CFRP/INT (c) CFRP/MTX and (d) CFRP/INT+MTX for tensile test.

Comparing the neat sample and interface-modified specimen in Figure 2.26 (a) and (d), the amount of matrix cracking (shown in red dots) is decreased, and the interface failure events (dots in dark blue) happened at higher energy levels for the CFRP/INT due to TEGO integration. The latter enhancement is not observed for the case of matrix modified composite (CFRP/MTX, Figure 2.26 c) as there is no nano-reinforcement in the fiber-matrix interface, so the matrix cracking events follow a similar tendency to the neat specimen. Referring to table 2.4, 7% improvement was obtained in tensile stress at maximum load level in the CFRP/INT samples, due to the enhancement in the interfacial bonding strength of the composite material with the TEGO integration. This can be viewed in the third cluster in the scatter plot of the same sample (Figure 2.26 b) in which the highest energy release is observed— during fiber rupture as expected. Fiber rupture is well known to occur at the highest stress values since the matrix consists enough cracks at that point and there happened enough interface failure to let any load transfer to fibers, and this is followed by global failure.

In CFRP/MTX system, TEGO modification was enhanced the tensile stress 15% according to reference neat specimen, which also has a similar improvement in the third cluster. The matrix cracking also decreased slightly in amount over the neat case.

The hybrid composite, which showed no significant improvement in mode I fracture toughness energy, also gave similar damage scatter to the neat case, only with the interface damage events happening at lower energy levels (Figure 2.26 d; shown in dark blue dots), indicating the localized TEGO-rich regions are clustered especially in the fiber-matrix interface, acting as stress raisers. On the other hand, a slight enhancement in the third cluster (fiber rupture) can be seen for the CFRP/INT+MTX sample, in comparison to the neat specimen, meaning that the tensile loading allows for the TEGO effect to arise in the microstructure in spite of agglomerations opposite to the mode-I fracture toughness energy tests.

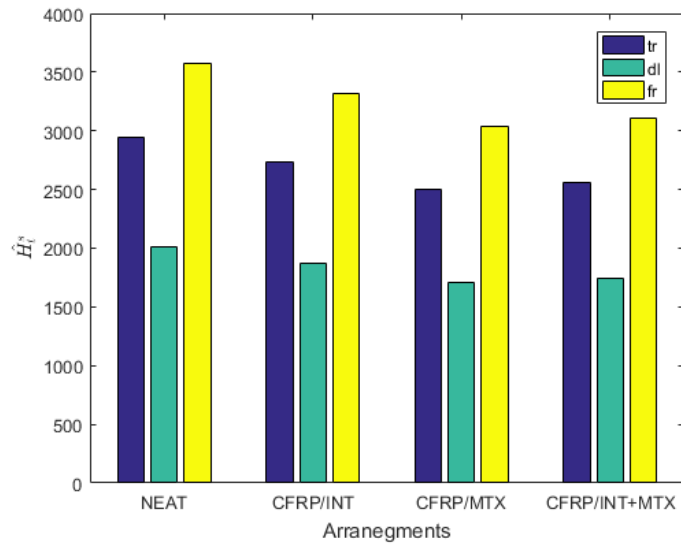


**Figure 2.27** The average number of hits for tensile test with three micro damage types for each arrangement.

Figure 2.27 provides the total hit numbers for each type of damage event in all four composite arrangements. The number of total hit number for each arrangement is as follows:

$$\hat{H}_t^{NEAT} > \hat{H}_t^{NCFRP/INT} > \hat{H}_t^{CFRP/INT+MTX} > \hat{H}_t^{CFRP/MTX}$$

In the figure, the decrease in the hit numbers representing the transverse cracking (in dark blue) can be seen in the CFRP/MTX system due to the TEGO modification as it dispersed in the matrix. The matrix cracking amount is the most serious in the neat sample, followed by CFRP/INT where no nano-integration in the matrix exists, thirdly in the hybrid sample, and in CFRP/MTX the least. These slight differences are the most visible with number of hits graphics rather than the scatter plots.

The hits indicating the interface failure gradually decreases with the TEGO integration in the systems, with matrix-modified sample slightly less than the interface-modified composite, both of which are less than the neat level. The decrease in the number of hits for CFRP/INT specimen can be related with the interface modification in composite structure. Here the higher decrease would be expected for the CFRP/INT specimen, however the TEGO dispersed matrix exhibits a more dominant improvement. The same phenomenon is visible

for the cases of hybrid sample and the matrix-modified sample, as the number of hits regarding the fiber ruptures are lower for CFRP/MTX.

Moreover, the slight difference between the number of hits of CFRP/MTX and CFRP/INT+MTX system proves that the matrix properties dominates the failure mechanism with respect to the interface properties under tensile loading.

Mechanical test results indicated that the Poisson's ratio of CFRP/INT and CFRP/INT+MTX systems were increased due to interface modification of TEGO. It proves that the interphase modified composite materials are more ductile with respect to the neat and CFRP/MTX systems. In tensile test, matrix is the main load distributor across the fibers. When matrix contains any micro-damages or agglomerations; during tensile testing, the axial load won't be uniformly distributed in the transverse direction which led the transverse crack formations. However, in CFRP/INT+MTX system the formation of the transverse cracks are prevented by the strong interaction between graphene sheets and carbon fibers. Strongly bonded graphene sheets on the fibers act as a crack bridge and resist the formation of the transverse cracks that occurred in 90° oriented mid plies. Therefore, the transverse strain will directly reduce, consequently, Poisson's ratio increased in both systems which TEGO sheets used as an interface modifier.

To sum up, acoustic emission results validate the mechanical test results by clarifying the types and order of failure in terms of energy levels and number of hits indicating the damage events that occurred in the composites under mode-I fracture toughness energy and tensile tests.

#### **2.4.2.3 Compression Test**

Compression test is a method to measure the compressive strength and stiffness of the CFRP by using combined compression loadings. It was aimed to investigate the effect of TEGO reinforcement on the compressive properties of the composites. For this purpose, all specimens are prepared and tested in accordance with ASTM D6641/ D6641M standards. The specimens were cut into the dimensions of 140 mm (length) x 12 mm (width) x 1.2 mm (thickness) (Figure 2.28). The gage length was chosen to be 12.7 mm to avoid Euler buckling. For the compression test, composite tabs composed of 6 layers of  $\pm 45^\circ$  oriented

unidirectional carbon fiber prepregs with the dimensions of 50 mm x 25mm x 1.8 mm with were glued on the specimens with Huntsman, Araldite® 2011 adhesive. Axial strain gage from Micro-Measurements Company was mounted at the center of the specimen to measure axial strain. Specimens were axially loaded under compression using the INSTRON 5982 100 kN UTM system.

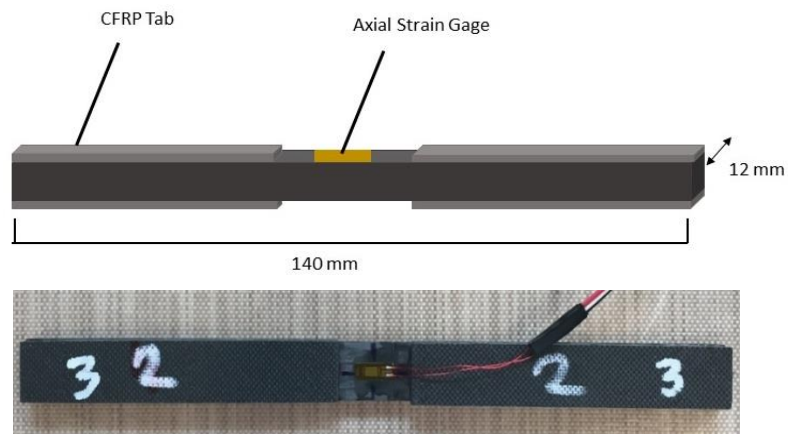


**Figure 2.28** Schematic for the compression test specimen.

For carbon fiber reinforced polymers subjected to compressive loading, failure generally starts with micro buckling. Rosen et al claims that there are two types of micro buckling: in-phase micro buckling for higher fiber volume fractions and out-of-phase micro buckling for lower fiber volume fractions [53]. In-phase micro buckling causes kink-band formation as the load increases (Figure 2.29).

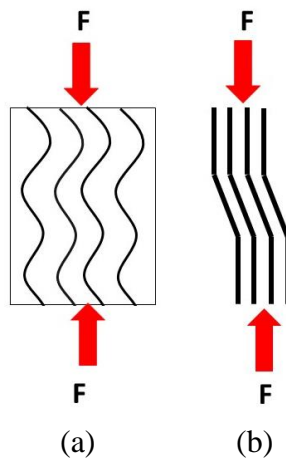


**Figure 2.29** Schematic representation of (a) in-phase buckling, and (b) kink- band formation under axial compressive loading.

Figure 2.31 presents the stress-strain curves for the four different composite systems. Here the chord modulus of the tested specimens are calculated as the slopes of the stress-strain curves between 0.1 -0.3%  $\mu\epsilon$  ranges. It can be stated that the chord moduli of the CFRP/INT and CFRP/INT- MTX arrangements were improved by 17% and 21%, respectively. Furthermore, there was an 8% enhancement observed in the CRRP/MTX system. These results imply that the interphase modification dominates the mechanical behavior of the composites under compression. However, there was a sudden drop, 11% decrease in the maximum compressive stress level achieved in CFRP/INT (Figure 2.30). The reason behind this decrease in stress values might be the formation of holes [54, 55] and local fiber misalignments [56].

As mentioned in the previous sections, in CFRP/INT and CFRP/INT+MTX systems, unexpected hole formations were observed on the damaged plies after testing. These holes were formed only in two arrangements which include the electro spraying of the fibers with TEGO (Figure 2.31). This phenomena was explained in detail Section 2.4.2.1.

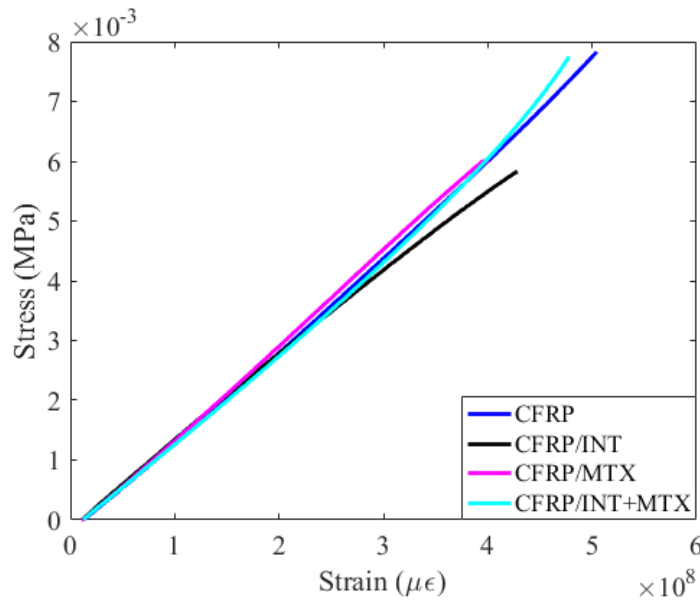


**Figure 2.30** Stress - strain curves of the axial compression test of the four different composite arrangements.



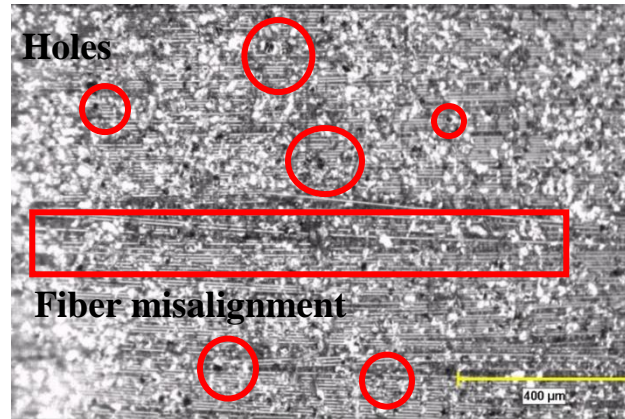


**Figure 2.31** Optical microscope view of the hole formations and fiber misalignment in CFRP/INT from the axial compression test specimen.

Another reason for the decrease in compression strength values for the CFRP/INT system is the delamination observed as an interfacial failure mechanism. Generally, delamination was observed at the edges of two layers, due to the high peel stress levels [57] (Figure 2.32).

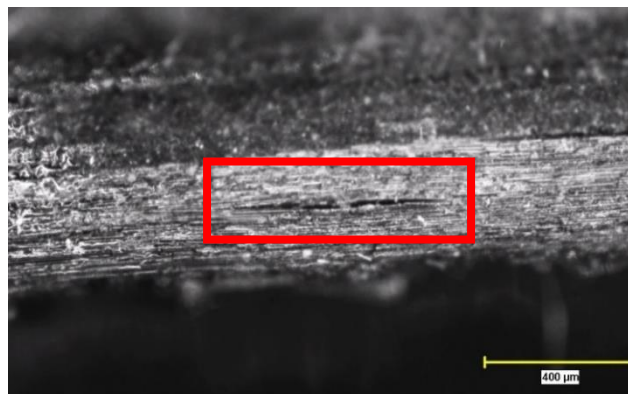


**Figure 2.32** Optical microscope image of the CFRP/INT specimen cross section.

The damage mechanisms occurring during the axial compression test can be stated as follows: the damage starts with fiber micro buckling and it causes kink band formation in those regions, it is then followed by delamination. The optical microscopy images of the specimens belonging to CRRP/MTX system proved that in-phase micro buckling occurred during testing and consequently the kink- band formation was observed, as shown in Figure 2.33. When the load was released, the micro buckling disappeared slowly from the structures, or turned into kink band formations.

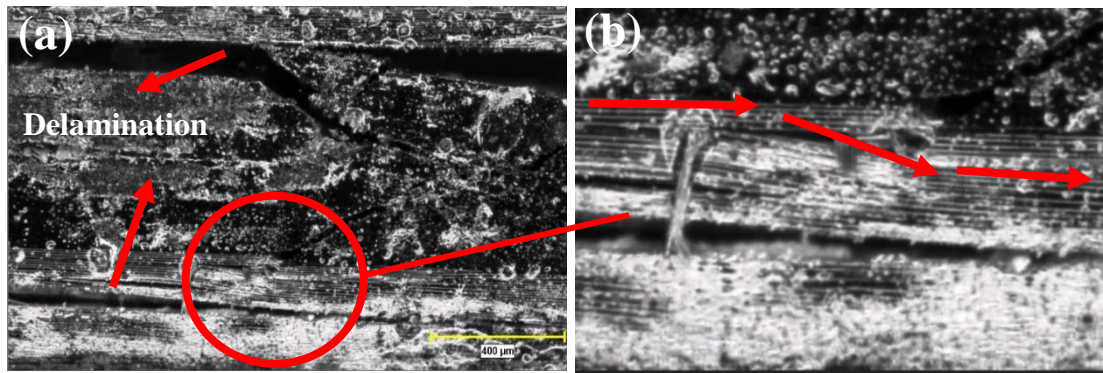


**Figure 2.33** (a) Delamination growth and fiber kink formation in CFRP/MTX (b) detailed view of fiber kink formation.

Additionally, Greenhalgh et al. claimed that the delamination movement becomes vital especially through different interfaces [58]. In their study, they reported that the propagation speed is directly proportional with size of the damage area. Fast delamination growth causes large delamination areas when the fiber orientation and the delamination driving force are in the same direction. The stacking sequence of the composite in this study is  $0^\circ/90^\circ/90^\circ/0^\circ$ , whereas the direction of loading is the same with the fiber orientation of the outer ply ( $0^\circ$ ). Delamination growth was observed in the  $90^\circ$  plies, which were the mid-ply of the composite. According to Leopold et al [59], delamination propagation happens in plies that are transverse to the loading direction, which is also observed in this study.

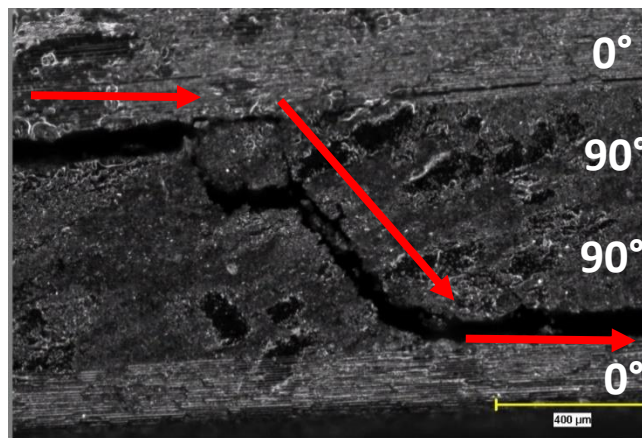


**Figure 2.34** Optical microscope image of cross section view of CFRP/MTX damaged specimen, arrows indicating the path of advancing crack.

From Figure 2.28 the crack path is obviously seen. The shape of the crack path shows that there was a matrix failure at the mid-ply which were oriented in  $90^\circ$ , as those fibers were not in the same direction with the loading of the specimen. Therefore, the matrix directly failed in those two plies and the crack continued its propagation along  $0^\circ$  fibers lying along the loading direction.

To sum up, kink band formation in fibers and consequently the delamination were the main failure types observed in the damaged specimens after conducting the axial compression tests. The decrease in stress-strain values in all TEGO-integrated arrangements showed that the hole formation might be the one of the critical factor that changes the course of the test.

#### 2.4.2.4 Flexural Properties - 3 Point Bending Test

Flexural properties play a crucial role in the understanding matrix-fiber interactions, in addition to the mechanical properties of the composite materials. According to ASTM D790-3 test standard, the specimen dimensions should be 50.8 mm(length) x 12.7 mm(width) x 1.2 mm (thickness) to perform the testing for composites with thickness values less than 1.6 mm. Three specimens from each arrangement were tested in this setup. The load was applied by INSTRON 5982 5 kN UTM to each group of specimens to examine their flexural properties (Figure 2.34).

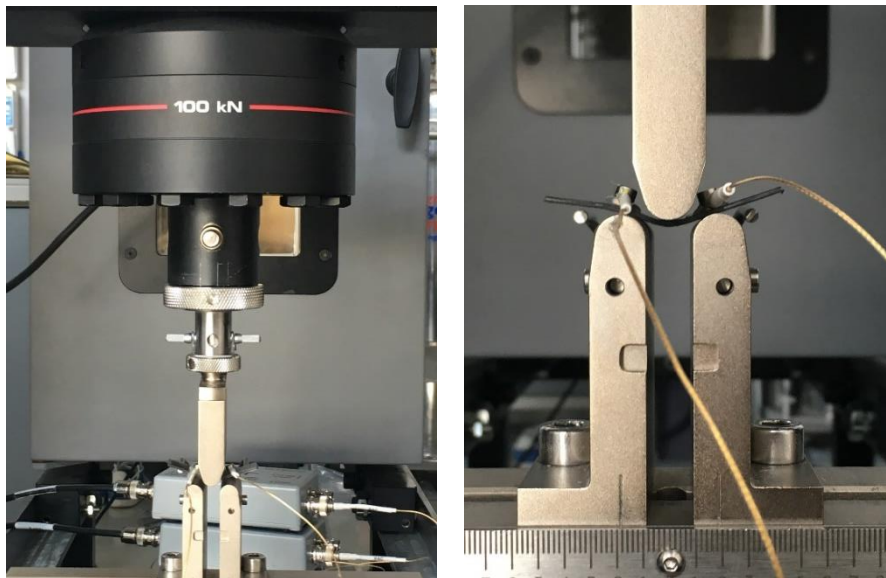


*Figure 2.35* Three-point bending test.

Flexural modulus represents the trend of the material towards bending, and the flexural strength indicates the material's resistance to the fracture while subjected to bending loads. The results of the 3-point bending tests conducted for all types of arrangements are provided in Table 2.7.

**Table 2.7** Flexural properties of the test specimens.

	Flexural Strength (MPa)	Flexural Strength improvement (%)	Flexural Modulus (MPa)	Flexural Modulus improvement (%)
NEAT	546	---	14400	---
CFRP/INT	585	7	19075	32
CFRP/MTX	702	28	18475	28
CFRP/INT+MTX	564	3	18255	26

Examining the results, compared to the neat composite, there is a 7% and 32% increase in flexural strength and flexural modulus of CFRP/INT specimens respectively. Zanjani et al. also suggested that TEGO as an interface modifier enhances the interfacial bonding between the matrix and fibers; consequently, the load distribution becomes more efficient [44]. With the integration of TEGO on the surface of the reinforcing carbon fibers, the surface area of these fibers increase significantly, thereby the contact surfaces between the fibers and the matrix material are increased.

In the CFRP/MTX system, there is a distinguishable improvement in flexural strength compared to the neat composite. As seen in Figure 2.36, fracture occurred at higher stress-strain values for this arrangement among the other samples. It proves that the composite with TEGO-integrated matrix withstands higher loads. However, TEGO that is dispersed in high amounts in the matrix creates entanglements, which lower the mobility of the chain segments of the matrix [60- 67]. Additionally, mechanical interlocking originating from the increase

in the surface area is directly related to the mechanical enhancement observed in these specific type of samples [68, 69-72].

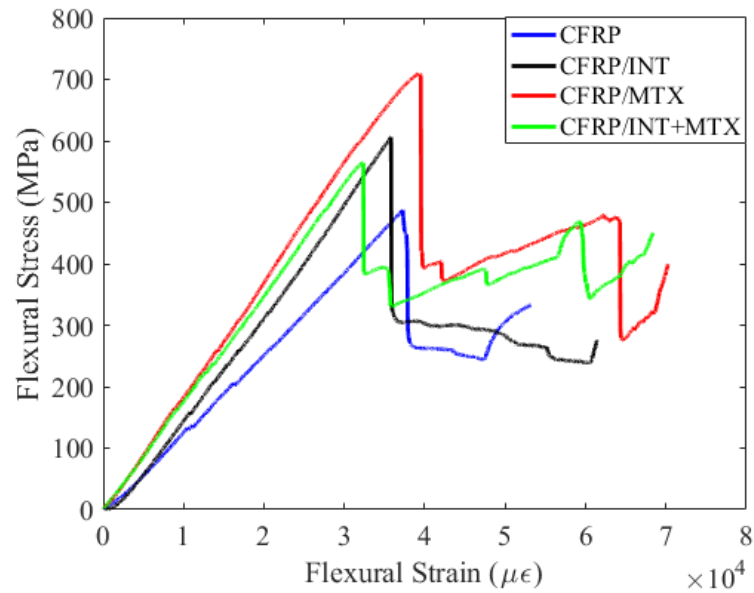


**Figure 2.36** Representative flexural stress - strain graph.

For the CFRP/INT+ MTX, there is a 26 % increase in the flexural modulus, which is close to the moduli of CFRP/INT and CFRP/MTX arrangements. Figure 2.36 shows that, nearly 18% improvement occurred in the flexural stress of CFRP/INT+MTX specimen with respect to the reference neat material. However, it can be stated that the crack formation in the hybrid sample started at lower strain values than the neat composite.

In addition to the flexural tests, the fractographic analysis of the three - point bending specimens were conducted to comprehensively investigate the failure mechanisms and these inspections were made with Nikon Eclipse LV 100ND optical microscope. After conducting three-point bending tests, to keep the specimen at the same damage state, a special apparatus was used to imitate the same bending load (Figure 2.37).



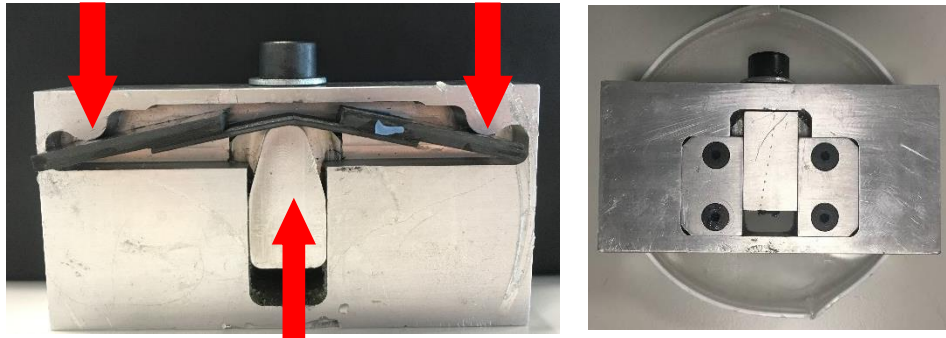


**Figure 2.37** Apparatus with the mounted specimen used to imitate the loading of 3-point bending test.

Following, the specimen held within the apparatus was immersed into the Biresin<sup>®</sup> CR120 epoxy and Biresin<sup>®</sup> CH 120-6 hardener system, which was cured at the room temperature. The resin material around the damaged region was trimmed to focus on the failure area. The surface of the mounted specimen was ground with 120, 360, 500 and 1000 grit sand papers respectively, with the Struers grinding machine. The aim of grinding with different grit number sandpapers was to obtain smooth surface finish on the specimen, as it is well known that the quality of the surface plays an important role while inspecting the specimen with optical microscope.

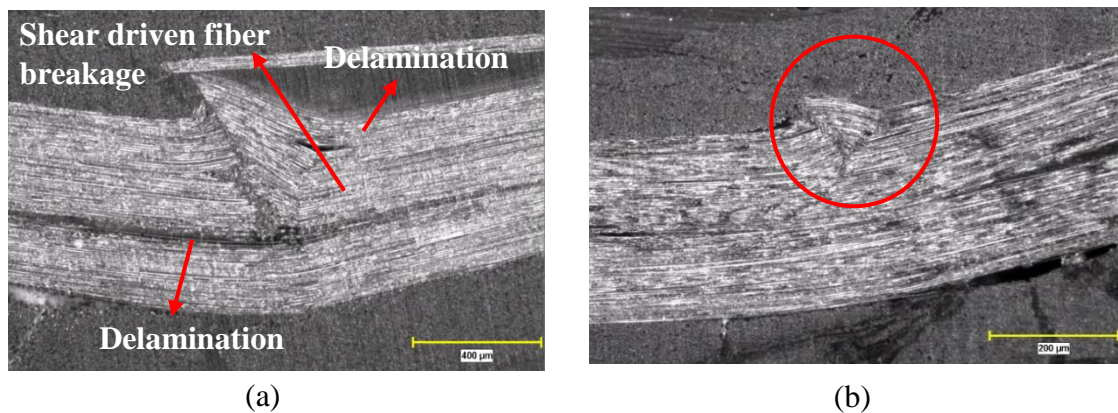


**Figure 2.38** Optical microscope images of the damaged (a) CFRP/INT, (b) CFRP/MTX specimens.

As shown in Figure 2.38 (a), shear-driven fiber breakage and interlaminar fracture (delamination) were the leading mechanisms of failure for CFRP/INT specimen subjected to three-point bending. Delamination is the common failure type among the composite

structure, triggering crack propagation; however, it dominates the failure especially under bending and compressive loads. For the CFRP/INT specimen, TEGO reinforcement only exists at the interface of the composite structure causing an increase in the flexural modulus value, however not as significant as in the CFRP/MTX case. It is worth restating here that the matrix nano-strengthening played an important role in the homogeneous dissipation of the fracture energy.

Examining Figure 2.38 (b), for the CFRP/MTX arrangement has the highest mechanical improvements with TEGO in its flexural properties as observed in the tensile, compressive and mode I fracture toughness energy tests. In these specimens, the shear-driven fiber breakage region remained very small, and the rest of the sample did not contain any substantial amount of delamination unlike the CFRP/INT and CFRP/INT+MTX specimens.

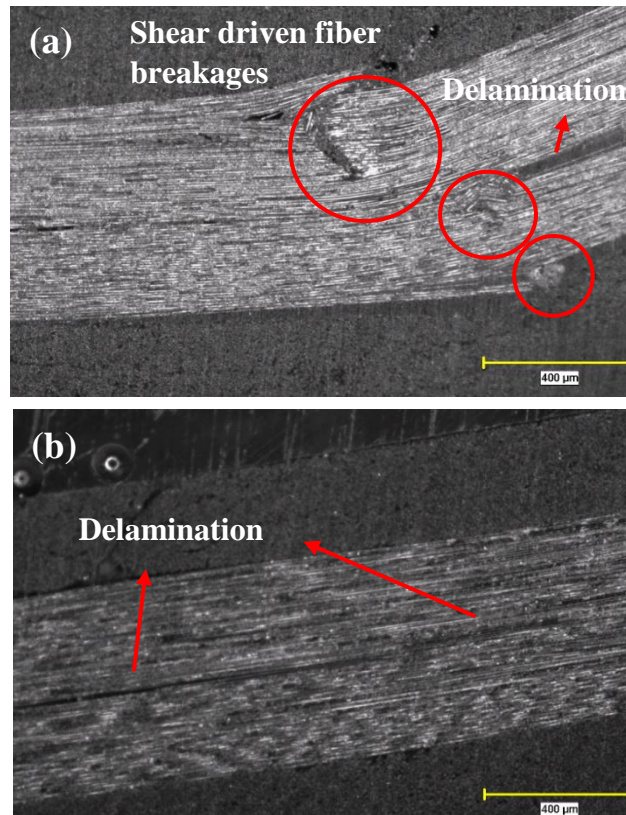


**Figure 2.39** Optical microscope image of the (a) CFRP/INT+MTX (b) Neat specimens.

The CFRP/INT+MTX specimen exhibits more than one shear-driven fiber breakage locations, which apparently caused a decrease in flexural strength compared to the other arrangements (Figure 2.39). Neat specimen exhibits the same failure types, including mainly delamination. This is the reason that the flexural strength values of both neat and CFRP/INT+MTX were nearly in the same trend. However, having interfacial nano reinforcement material in CFRP/INT+MTX, the flexural modulus still exceeded the value of the neat specimen.

To conclude the chapter, the comparison of percentage improvement of each mechanical test results are shown in figure 2.40. As seen in radar graph, the mechanical properties of each three modified system enhanced with respect to the reference neat system. The highest increases in flexural stress (FS), fracture toughness energy (FTE) and tensile stress (TS) were observed in CFRP/MTX system. Moreover, interface modified system followed the second highest trend in FTE, FS and FM values. The CFRP/INT+MTX system showed the highest improvement in compressive modulus (CM).

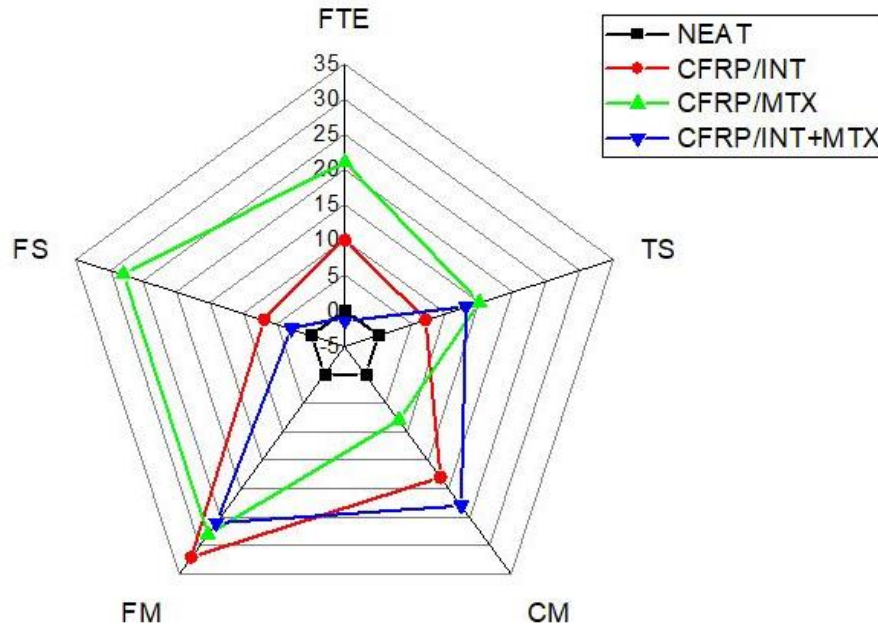


**Figure 2.40** The percentage improvement of mechanical properties of each system.



## Chapter 3

### Design of Multiple-Nozzle Electro spraying Unit

#### 3.1 Introduction

Studies in recent years have indicated that there are several methods for nano- and micro-scale deposition methods such as ink jetting [74], electro spraying, plasma spraying and photolithography [75]. Lord Rayleigh stated the logic behind the electro spraying method for the first time in 1882 [76], then the idea was improved by Zeleny [77] and Sir Taylor [78] in 1917 and 1964, respectively. Electro spraying is one of the accessible, low cost and user-friendly method that is currently in use in many fields such as biomedicine [79], nano-material integration, micro manufacturing [80] and sensors technology [81]. Electro spraying is a method that uses depositing solution-based nano or micro particles on the target surface. High voltage source is employed to atomize the solution to enable spraying in micro and nano-scales. To obtain fine droplets, liquid is forced to move through an electric field at high electrical potential environment [82]. When the droplet is within the range of the electric field, Coulomb forces are formed on the droplet due to the electric charge. Moreover, Coulomb forces cope with the cohesive forces within the droplet. When the Coulomb force exceeds the cohesive force, the droplet is immediately atomized in to a micro or nano-scale depending on the applied parameters [83]. To maintain the size of the droplets within a constant range, both flow rate and the voltage level are optimized. Moreover, the size and the direction of the droplets can be controlled with the electric field by administering their charge characteristics. The dripping of the droplet from the nozzle is calculated by the Rayleigh limit equation [82].

$$L_R = q(64\pi^2 \epsilon \gamma R^3) \quad (3.1)$$

$$q = 8\pi\sqrt{\epsilon_0 \gamma R^3} \quad (3.2)$$

$L_R$ : Rayleigh limit

$q$ : the surface charge of the droplet

$\epsilon$ : the permittivity of the surrounding medium

$\gamma$ : the surface tension of the liquid

$R$ : the radius of the droplet

Monodisperse atomized droplets are generated by using the appropriate parameters in these two equations. The distance between the electrically conductive metal nozzle and the targeted fiber surface plays an important role in the deposition area due to the instable movement of the charged particles [84]. When the nozzle and the targeted material are positioned very close to each other, a stable jet is observed. Achieving such remarkable enhancements in the small-scale integration of TEGO in composite specimens created a turning point to design and manufacture a large-scale fully automated electrospaying system with multiple nozzles for the future industrial applications.

## 3.2 Experimental

### 3.2.1 Equipments

Poysan Makina B100150 CNC Router, New Era NE -300 Just Infusion<sup>®</sup> one channel and NE-1600 programmable six channel syringe pump, 6 units of Festo Y- fittings were the main components of first design of the electrospaying system. 1 unit of 500x250x15 mm and 2 units of 250x230x20 mm pre-ground aluminum plates; with 70 x 60x 110 mm PTFE Teflon were processed in Sabanci University Production Research Laboratory to manufacture the pump stand and needle holders. For the second design Kestamid<sup>®</sup> and fiber plates were used due to their non-conductive properties for providing safety during usage. 45 x 90 Aluminum sigma profile, Hamilton Injections N718 NDL 6/PK (18/2"/3) and three zones Brisk Heat<sup>®</sup> Silicone Rubber heating Blanket (SR style) of size 125 cm x 176 cm with three built-in "J" style thermocouples and 240 VAC, 15 amps per zone, operating range 32-1400°F (0-760°C) MPC223NRN three zone thermocouple PID controllers were used. Heat blankets were placed between 125 x 126 x 8 mm tempered glass plates. 1250 x 1790 mm sized Aluminum plate was used for the grounding of the electrospay unit.

### 3.2.2 Working Principle of the Electro spraying Unit

In the electro spraying process, to maintain a fine layer of deposition on the surface, the dispersion to be sprayed should be sonicated well just before the spraying process. Firstly, syringes are loaded with the solution and parameters such as flow rate and the diameter of the syringe are set digitally in the pump system. Hamilton metal needles are fixed at the tip of the syringes. The height of the pump from the surface is changed between 15 to 20 cm with respect to the applied high voltage, considering the applied voltage level is directly proportional with the distance between the ground and the spraying needle. In this case, applied voltage is usually preferred between 15 to 20 kV. Applied voltage, flow rate, needle diameter, the distance between the ground and the needle basically influence the particle size and distribution [83].

### 3.2.3 Design of the Multiple Nozzle Electro spray Unit

The multiple nozzle electro spraying unit was designed for adopting the same process that was briefly explained in the previous chapter to the pilot scale production. As seen in Figure 3.1, the design of the unit was primarily completed in SolidWorks. Within the scope of the 2+2 TÜBİTAK project (nr. B100150), CNC Router's milling spindle was removed from the router head and a single channel of three New Era NE -300 Just Infusion<sup>®</sup> pumps were placed on the designed stand.

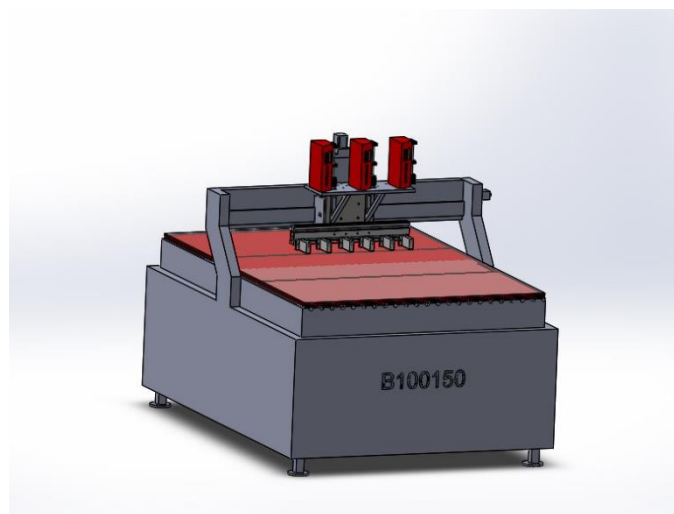


*Figure 3.1* The design of Multiple-nozzle electro spray unit in SolidWorks software.

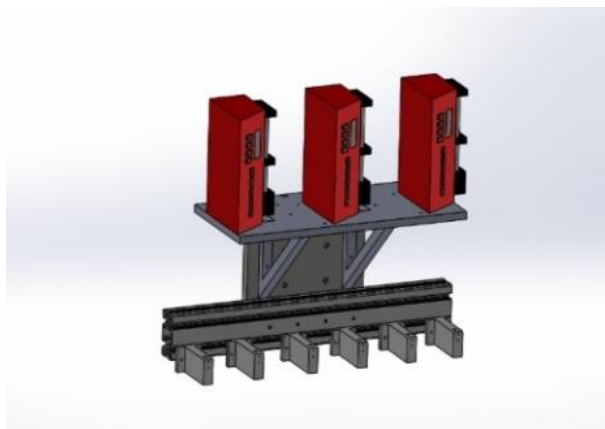


**Figure 3.2** The pump stand.

As shown in the Figure 3.2, three NE-300 single-channel pumps were located on top of an aluminum plate side by side to minimize the surface area and so the weight of the aluminum plate. Feder's were used for supporting the plate against possible bending forces. 45 cm x 90 cm sized Aluminum sigma profile was used as the rail structure to hang the custom-designed Teflon apparatus shown in Figure 3.3, to be used for attaching the metal needles. Due to non-conductive characteristic of Teflon, metal pins are embedded in the designed apparatus. Each pump includes one syringe, and in total three syringes separated into six needles by a tubing system. The division of the tubing system was fitted with polypropylene T- joints. However, leakage was observed due to the non-matching dimensions of both T- joints and tubing system. Then, Festo Y- fittings were replaced with a lock system to prevent leakage during spraying process. To evaporate the DMF/nano-material solution, Brisk Heat<sup>®</sup> Silicone Rubber heating blankets were located in between tempered glass plates on the base surface of the unit.

In spite of many trials, a stable spraying profile could not be obtained in the piping system, since aspirator pumping occurred in one of the pipes and disturbed the flow regime. For this reason, no synchronized sprays could be performed through all six needles.



**Figure 3.3** Completed assembly of the pump stand.

Another problem was the high voltage that jumped over the metal pump stand into the chassis of the router (as the circuit was grounded), which was a safety issue and a damaging event for the electrical and metallic components. After this event, the drivers and the Ethernet card of the CNC Router became out of order and had to be renewed. For this reason, the grounding in the system was disabled and other solutions were sought. Eventually, the pump stand was re-designed and manufactured with non-conductive material Kestamid<sup>®</sup>. The parts that are in contact with the metal chassis were isolated by a special kind of wood-fiber material (Figure 3.4). The orange colored part seen in the design and the sides of the router are covered with rubber to prevent any electrical contact (Figure 2.5).

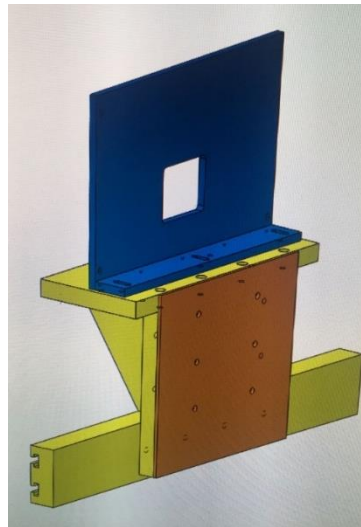


**Figure 3.4** New design for six-channel pump stand from Kestamid and fiber material in SolidWorks.

The pump model was modified to solve the flow problem of the DMF/TEGO solution that encountered in the previous attempts of electrospraying. Instead of separating three pumps into six needles, the design was updated so that a direct connection can be established from the six channel New Era-1600 pump to needles (Figure 3.5). However, during spraying, it was noticed that the TEGO agglomerated in the tubes and only DMF was sprayed. Parameters such as the spray flow, voltage and the distance between the pump and the metal surface were optimized accordingly to fix this problem.

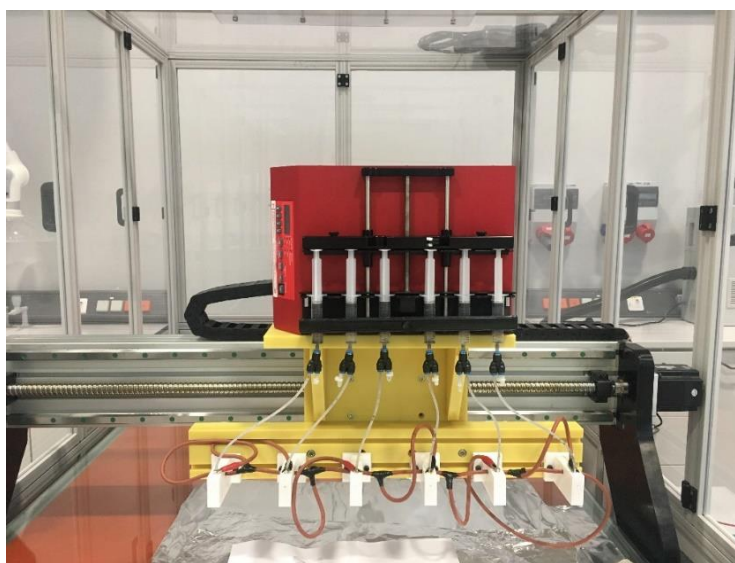


**Figure 3.5** New design for six channel pump stand from Kestamid and fiber material.

During the six-channel pump electrospraying trials, a sudden potential drop in the electric field was observed before DMF and TEGO solution reached the metal needle tip. Although high voltage was applied at the tips of the needles which were located on the Teflon component, the flow started from the tip of the syringe and followed the polypropylene tubes until it reaches to the metal needles. Therefore, deformed TEGO nano-particles began to form clusters and remained in polypropylene tubing system, while only DMF was sprayed onto the surface. The accumulated TEGO clusters can only be sprayed onto the surface abruptly and randomly whenever they could be able to exit the tubes. In order to eliminate this problem, the polypropylene pipes with interconnection elements were all removed and the desired sprinkling profile was obtained by connecting the high voltage crocodile directly on the middle height of the metal needles. However, inserting six needles into the pump while

applying high voltage created a new problem. As shown in Figure 3.6, the magnetic field of each needle effected each another due to the short distance between the needles. Specifically, the position of the crocodiles on the needles that transmit high voltage plays an important role in the spraying profile.



**Figure 3.6** Electro spray profiles with six needles.

The solution for this problem was inserting only three needles instead of six needles by leaving a specific distance between them (Figure 3.8). After many trial and errors, the minimum distance between the needles were specified equal in number to the voltage value that applied. For instance, when 15 kV applied to the metal needles, the distance between the ground and horizontal distance to other needles should be 15 mm. With the three-needle arrangement, the desired result was obtained. The router motion was specified by setting 10 mm distance movement along the y-axis to obtain the profile that shown in Figure 3.7.

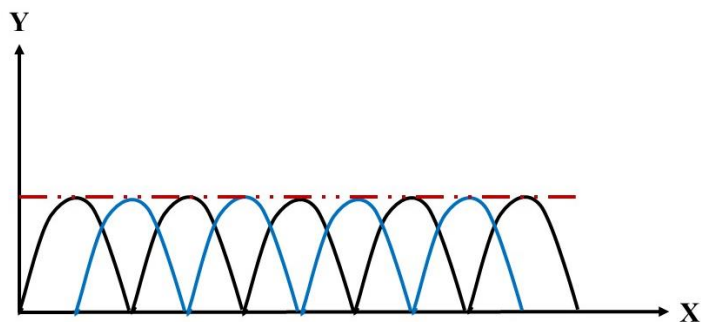


**Figure 3.7** Homogeneous spraying profile.



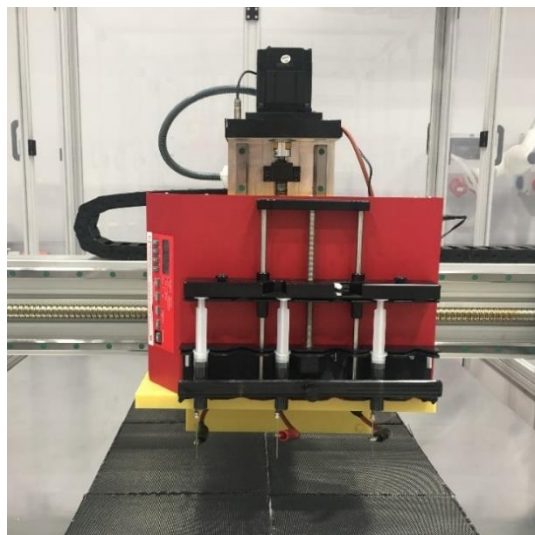


**Figure 3.8** Final design of the pump stand with the syringes mounted.

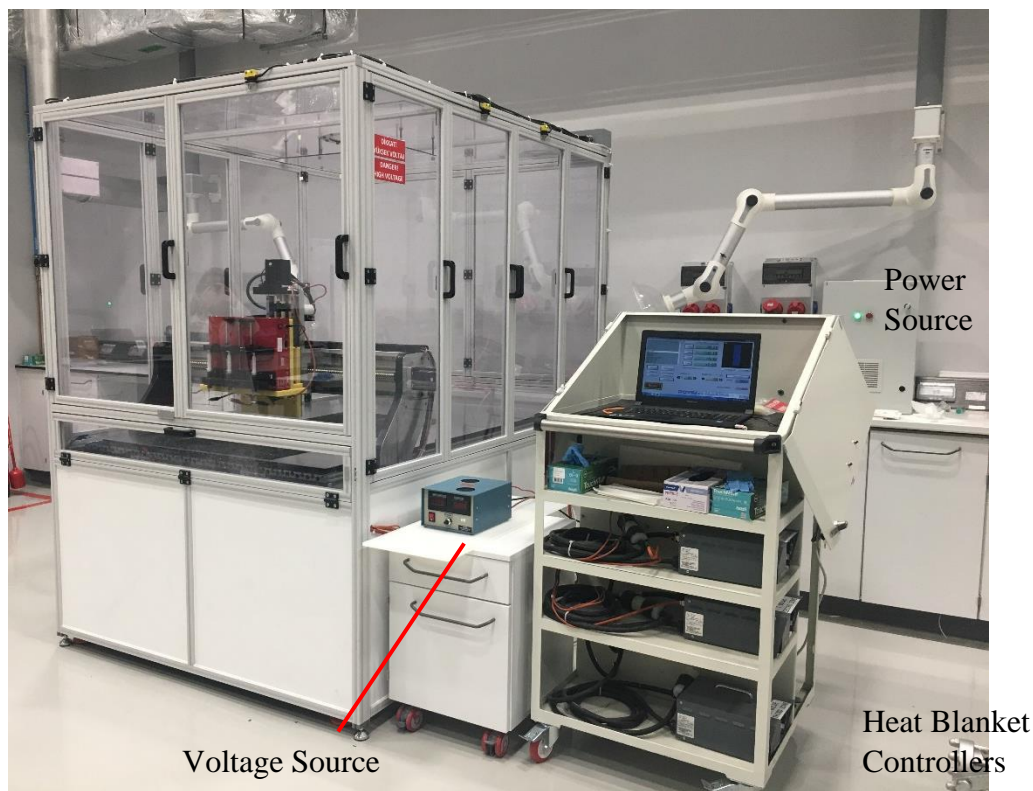


**Figure 3.9** Automated electrospinning unit with the computer system and heat blanket controllers.



Figure 3.9 shows the complete system of the electrospaying unit, currently in use at the composite technologies center of excellence. The unit is controlled by a computer, in which a modified software can be used for changing the spraying parameters, the position of the injection head, etc. The movement of the electrospaying head is provided by G code. G code is adjustable for the size of the fabric that is to be coated. To prevent any damage on the injecting head due to hitting the surrounding panels the position of the head should be reset in the software before any spraying attempt. The code can be written, or existing codes can be edited by the user, and uploaded to the computer for the software to read it and execute accordingly.

The execution (so the spraying) can be paused to refill the injectors with the TEGO/DMF (or other chemical mixture of nano particles and a suitable solvent), so the unit does not start spraying from the beginning when the injectors are refilled and mounted on the spraying head.

The panels surrounding the unit are connected to a control unit, so that the voltage is turned off for safety whenever any panel is opened by the operator. Additionally, the current level should be watched closely during the spraying operation and the unit should be stopped in case of a high current value is shown on the voltage unit's screen.

To conclude, the new electrospaying system provides spraying facilities for large amount of fibers in a quicker way. As a future work, a drum will be integrated into the electrospaying system, to enable spraying whole roll of fibers with maximum 1250 mm width, so that this facility will directly integrate into the production line. The electrospaying unit will be a milestone for leading the composite industry towards nano material coating. Time efficiency, low cost, flexibility in using provide the principal advantages of the electrospaying system compared to the lab scale ones.

# Chapter 4

## Repair of Carbon Fiber Monolithic Plates

### 4.1 Introduction

Repairing of the damaged components is one of the crucial steps to extend the life cycle of advanced composite materials that are used in the aircraft structures and wind turbine blades. Compared to metal components, fiber reinforced polymer composites are very lightweight, have high stiffness, strength and especially corrosion resistance [85, 86], making them ideal candidates for the mentioned fields of applications. However, one of the main disadvantages of composites is their high costs of production with respect to the metal structures. The replacement of damaged composite structures in aerospace applications with the new ones is not economical, as the constituent materials and their processing techniques are expensive. Therefore, for the sake of reducing the cost, repair methods were developed as an alternative to replacement of damaged composites. To maintain the high strength and aerodynamic properties of the component after the repair process, bonded repair is usually preferred. This method mainly consists of removal of the damaged region by special techniques and adhering a correspondingly cut and shaped new material which has the same constituents and properties into the damaged site. The most common repairing methods for composite structures can be listed as stepped and tapered sanding, both of which are branches of the bonded scarf repairs [87]. Scarf angles, type of patches and adhesives are the critical parameters that affect the final quality of the repaired structure [88].

In this chapter, repairing procedures for monolithic composite plates are investigated. The repair procedures were planned in accordance with the Turkish Technic's (in connection with Turkish Airlines) repairing guidance. The aim of the present work was to examine the mechanical properties of the structures that were repaired by nano-material integrated patches. Moreover, the difference in the mechanical properties of the resulting composites repaired by stepped and tapered sanding methods was investigated. All procedures from the

production stage of the composite plates to the repair process are covered in this section. Each step for the repair methods are discussed. Shear tests of the repaired plates were successfully completed, and satisfactory results were obtained.

## **4.2 Experimental**

### **4.2.1 Materials**

Similar to the small-scale integration of nano-material in the different phases of composites (previous section), the same nano material, thermally exfoliated graphene oxide (TEGO) Grade-2, N, N dimethyl formamide (DMF, Sigma Aldrich, 99%) was used to prepare the TEGO solution for electrospaying on the fibers and integration into the resin system. BMS9-8 3K-70-PW, 7 mil plain weave carbon fiber prepreg was purchased from KordSA for the composite plate production. The fiber density of the prepreg is  $1800 \text{ kg/m}^3$ . MY 721-epoxy resin, B (hardener) and C (accelerator) was used as epoxy system. Due to the commercial confidentiality, hardener and accelerator were named as B and C, respectively. 3M Scotch-Weld™ AF 163-2 Structural Adhesive Film was used during repair process. Methyl Ethyl Ketone (MEK) was used to clean the tapered surface during repairing.

### **4.2.2 Characterization**

Mechanical tests were conducted with INSTRON 5982 100 kN Universal Test Machine (UTM) using a cross-head speed of 1 mm/min and 2 mm/min for shear tests, respectively. All mechanical tests were performed in accordance with the ASTM standards. The axial and transverse strain data were measured by Micro Measurements C2A-06-250LT-350, C2A-06-062LV-350, biaxial and shear strain gages, respectively. Additionally, the fracture surfaces of the damaged plates were examined with Nikon Eclipse LV 100ND optical microscope after the mechanical tests.

### **4.2.3 Preparation of Graphene Integrated Epoxy Resin**

Regarding the integration of the nanoparticles to the system, thermally exfoliated graphene oxide (TEGO) of 0.05% by weight was added to the epoxy resin to improve the mechanical properties. First, MY 721-epoxy resin, B (hardener) and C (accelerator) were prepared by 100/16/5 ratio, and were mixed at 1000 rpm for two minutes using a Thinky ARV -310 planetary vacuum mixer to obtain reference or neat epoxy samples. Detailed

chemical information on the content of hardener B and accelerator C materials could not be exposed here, as they are commercially confidential. The test specimens are prepared by pouring MY721-B-C mixture into an Aluminum mold (Figure 4.1) and then cured in the Pol-eko Aparatura oven. Cure cycle includes keeping the molds in the oven for 2 hours at 100 ° C, then 2 hours at 150 ° C and finally 2 hours at 220 °C. Test samples were demolded after slowly cooling them to the room temperature in the oven (Figure 4.2).

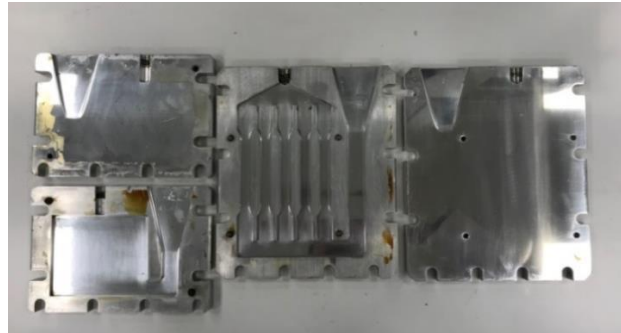


**Figure 4.1** Aluminum molds used in the production of test specimens.

For the preparation of TEGO-reinforced epoxy samples, TEGO is added into MY-721 epoxy resin with the amount of 0.05% by weight of MY721-B-C mixture. The TEGO-MY-721 epoxy resin mixture is processed for 30 minutes utilizing Ross HSM-705 high shear mixer (HSM) at different speeds to investigate the effect of the speed of rotation on the dispersion, namely, 5000, 10000 and 12000 rpm. After high speed shear mixing, components B and C were added to the MY721-TEGO dispersion by 100/16/5 ratio and then mixed with the Thinky device for 2 minutes at a rate of 1000 rpm. After casting the mixture in the molds, curing was carried out following the same cure cycle previously introduced. The reference epoxy and the graphene-reinforced epoxy test specimens are shown in Figure 4.2.



**Figure 4.2** The prepared (a) reference and (b) TEGO reinforced tensile test specimens.

#### 4.2.4 Preparation of Mechanical Test Specimens

The reference epoxy samples were subjected to tensile and three-point bending tests according to ISO-527 and ASTM D790 standards, respectively (Figure 4.3). The crosshead speed was 2 mm / min, and strain values were logged by an Instron uniaxial clip on extensometer with 50 mm gage length and 25 mm travel distance. Bending tests were carried out at 1 mm / min cross head speed and specimens prepared at a (L/h) ratio of 16. All tests were performed at least 5 times by using all the specimens that were produced in laboratory conditions to verify the results.

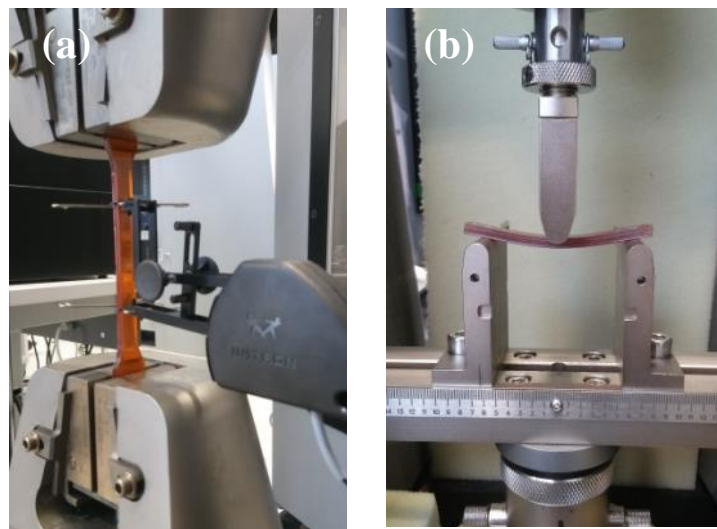


**Figure 4.3** The reference test samples (a) during tensile test and (b) three point bending test.

### 4.2.5 Mechanical Test Results of TEGO-Integrated Resin

The tensile and flexural mechanical properties measured with the tests were compared with the reference samples. Figure 4.4 and Figure 4.5 show the stress-strain curves obtained for the specimens under tensile and flexural loads, respectively. As can be seen, the stress-strain curves exhibit linear behavior and damage occurs when the maximum damage load (stress) was reached.

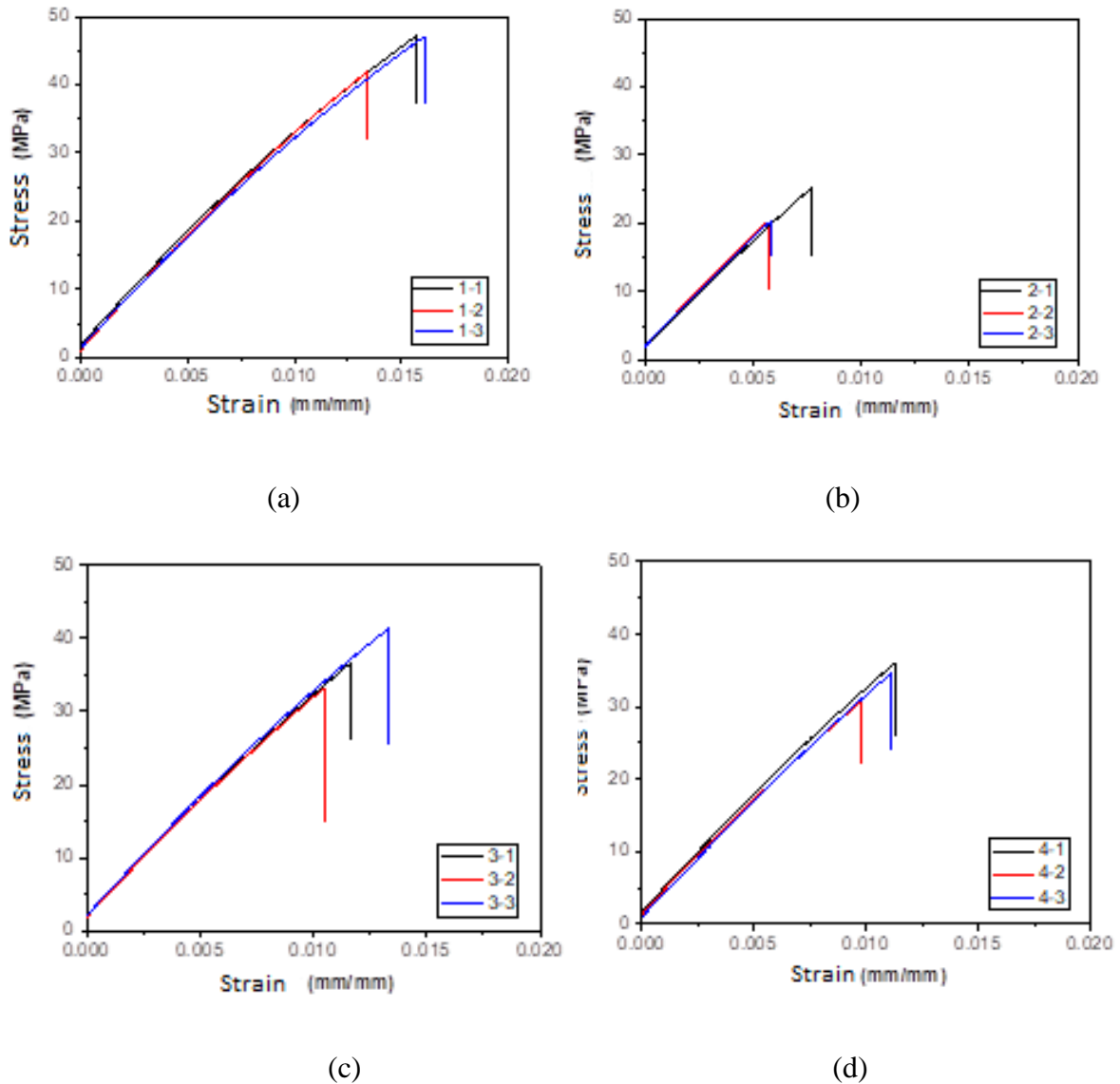


**Figure 4.4** The tensile stress-strain curves (a) reference state, after the stirring of the tensile test specimens at (b) 5000 rpm, (c) 10000 rpm and (d) 12000 rpm.

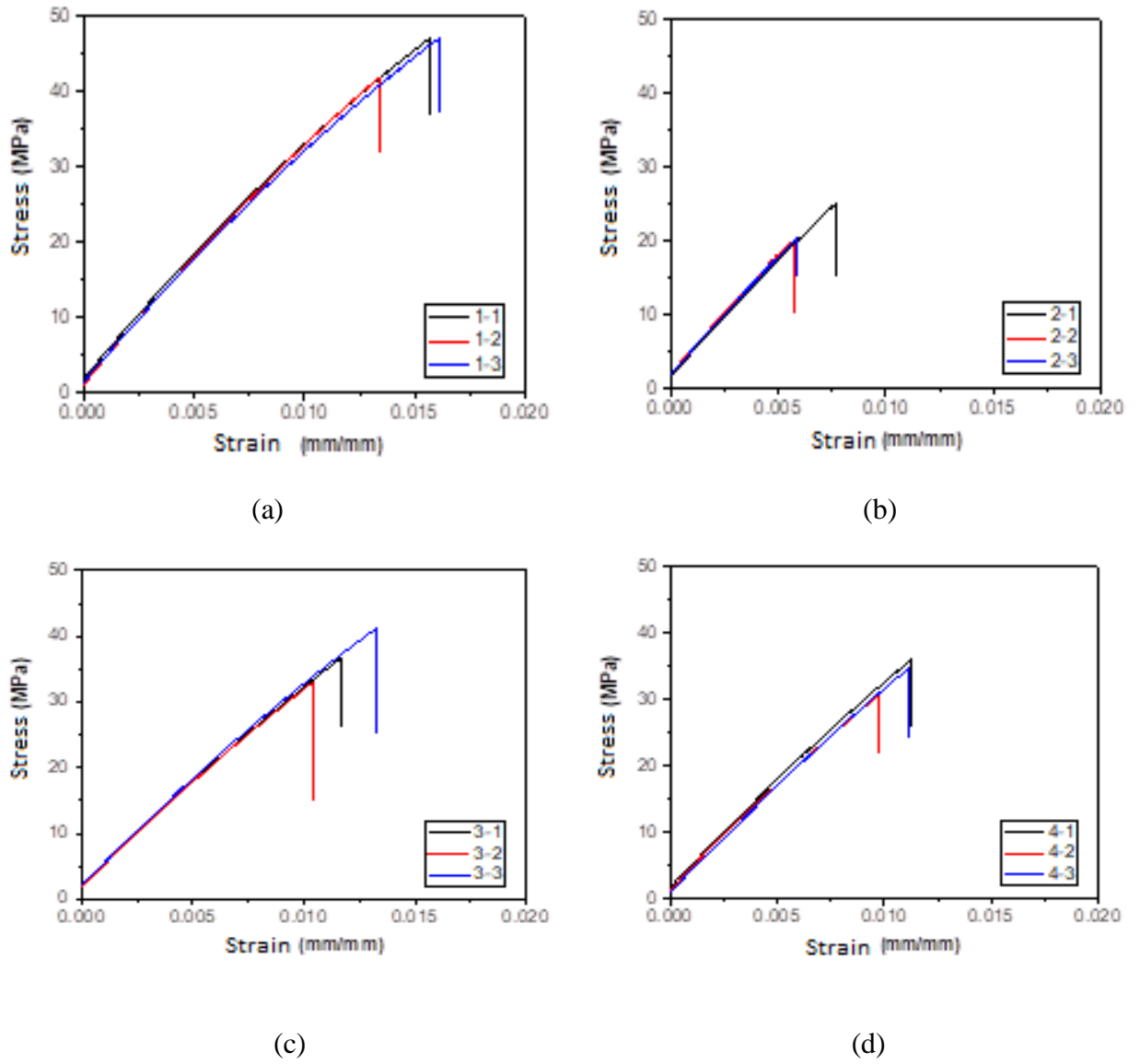


**Figure 4.5** The flexural stress-strain curves obtained (a) reference sample, after mixing at high speed of (b) 5000 rpm, (c) 10000 rpm and (d) 12000 rpm of high-shear mixing.

**Table 4.1** Tensile and three- point bending test results.

<b>Sample</b>	<b>Elastic Modulus (MPa)</b>	<b>Tensile Strength (MPa)</b>	<b>Flexural Modulus (MPa)</b>	<b>Flexural Strength (MPa)</b>
<b>Reference MY721BC</b>	3468	40	3430	109
<b>MY721-BC-0.05 Graphene-5000 rpm</b>	3297	22	3290	55
<b>MY721-BC-0.05 Graphene-10000 rpm</b>	3303	39	3420	63
<b>MY721-BC-0.05 Graphene-12000 rpm</b>	3400	33	3340	80

The results obtained from the tensile and three-point bending tests are given in Table 4.1. Compared to the reference samples, it was observed that the damage occurred earlier in the graphene reinforced specimens, as can be implied from the lower tensile and flexural strengths. The elastic modulus and tensile strength values of the reference epoxy material are evaluated as 3468 MPa and 40.6 MPa, while the reference flexural modulus and strength values are 3430 MPa and 109.2 MPa, respectively. Comparing the neat sample's properties with the nano-reinforced specimens, a decrease in the elastic modulus and tensile strength values occur with the TEGO-integration. This decrease percentages are 4.9% and 4.7% at 5000 rpm and 10000 rpm of high shear mixing cases. After graphene addition, the flexural strength values decreased by 49%, 41% and 26% for the mixing rates of 5000, 10000 and 12000 rpm. No significant change in the elastic and flexural moduli is seen for the case of 12000 rpm mixing rate. Tensile strength values exhibit significant drops, except for the samples which were mixed at 10000 rpm. The main reason for this decrease in mechanical properties is that graphene was not uniformly distributed in the epoxy and agglomerated graphene clusters cause stress concentrations in the structure. To solve this problem, studies in the literature have been reviewed and the method for the uniform dispersion of graphene in epoxy resin has been developed, as described below.

To ensure homogeneous dispersion of the graphene in epoxy, TEGO was first mixed with tetrahydrofuran (THF) in the bath sonication for 2 hours. Then the TEGO/THF solution was dispersed for 1 hour with probe sonication. The TEGO/THF uniform solution was exposed to bath sonication for 2 more hours by adding MY721 epoxy resin after probe sonication. The resulting MY721/TEGO/THF solution was kept in the oven at 70 ° C for 48 hours to



vaporize the THF chemical from the system. The solution was then examined under optical microscope and homogeneous distribution of the graphene in epoxy was observed (Figure 4.6).

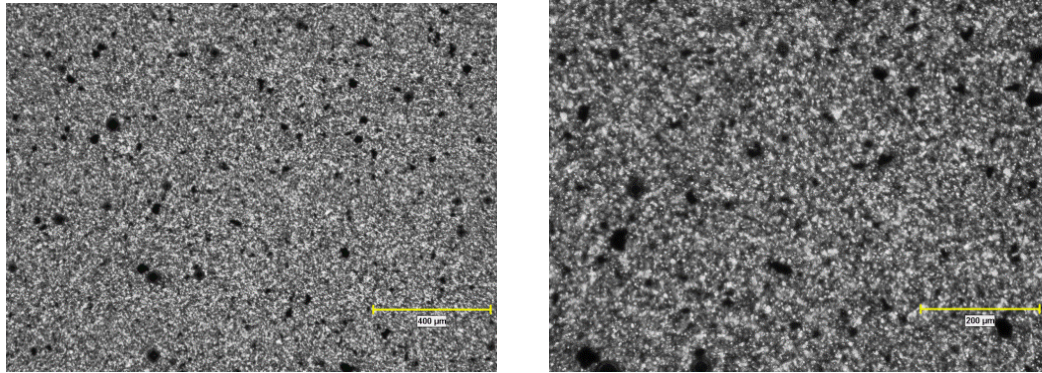


**Figure 4.6** Homogeneous distribution of graphene in epoxy.

The %0.05 wt. TEGO integrated resin was used for manufacturing the prepregs on Hotmelt system in KordSA pilot scale manufacturing line for producing the repair patches.

TEGO-integrated prepregs were also manufactured applying the TEGO integration only on the reinforcing carbon fibers with the electro spraying unit described in Chapter 3. The dry fiber preforms as mentioned in the previous chapter were electro sprayed with %0.01 wt. TEGO. For the nano-integrated patch production, the surface of the woven fiber was coated with TEGO five times in the electro spray unit, leading to %0.05 wt. TEGO in the fiber preform. Again, 125 mm x 120 mm TEGO coated woven carbon fiber was covered with neat resin film for the preprep manufacturing in KordSA Siltex production line.

#### **4.2.6 Manufacturing of the Carbon Fiber Reinforced Composite Plates**

The repair process should be performed with the same material of the main body. Additionally, fiber orientation should be identical with that of the damaged structure. Polymer matrix prepregs were produced by using the newly developed TEGO integrated resin system, neat resin system and TEGO integrated carbon fiber woven fabric with the properties given in Table 4.2. In this study, the woven carbon fiber was produced by KordSA to produce an equivalent fabric material as CYTEC 3K-70-PW, TY4, CL2- Graphite prepreg 350 Degree. For later reference, prepregs without any TEGO integration, and with TEGO integration into the fiber or resin are referred to as “n-prepreg” (i.e. neat), “f-prepreg” (nano-integrated fiber), and “m-prepreg” (nano-integrated matrix) systems. CFRP plates were

produced based on the fabrics and orientations used by Turkish Technic in the framework of Boeing aircraft repair standards. Composite structure was decided as eight plies with prepreg 3K-70-PW CF fabric and the fiber orientation is shown schematically in Figure 4.7.

**Table 4.2** Properties of the carbon fiber prepreg and epoxy.

<b>Type IV</b>	Nominal resin content 40 percent by weight
<b>Class</b>	Woven fabric prepreg
<b>Style – Class 2 (BMS9-8)</b>	Style 3K-70-PW, Type IV, 3K yarn, 7 mil plain weave, nonporous, 0,0083 inch nominal cured ply thickness
<b>Fabric Details</b>	
Fabric weight	Dry: 197 g / m <sup>2</sup>
<b>Type of Yarns</b>	
Warp yarn	3K Carbon
Fill yarn	3K Carbon
Fiber	300T
<b>Resin Details</b>	Similar design with 350F Autoclave cure ready Cycom 984 epoxy adhesive

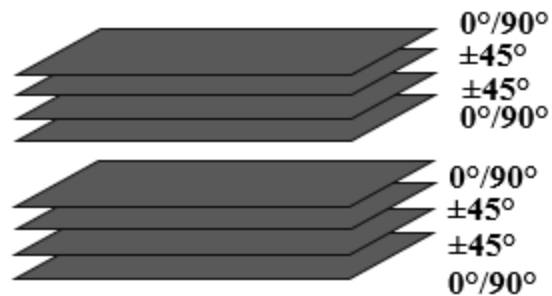


**Figure 4.7** Stacking sequence of the prepregs.

Prepregs were cut with Zünd® G3 L-3200 Cutter into dimensions of 25x25 cm in 0°/90° and ±45° fiber orientations. The surface preparation of the metal plates on which the composites would be produced was completed with applying two coats of XTEND AMS Semi- Permanent Mold Sealer and left to dry approximately for 20 minutes between each coating process. Then, prepregs were laid symmetrically to prevent any possible buckling following the curing process of the composite plates. Carbon fiber prepregs were stacked on the metal plate according to the predefined orientation and framed by rubber tapes to avoid resin overflow during curing (Figure 4.8). Recommended cure cycle for the developed resin

material is one hour at 135°C, under 7 bar pressure. MSE Press Series-Hot Press was used for manufacturing of the 25 x25 cm CFRP plates (Figure 4.9). The heat cycle of the hot press starts with warming up from room temperature to the desired temperature in 10 minutes. After reaching the desired temperature, prepregs with the metal plates were placed into the hot press and the pressure was set into 4.5 tons. After curing the thickness of the plate was 1.7 mm.

$$P = F/A \quad (4.1)$$

$$7 \text{ bars} = 700.000 \text{ N/m}^2$$

$$\text{Area} = 0,0625 \text{ m}^2$$

$$F = 43,750 \text{ N}$$

$$F = m \cdot g \quad (4.2)$$

$$m = 4,46 \text{ tons}$$

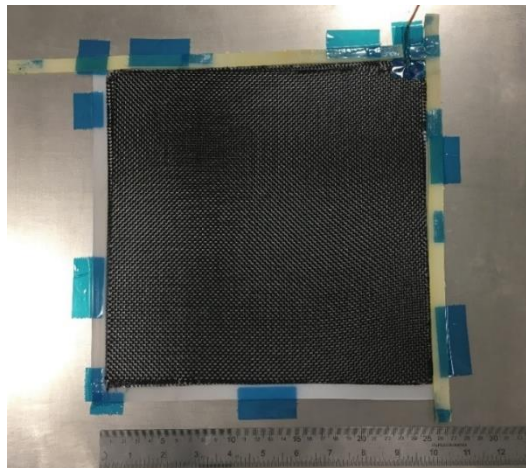


**Figure 4.8** 25 cm x 25 cm CFRC plate.



*Figure 4.9* Hot press.

### **4.3 Repair of the composite plates**

Repair of composites is an important concept in the aerospace, automotive and renewable energy industries. The repair method generally varies with the type of the damage in the composite, also depends on the type of composite material itself. There are several types of damages, such as holes, punctures due to low or high velocity impact of small or mid-sized objects (rain or birds), delamination, disbonds, core damage, resin damage, damage due to lightning, fire and thermal loads [88].

Damage detection is the primarily important step for repairing. In metal structures, damage is visible in the form of dents or dings. However, in composite structures, it is hard to detect damages with naked eye. Detectability of the visible damage depend on the impact energy. Damages that occur with high impact energy has stringent results. On the other hand, invisible damages between plies in general are only detectable with the non-destructive inspection methods [90]. The damage occurred inside the component might be delamination, debonding or both of them simultaneously.

The type and the orientation of the fibers, prepregs and the cure cycle of the resin of the damaged composite part should be defined clearly before starting the repair process. Tapered and stepped sanding methods are commonly used in aviation industry for repairing composites to prepare the damaged area for repairing. Tapered sanding is an angled sanding method that provides a smooth transition between the nondamaged and damaged area in the

structure, to maintain the uniform load transfer in the bonded repair. On the other hand, stepped sanding method is an alternative method, which removes the precise area from the damaged surface with sharp edges which creates stress concentration areas. These two methods are separated from each other with respect to the damage location and through the structural repair manual (SRM) documents of the aircraft companies.

The first action for repair generally starts with the surface inspection to determine the size and type of the damage. If the thickness of the composite part is less than 1.6 mm then tap test can employed for the damage inspection. For thicker composite parts, ultrasonic inspection is necessary. The thickness of composite plates were varied between 1.4 – 1.5 mm. The dimensions of the damaged site are marked on the composite structure to plan the repair process. With the guidance of Turkish Technic, the damage type is decided as full skin perforation with 25 mm diameter, meaning that totally eight layers of the composite should be repaired in our study. The taper ratio defines the overlap angle between plies, is decided according to the material type, grade of the fibers and the number of damaged plies, and is verified with the number of damaged plies. The 50:1 taper ratio should be preferred if the number of damaged plies is 5 or less, whereas 30:1 taper ratio should be used when the number of damaged plies is 6 or more (Figure 4.10). For this study, the surface preparation was completed with 30:1 taper ratio. To obtain a smooth gradation between the plies a finish removal was performed.

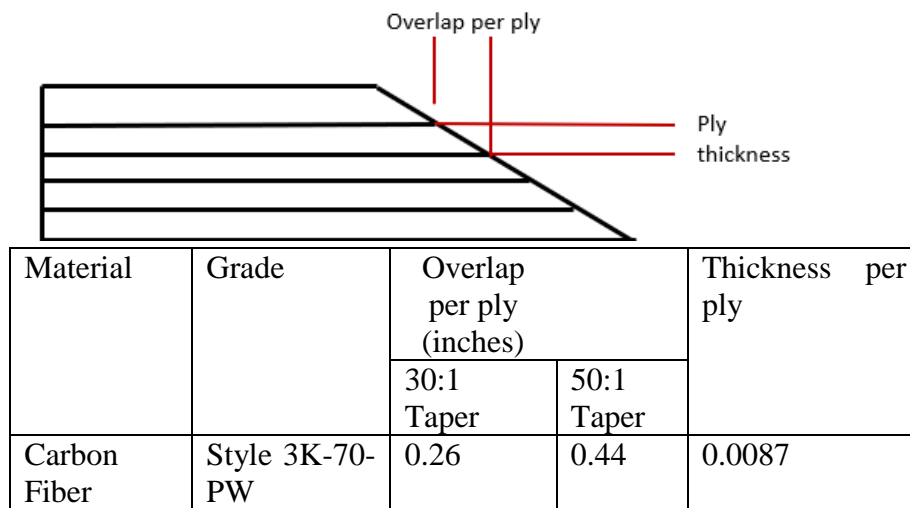


**Figure 4.10** Taper ratios.

The second step is marking the outlines for the sanding process by metal stencils as shown in Figure 4.11.



**Figure 4.11** Metal stencils for marking the outlines for sanding process.

Tapered and stepped sanding methods were applied to the damaged composite plates to compare the differences in their shear and tensile properties. According to the mechanical test results of the neat repaired components which will be discussed in the next section in detail, taper sanding method (Figures 4.12 and 4.13) was selected as a better option for repairing, so that method was employed in the rest of the components. After completing the sanding process, the surface area is cleaned with Methyl Ethyl Ketone (MEK) until it removes all carbon dust from the surface.



**Figure 4.12** Taper sanding method.



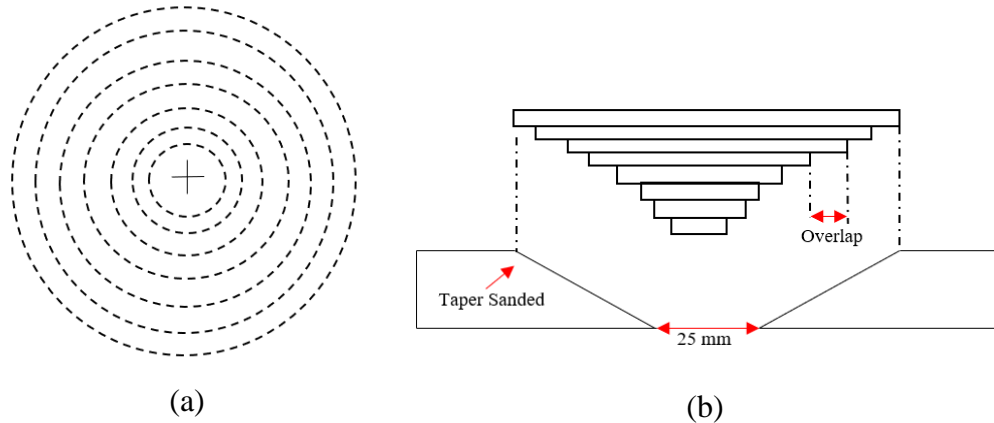


**Figure 4.13** Taper sanding method (a) top view (b) cross section views.

On the other hand, ‘water break’ test was performed to the repair-sanded surface to check if the surface was grease free. In this test, a thin layer of distilled water is applied with a fabric on the surface as seen in Figure 4.14. If the surface is rough and clean enough, the distilled water should stay on the surface at least 30 seconds without forming any water drops or beads. If water drops or beads form in 30 seconds, the sanding process should be repeated. Performing this test requires extra care as the composite structures can easily absorb fluids before or during service. It is worth noting that the remaining fluid or water inside the composite structure after the repair process can cause debonding due to the steam pressure that is formed during curing. For this reason, the plates were dried with heat blanket at 85 °C for 12 hours after the water break test.



**Figure 4.14** Water break test.

As seen from Figure 4.15, the repair-ply boundaries were marked by silver pencil to define the shape of each ply. It is vital to indicate the direction of the drawing and the orientation of each ply. Because the plies that used for repaired region have no perfect circular shape. A plastic film (miler) was attached to the repair surface to extract the template of ply boundaries. Edges of the plate and plastic film were labelled to avoid any confusion in the stacking sequence.

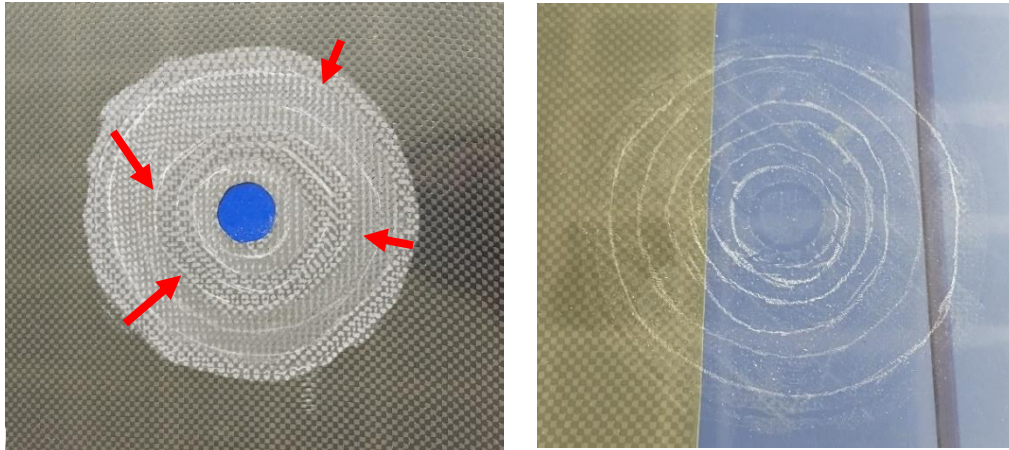


**Figure 4.15** Ply boundaries marked by silver pencil on the damage site of the composite plate.

In the next step, to prepare a template for ply cutting, the previously drawn ply boundaries were transferred back onto the parting film. Then, the template was placed on one side of the neat and TEGO-integrated prepregs. The repair plies and adhesive film were cut with respect to the cutting ply template (Figure 4.16). 3M Scotch-Weld™ AF 163-2 structural adhesive film was laid on the repair area and all the cut repair-plyes were stacked according to their orientations and shape of the template. To increase the stiffness of the repaired part two extra plies were used of the same material and orientation with the outer ply. It was important to make sure that no parting film were left in the damage site while placing the repair-plyes. Therefore, all parting films should be counted for verification after the process is completed. Lastly, the damage part was filled with the same prepreg with the help of the adhesive film.



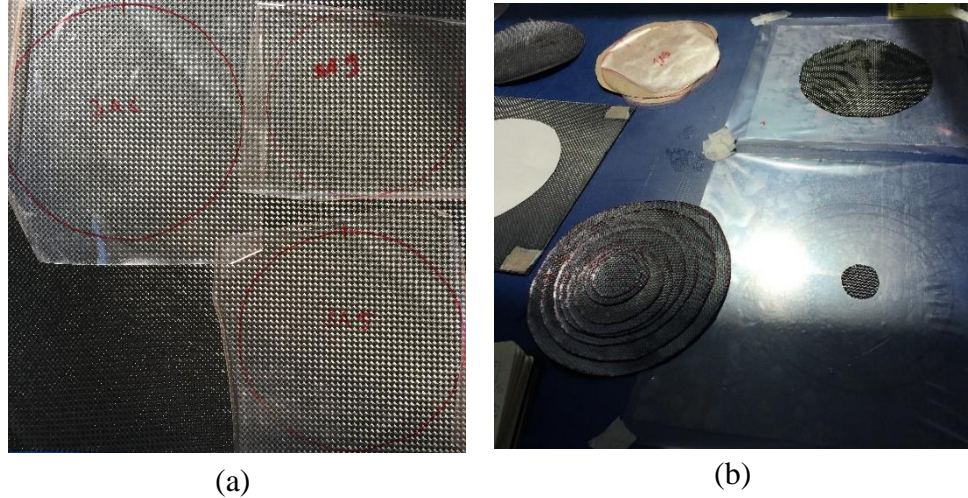


**Figure 4.16** (a) Ply boundaries (b) layup of the repair plies.

Three different systems were employed in this part. Neat composite plates were repaired with neat repair patches (n- prepreg), fiber modified repair patches (f-prepreg) and matrix modified repair patches (m-prepreg). Before curing the repaired plates, the size of the heat blankets and all the other equipment's such as bleeder and breather plies, vacuum probes were specified. The repaired plates were cured on another large sandwich panel. The sandwich panel was covered with a vacuum bag, and glass fiber with the bleeder ply were laid respectively to maintain the air circulation during the cure cycle. Plates were laid over these layers. Thermocouples were placed above the center of the repaired area and around the plates. Another bleeder ply was used for covering the plates. Vacuum bag was again laid on the bleeder ply to protect the heat blankets from any resin leakage. Brisk Heat<sup>®</sup> Silicone Rubber heating blanket was used in this process. Whole system was covered with breather ply and two vacuum probes were placed, completing the vacuum bagging. The curing cycle was 135 minutes at 130°C. Vacuum bagging was detached when the temperature of the vacuum system was cooled to the room temperature.

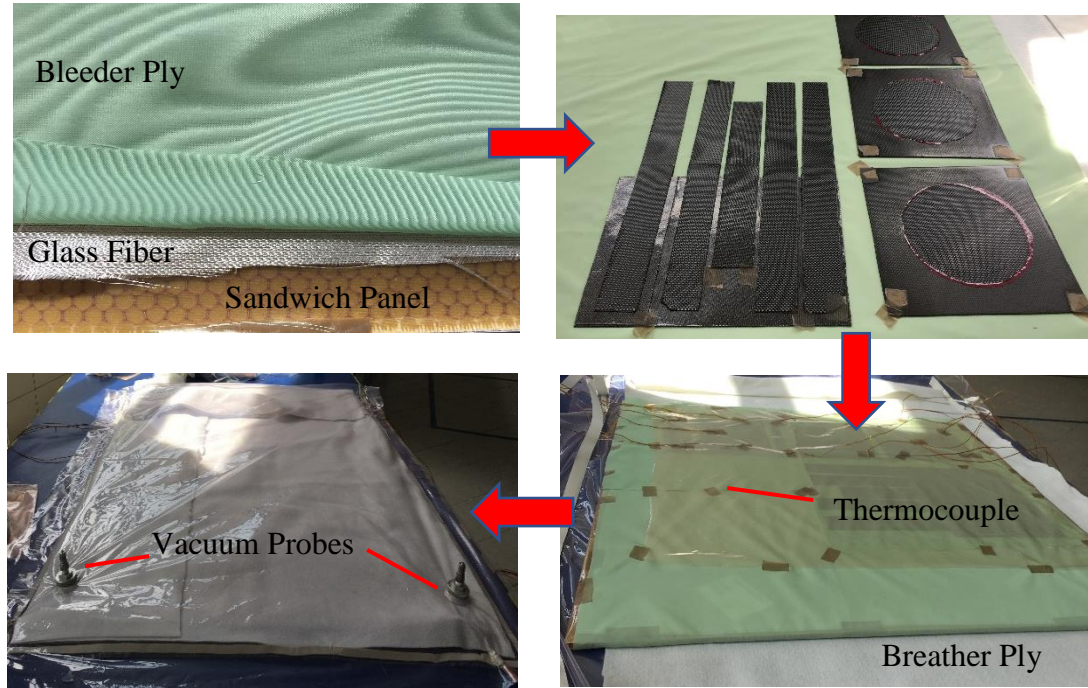


*Figure 4.17* Vacuum bagging steps.

#### 4.4 Mechanical Tests

The first set of specimens includes step and tapered sanding methods to compare the mechanical performances of these two distinct methods with the unrepaired neat specimens. Both groups of tapered and stepped sanded specimens were repaired with n-prepregs to determine the best repair method for the composites.

The unrepaired reference specimens were tested to compare the efficiency of the repairing procedure (i.e. to specify the targeted level of mechanical performance for the repaired composites). The second set includes the tapered neat specimens, which were repaired with both m- and f-prepregs with taper sanding method.

#### 4.4.1 Shear Test

As a first step, shear tests were conducted to investigate the shear properties of the repaired composite materials. Shear test is one of the most common mechanical test methods to define the shear modulus and shear strength of engineering materials. All specimens are prepared and tested according to the ASTM D5379/D5379M -05 standard. The specimens were cut from the plates into 76 mm (length) x 20 mm (width) x 1.8 mm (thickness) dimensions. Two specimens from each group were tested, which were cut from symmetric locations in the repaired plates. To collect the strain data, shear strain gage C2A-06-062LV-350 from Micro – Measurement Company was used. Load was applied by INSTRON 5982 100 kN UTM. Five different composite arrangements were tested with shear test method, namely, (i) the neat composite (reference) samples, neat composite samples repaired with (ii) tapered sanding and (iii) stepped sanding, and composite samples repaired with (iv) m- and (v) f-prepregs. Shear test results for these arrangements are presented in Table 4.3.

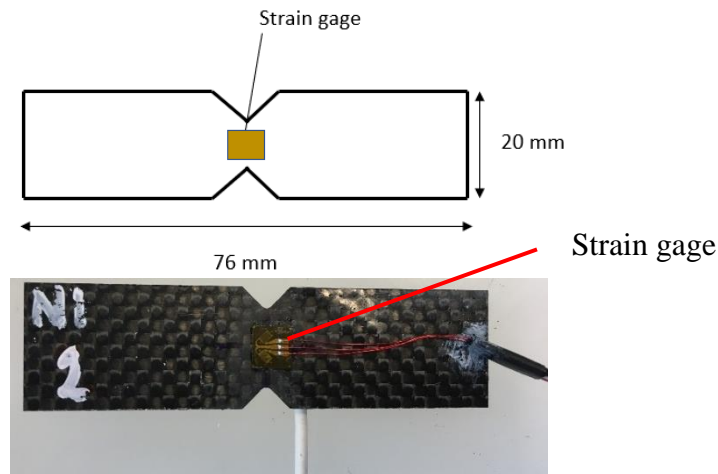


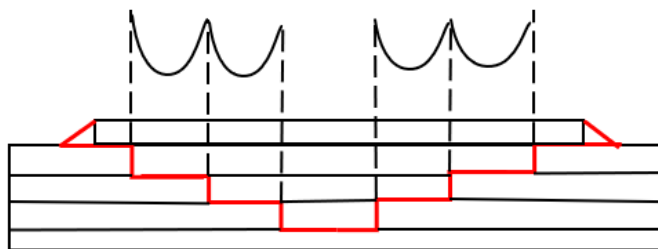
**Figure 4.18** Shear test specimen with strain gage attached on its surface.

As seen in Table 4.3, there is a significant difference especially in the shear modulus values between the tapered sanded and the step sanded neat specimens. The drop in the shear modulus of the neat specimen repaired with stepped sanding is larger than that of tapered sanded sample. Shear moduli of both repair methods for the neat specimen are still lower compared to that of reference sample (13 MPa), however the tapered sanded repair method provides the closest value, therefore it is desirable for the composite repairing processes. The

shear strength levels of neat specimen repaired with the tapered sanded and the step sanded methods are rather close to each other, however tapered sanded neat composite still gives a better value than the stepped sanded sample. At this point it is useful to examine Figure 4.19, in which the shear stress distribution in both stepped and tapered sanded neat samples are shown. In stepped-sanded samples, peak stresses are concentrated on the edges of the stepped repair region [88]. Here the load distribution is carried by the lap joint. For the specimens repaired with tapered sanding, the load is carried by the repaired plies through the composite structure, with a uniform distribution of shear stress through the repair patch. From Table 4.3, there is a 26.8% improvement in shear stress level for the tapered sanding repair method according to the stepped sanding method. It is worth noting that stress concentration areas do not bear high loads, rather act as damage initiation sites or weak points in the structure. Therefore, the specimens repaired with stepped sanding exhibit the lowest shear modulus and strength values.

**Table 4.3** Shear test results.

	<b>Shear Modulus(Mpa)</b>	<b>Max. Load (N)</b>	<b>Shear Strength (Mpa)</b>	<b>Shear Strain (%)</b>
<b>Neat (Reference)</b>	13	3212	145	1.05
<b>Neat Tapered</b>	10	3409	119	1.02
<b>Neat Stepped</b>	5	2957	111	2.09
<b>M-Prepreg Tapered</b>	9	5587	128	1.33
<b>F-Prepreg- Tapered</b>	10	5485	129	1.18



(a)

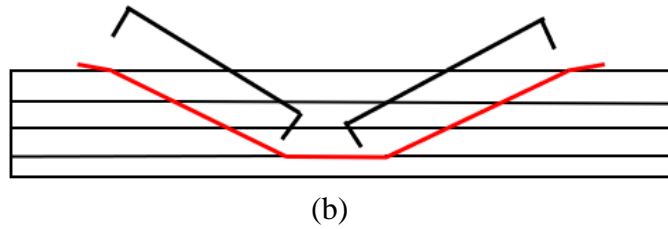


**Figure 4.19** Schematic of the shear stress distributions in (a) stepped sanded repair site, (b) tapered (scarf) sanded repair site.

Furthermore, in both cases of matrix- and interface-modification, the load carrying capacity (max. shear load) was significantly increased due to the TEGO integration. TEGO sheets are known and proven in the previous sections to improve the interfacial bonding of the fibers and the resin material, and to enhance the load distribution in the composite structure. Additionally, using external plies during repair processes made the composite stiffer, which allows the structure to bear more load. Therefore, the load carrying capacity was increased in both repaired samples.

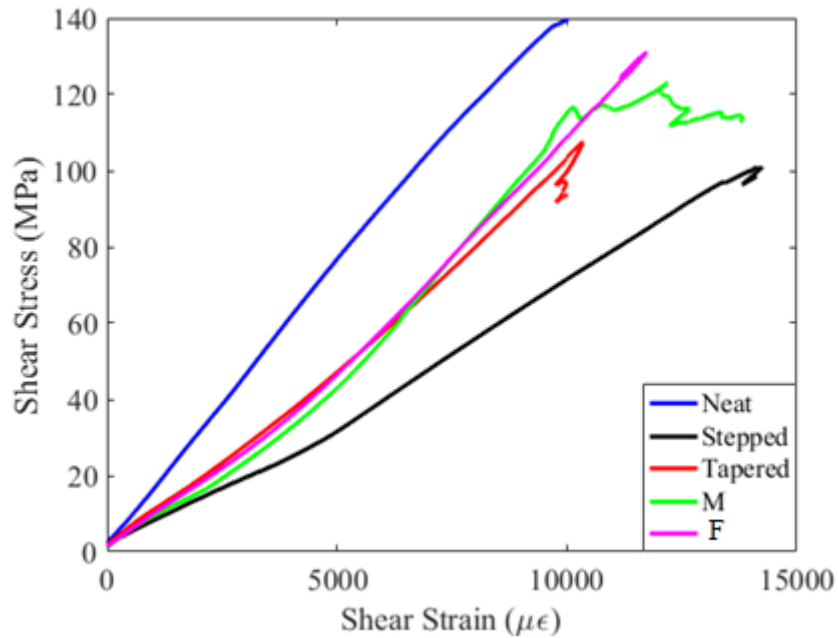


**Figure 4.20** Representative shear stress -strain graph.



Practically, a repaired composite structure can never reach its original mechanical properties before it was damaged. Inspecting the shear stress- strain curves in Figure 4.20, except the stepped-sanded case (shown as black line) and the neat (unrepaired) one, the remaining samples are generally lying within the same range of shear stress values for a specified value of shear strain.

The repaired composite specimens exhibited no true shear failure during the tests. As shown in Figure 4.21, the overall shape and geometry of the specimens remained the same after the shear tests. Only the lateral sections were deformed due to the shear loading.



**Figure 4.21** Damaged test specimens after completing the shear tests.

The fractographic analyses of the shear test specimens revealed that in lateral sections, micro-damages (delamination and fiber breakage) were formed and towards the completion of the tests, micro damages became visible to naked eye on the samples. The detailed optical microscopy images of fracture surfaces for each specimen are given in Figure 4.22.

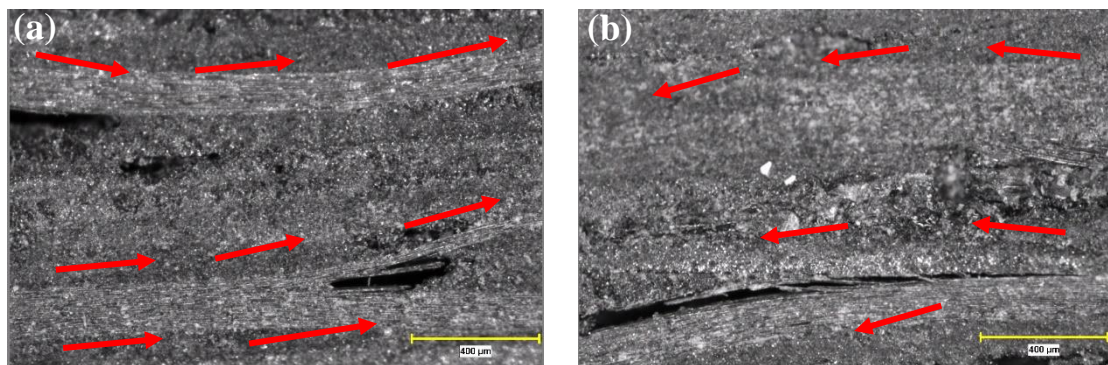


**Figure 4.22** Optical microscope images of the lateral view of (a) m- prepreg tapered (b) f- prepreg tapered specimens.

Delamination governed the failure in both m- prepreg and f- prepreg samples. With shear loading, fiber buckling was obvious in all the damaged specimens. As the load increases, fiber buckling gave rise to delamination and delamination continued until the failure of the specimen.

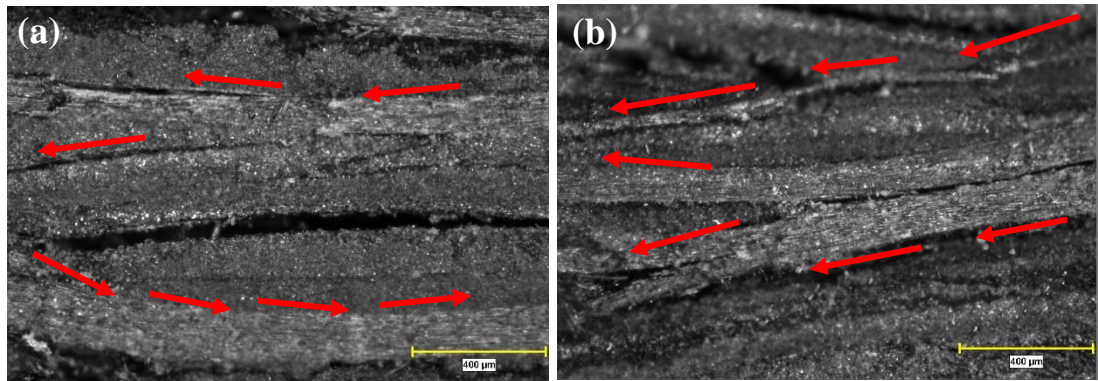


**Figure 4.23** Optical microscope images of lateral view of (a) neat stepped (b) neat tapered specimens.

## Chapter 5

### Conclusions

This study includes three main chapters. The results of each chapter are described in a nutshell as the following.

#### **5.1 Mechanical enhancements in graphene oxide integrated carbon fiber reinforced composites**

Graphene was used as a matrix and an interface modifier in three different arrangements. CFRP/INT arrangement had TEGO as an interface modifier, which improved the bonding between the matrix and carbon fibers. The enhancement of the interface modifier was observed especially in the results of the three-point bending, mode-I fracture toughness, tensile and compression tests. CFRP/MTX system had graphene as a matrix modifier which gave the best results especially in mode-I fracture toughness test with 21.73 % improvement in the fracture toughness values. The last arrangement in which TEGO was used both as an interface and a matrix modifier exhibited reduced mechanical properties in some of the tests. Delamination and fiber breakage were the major failure types that were observed. The important outcome of this work was the change in load transfer mechanisms due to the TEGO reinforcement in the composites for each of the mechanical tests. These findings were supported with the acoustic emission techniques, which helped the damage mechanisms, their order of occurrence and the energy levels for each damage event to be distinguished clearly.



## **5.2 Design of multiple-nozzle electrospray unit**

The design and manufacturing of the multiple-nozzle electrospray unit aimed to develop an automated large-scale system that is adaptable to mass production. As mentioned earlier in this study, electro spraying is a fast, user friendly and low-cost method for nanomaterial coating on the dry fiber preforms which are later to become the reinforcing components of composite materials. The most important parameters in an electro spraying system are the high voltage and the coating rate, which influence the spraying profile thus, the resulting microstructure of the composite greatly. All the required safety precautions including sensors on the cabin panels, ventilating system for the removal of the vaporized chemicals and other necessary infrastructure have been installed in the unit. The new multiple nozzle electro spraying unit will lead the nanomaterial integration in mass production.

## **5.3 Repair of Carbon Fiber Monolithic Plates**

Repair is one of the crucial subjects for composite materials due to their non-recycling characteristic. Proper repairing techniques allow the damaged composite structures to perform safely and durably during their service lives. To enhance the mechanical properties of the repaired composite structure, nanomaterial integrated repair patches were used in this work. First, tapered and stepped sanded specimens were repaired with neat repair patches and the efficiency of the sanding methods were compared. According to the shear tests, there was a 48% difference in shear moduli of the tapered- and stepped-sanded specimens. Thus, tapered sanding was regarded as the best method which exhibited mechanical properties closest to the unrepaired specimens, and was employed to repair the composite samples for the rest of the study. Secondly, TEGO integration was employed in two different group of specimens. First group included the matrix reinforcement by adding TEGO sheets into the resin system of the composite. The second one was the integration of TEGO in the dry fibers by using electro spraying method. As expected, the effect of the interface modification was dominant in the shear tests, surpassing the maximum shear load value of the neat tapered sanded samples.

To conclude, nanomaterial-integrated repair patches will potentially bring a novel perspective to the repair methods of composite materials. The use and effects of TEGO as an interface and a matrix modifier was successfully examined. The obtained promising results in using nanomaterial integrated repair patches will lead to new developments in the application areas of composites, such as aerospace, renewable energy and defense industries.

## Bibliography

- [1] Yazyev, O. V. and Chen, Y. P., *Nat. Nanotechnol.*, (2014), 9, 755– 767.
- [2] Gopinath, A., Kumar, M.S., Erayaperumal, A., Experimental Investigations on Mechanical Properties of Jute Fiber Reinforced Composites with Polyester and Epoxy Resin Matrices, *Procedia Engineering* 97(0) (2014) 2052-2063.
- [3] Hine, P.J., Bonner, M., Ward, I.M., Y. Swolfs, Y., Verpoest, I., Mierzwa, A., Hybrid carbon fibre/ nylon12 single polymer composites, *Composites Part A: Applied Science and Manufacturing* 65(0) (2014) 19-26.
- [4] Young, R. J., Kinloch, I. A., Gong, L., & Novoselov, K. S. The mechanics of graphene nanocomposites: A review. *Composites Science and Technology*, 72(12), (2012) 1459-1476.
- [5] Mittal, G., Dhand, V., Rhee, K. Y., Park, S. J., and Lee, W. R., *J. Ind. Eng. Chem.*, (2015), 21, 11–25.
- [6] Li, D., Müller, M. B., Gilje, S., Kaner, R. B. & Wallace, G. G. Processable aqueous dispersions of graphene nanosheets. *Nat. Nano technol.* (2008) 3, 101–105.
- [7] Zhou, X. S. et al. Dispersion of graphene sheets in ionic liquid stabilized by an ionic liquid polymer. *Chem. Commun.* (2010), 46, 386–388.
- [8] Fang, M., Wang, K. G., Lu, H. B., Yang, Y. L. & Nutt, S. Covalent polymer functionalization of graphene nanosheets and mechanical properties of composites. *J. Mater. Chem.* (2009) 19, 7098–7105.
- [9] Katnam, K.B, Comer, A.J., Roy, D., Da Silva, L. F. M, and Young, T. M., Composite Repair in Wind turbine Blades: An Overview, *The journal of Adhesion*, (2015) 91:113 -139.
- [10] Gassan, J., A study of fiber and interface parameters affecting the fatigue behavior of natural fiber composites, *Composites Part A: Applied Science and Manufacturing* 33(3) (2002) 369-374.
- [11] Song, W., Gu, A., Liang, G., Yuan, L., Effect of the surface roughness on interfacial properties of carbon fiber reinforced epoxy resin composites, *Applied Surface Science* 257(9) (2011) 4069-4074.
- [12] Fitzer, E., Geigl, K.H., Hüttner, W., Weiss, R, Chemical interactions between carbon fiber surface and epoxy resins, *Carbon* 18(6) (1980) 389-393.
- [13] Novoselov, K. S., Geim, A. K., Morozov, S. V., Jiang, D., Zhang, Y., Dubonos, S. V., Grigorieva, I. V., and Firsov, A. A., *Science*, (2004), 306, 666–669.

- [14] M. D. Stoller, S. Park, Y. Zhu, J. An and R. S. Ruoff, *Nano Lett.*, (2008), 8, 3498–3502.
- [15] C. Lee, X. D. Wei, J. W. Kysar and J. Hone, *Science*, (2008), 321, 385–388.
- [16] A. A. Balandin, S. Ghosh, W. Bao, I. Calizo, D. Teweldebrhan, F. Miao and C. N. Lau, *Nano Lett.*, (2008), 8, 902–907.
- [17] Saner, B., Okyay, F., and Yurum, Y., Utilization of multiple graphene layers in fuel cells 1. An improved technique for the exfoliation of graphene- based nanosheets from graphite, *Fuel*, 89(8) (2010), 1903–1910.
- [18] Poudeh, L.H, Okan, B.S, Zanjani J.S.M, Yildiz, M. and Menciloglu, Y. Z., *RSC Adv.*, (2015), 5(111), 91147–91157.
- [19] Liu X., Boddeti, N. G., Szpunar, M. R. , Wang, L., Rodriguez, M. A., Xiao, R. Long, J., Dunn, M. L. and Bunch, J. S. ,*Nano Lett.*, (2013), 13, 2309–2313.
- [20] Demircan O, Ashibe S, Kosui T, et al. Mechanical properties of biaxial weft-knitted and cross-ply thermoplastic composites. *J Thermoplast Compos Mater* (2014)
- [21] Almond, D. P. and Peng, W., *J. Microsc.* 201, (2001), 163–170.
- [22] Avdelidis, N. P., Almond, D. P., Dobbins, A., Hawtin, B. C., Castaneda, C. I., and Maldague, X., *Prog. Aerosp. Sci.* 40, (2004), 143–162.
- [23] Avdelidis, N. P., Hawtin, B. C., and Almond, D. P., *NDT & E Int.* 36, (2003) 433–439
- [24] 1. ASTM E 1316, 2002, Standard Terminology for NDT.
- [25] EN 1330-9, 2000, Terms Used in AE Testing.
- [26] Randviir, Edward P. Dale A.C. Brownson and Craig E. Banks, *Materials Today*, (2014) Volume 17, Number 9.
- [27] Novoselov, K.S. et al. *Proc. Natl. Acad. Sci. U. S. A.* 102 (2005) 10451.
- [28] Bai, H. Li, C. and Shi, G. *Adv. Mater.*, (2011), 23, 1089–1115.
- [29] Zhao, X. et al. *Adv. Energy Mater.* 1 (6) (2011) 1079.
- [30] Wang, H. et al. *Angew. Chem. Int. Ed.* 52 (35) (2013) 9210.
- [31] Cooper, D. R., D'Anjou, B., Ghattamaneni, N., Harack, B., Hilke, M., Horth, A., Majlis, N., Massicotte, M., Vandsburger, L., Whiteway, E. and Yu, V., *ISRN Condens. Matter Phys.*, (2012), 1–56.
- [32] Pu, N.W., Peng, Y.Y., Wang, P.C., Chen, C.Y., Shi, J.-N., Liu, Y.M., Ger, M.D.; Chang, C.L. Application of nitrogen-doped graphene nanosheets in electrically conductive adhesives. *Carbon* (2014), 67, 449–456.

- [33] Hertzberg, Richard W. *Deformation and Fracture Mechanics of Engineering Materials* (4th ed.). Wiley. (1995).
- [34] Todd M. Mower, Victor C. Li., Fracture characterization of random short fiber reinforced thermoset resin composites, *Engineering Fracture Mechanics*. 26(4): (1987). 593-603
- [35] C.K.H Dharan, Fracture mechanics of composite materials, *Journal of engineering materials and technology*. 100, (1978). 223-247
- [36] M.G. R Sause, T. Müller, A. Horoschenkoff, S. Horn, *Compos. Sci. Technol.*, 72 (2012) 167-174.
- [37] Li, M.; Gu, Y.; Liu, Y.; Li, Y.; Zhang, Z. Interfacial improvement of carbon fiber/epoxy composites using a simple process for depositing commercially functionalized carbon nanotubes on the fibers. *Carbon* (2013), 52, 109–121.
- [38] Gretchen B. Murri, Effect of Data Reduction and Fiber-Bridging on Mode I Delamination Characterization of Unidirectional Composites Article Information (2015), 48, 2413-2424
- [39] EN 6033 STANDARD
- [40] Shojaee, S.A.; Zandiatashbar, A.; Koratkar, N.; Lucca, D.A. Raman spectroscopic imaging of graphene dispersion in polymer composites. *Carbon* (2013), 62, 510–513.
- [41] Rodbari R.J., Wendelbo R, Jamshidi L.C.L.A, Hernández E.P., Nascimento L. Study of Physical and Chemical Characterization of Nanocomposite Polystyrene / Graphene Oxide High Acidity Can Be Applied in Thin Films. *J. Chil. Chem. Soc.*, 61, (2016), (3).
- [42] Lee, D.; Zou, X.; Zhu, X.; Seo, J.W.; Cole, J.M.; Bondino, F.; Magnano, E.; Nair, S. K.; Su, H. Ultrafast carrier phonon dynamics in NaOH-reacted graphite oxide film. *Appl. Phys. Lett.* (2012).
- [43] ASTM D3039/D3039M-00. Standard test method for tensile properties of polymer matrix composite materials. American Society for Testing Materials. [CD-ROM]; 2004.
- [44] Zanjani J.S.M, Okan B.S, Menciloglu Y.Z, Yildiz M., Nano-engineered design and manufacturing of high-performance epoxy matrix composites with carbon fiber/selectively integrated graphene as multi-scale reinforcements, *RSC Adv.*, (2016), 6, 9495-9506
- [45] Li, Z. et al. Enhanced dislocation obstruction in nano laminated graphene/Cu composite as revealed by stress relaxation experiments. *Scripta Materialia* (2017) 131, 67–71.
- [46] Yan, Y., Zhou, S. & Liu, S. Atomistic simulation on nanomechanical response of indented graphene/nickel system. *Computational Materials Science* 130, 16–20 (2017).

- [47] Muller, S. E. & Nair, A. K. Dislocation Nucleation in Nickel-Graphene Nanocomposites Under Mode I Loading. *Jom* 68, 1909–1914(2016).
- [48] Liu, X. Y., Wang, F. C., Wu, H. A. & Wang, W. Q. Strengthening metal nanolaminates under shock compression through dual effect of strong and weak graphene interface. *Applied Physics Letters* 104 (2014).
- [49] Long, X. J. et al. Shock response of Cu/graphene nanolayered composites. *Carbon* 103, 457–463 (2016).
- [50] Rezaei, R., Deng, C., Tavakoli-Anbaran, H. & Shariati, M. Deformation twinning-mediated pseudo elasticity in metal–graphene nanolayered membrane. *Philosophical Magazine Letters* 96, 322–329 (2016).
- [51] Yang, Z., Wang, D., Lu, Z. & Hu, W. Atomistic simulation on the plastic deformation and fracture of bio-inspired graphene/Ni nanocomposites. *Applied Physics Letters* 109, 191909 (2016).
- [52] He, Y. et al. Tensile mechanical properties of nano-layered copper/graphene composite. *Physica E: Low-dimensional Systems and Nanostructures* 87, 233–236 (2017).
- [53] Rosen, B.W. Mechanics of composite strengthening. In *American Society for Metals: Seminar on Fiber Composite Materials*; American Society for Metals (ASM): Philadelphia, PA, USA, (1964), 37–75.
- [54] Liebig, W.V.; Leopold, C.; Schulte, K. Photoelastic study of stresses in the vicinity of a unique void in a fibre-reinforced model composite under compression. *Compos. Sci. Technol.* (2013), 84, 72–77.
- [55] Liebig, W.V.; Schulte, K.; Fiedler, B. Hierarchical analysis of the degradation of fiber-reinforced polymers under the presence of void imperfections. *Philos. Trans. Ser. A Math. Phys. Eng. Sci.* (2016), 374, 20150279.
- [56] Shams, S.S.; Elhajjar, R.F. Investigation into the effects of fiber waviness in standard notched composite specimens. *CEAS Aeronaut. J.* (2015), 6, 541–555.
- [57] Mittelstedt, C.; Becker, W. Free-Edge Effects in Composite Laminates. *Appl. Mech. Rev.* (2007), 60, 217–245.
- [58] Greenhalgh, E.S.; Rogers, C.; Robinson, P. Fractographic observations on delamination growth and the subsequent migration through the laminate. *Compos. Sci. Technol.* (2009), 69, 2345–2351.
- [59] Leopold C.; Schütt M.; Liebig W.V.; Philipkowski T.; Kürten J.; Schulte K.; Fiedler B. Compression Fracture of CFRP Laminates Containing Stress Intensifications *Materials* (2017), 10, 1039.

- [60] Zaimova D, Bayraktar E, Miskioglu I, Katundi D, Dishovsky N. Manufacturing of New Elastomeric Composites: Mechanical Properties, Chemical and Physical Analysis. In: Tandon G, editor. Composite, Hybrid, and Multifunctional Materials, Volume 4. Springer International Publishing; (2015), 139–50.
- [61] Bayraktar E, Zaimova D, Tan MJ, Miskioglu I. Design of Multifunctional Energetic Structural Composites: A Preliminary Study on an Epoxy-Rubber Matrix with Exothermic Mixture Reinforcements. *Experimental Mechanics of Composite, Hybrid, and Multifunctional Materials*, Volume 6. Springer International Publishing; (2014), 47–56
- [62] Xu, Y., Chung, D.D.L., Mroz, C., Thermally conducting aluminum nitride polymer-matrix composites. *Composites Part A: Applied science and manufacturing*. (2001); 32(12):1749–1757.
- [63] Ramajo, L.A, Reboredo, M.M, Castro,M.S. Characterization of epoxy/BaTiO<sub>3</sub> composites processed by dipping for integral capacitor films (ICF). *Journal of Materials Science*, (2007);42(10):3685–3691.
- [64] Bayraktar E, Miskioglu I, Zaimova D. Low-Cost Production of Epoxy Matrix Composites Reinforced with Scrap Rubber, Boron, Glass Bubbles and Alumina. In: *Mechanics of Composite and Multi-Functional Materials*, Volume 7. Springer; (2016); 163–172.
- [65] Menard KP. *Dynamic Mechanical Analysis: A Practical Introduction*, Second Edition. CRC Press; (2008), 240
- [66] Zaimova D, Bayraktar E, Miskioglu I, Katundi D, Dishovsky N. New Design of Composite Materials Based on Scrap Rubber Matrix Reinforced with Epoxy and SiC. In: *Advanced Materials Research*. Trans Tech Publ; (2014); 114–121.
- [67] Wernik JM, Meguid SA. Multiscale modeling of the nonlinear response of nano-reinforced polymers. *Acta Mechanica*. (2011) ;217(1–2):1–16
- [68] Martin M, Hanagud S, Thadhani NN. Mechanical behavior of nickel + aluminum powder-reinforced epoxy composites, *Materials Science and Engineering: A*. (2007);443(1):209–218.
- [69] Bai Y, Cheng Z-Y, Bharti V, Xu HS, Zhang QM. High-dielectric-constant ceramic-powder polymer composites. *Applied Physics Letters*. (2000); 76(25):3804–3806.
- [70] Zaimova D, Bayraktar E, Berthout G, Dishovsky N. Design of New Elastomeric Matrix Composites: Comparison of Mechanical Properties and Determining Viscoelastic Parameters via Continuous Micro Indentation. In: Patterson E, Backman D, Cloud G, editors. *Composite Materials and Joining Technologies for Composites*, Volume 7. Springer New York; (2013); 227–34.

- [71] Zaimova D, Bayraktar E, Tan MJ, Miskioglu I. Processing of Epoxy-Nickel Matrix Composites Reinforced with Aluminum and Waste Elastomers. *Advanced Materials Research*. 2014 ;(939). 496 A.B. Irez et al. / *Procedia Engineering* 184 ( 2017 ) 486 – 496.
- [72] Donghua K, Chienchih C. Dielectric Behaviours of Multi-doped BaTiO<sub>3</sub>/Epoxy Composites. *Journal of the European Ceramic Society*. (2001); 21(9):1171–1177.
- [73] Greenhalgh E., *Failure Analysis and Fractography of Polymer Composites*, A volume in Woodhead Publishing Series in Composites Science and Engineering, (2009); 164–237
- [74] Y. Zhang, J. Stringer, P.J. Smith, A. Hodzic and R. Grainger, Toughening Composites with Self-ameliorating Capability Using Inkjet Printing Technique. *Eccm16 - 16th European Conference on Composite Materials*, (2014)
- [75] He, J.; Xu, F.; Cao, Y., Liu, Y. Electrohydrodynamic direct-writing lithography: An alternative maskless technique for microstructure fabrication. *Appl. Phys. Lett.* (2014), 105, 5722–5726.
- [76] Rayleigh, L. On the equilibrium of liquid conducting masses charged with electricity. *Phil. Mag. Ser. 5* (1882), 14, 184-186.
- [77] Zeleny, J. The electrical discharge from liquid points, and a hydrostatic method of measuring the electric intensity at their surfaces. *Phys. Rev.* (1914), 3, 69-91.
- [78] Taylor, G. Disintegration of water drops in an electric field. *Proc. Roy. Soc. London Ser. A Math. Phys. Sci.* (1964), 280, 383-397.
- [79] Sridhar, R., Lakshminarayanan, R.; Madhaiyan, K., Amutha Barathi, V., Lim, K.H, Ramakrishna, S. Electrospayed nanoparticles and electrospun nanofibers based on natural materials: Applications in tissue regeneration, drug delivery and pharmaceuticals. *Chem. Soc. Rev.* (2015), 44, 790–814.
- [80] Olvera-Trejo, D., Velásquez-García, L.F. Additively manufactured mems multiplexed coaxial electrospay sources for high-throughput, uniform generation of core-shell microparticles. *Lab Chip* (2016), 16, 4121–4132.
- [81] Zheng, G., Zhu, P.; Sun, L., Jiang, J., Liu, J., Wang, X., Li, W. Thin film zinc oxide gas sensor fabricated using near-field electrospay. *AIP Adv.*(2016), 6, 125306.
- [82] Xie, J., Kuang, L., Phua, Y., Hua, J., Wang, C.-H. Electrohydrodynamic atomization for biodegradable polymeric particle production. *J. Colloid Interface Sci.* (2006), 302, 103–112.
- [83] Bock, N., Woodruff, M.A., Hutmacher, D.W., Dargaville, T., *Electrospraying, a Reproducible Method for Production of Polymeric Microspheres for Biomedical Applications* *Polymers* ( 2011), 3, 131-149.



[84] Hull D., An introduction to composite materials. Cambridge University Press, Cambridge, (1987).

[85] Hou, W.G, Zhang,W.F, Ding, M.L, Liu X, Wang, Z.R, Thermal deplying technology of damaged area in carbon fiber/bismaleimide resin laminates. The proceedings of 2010 Asia-Pacific international symposium on aerospace technology, vol.2, (2010) 865-868.

[86] Wang, C.H, Gunnion A.J, On the design methodology of scarf repairs to composite laminates. *Comp. Sci. Technol.* 68(1):35-36.

[87] Baig, Y., Cheng, X., Hasham, H.J., Abbas,M., Khan,W.A., Failure mechanisms of scarf-repaired composite laminates under tensile load, *J. Braz. Soc. Mech. Sci. Eng.* (2016) 38:2069-2075.

[88] Dorworth, L.C, Gardiner, G.L. , Mellema, G.M., Essentials of Advanced Composite Fabrication and Repair, Aviation Supplies & Academics, Inc. (2009).

[89] Melin LN, Neumeister JM. Measuring constitutive shear behavior of orthotropic composites and evaluation of the modified Iosipescu test. *Composite Structure* (2006); 76:106–15.

[90] Ratwani. M.M, Repair Types, Procedures – Part I, RTO-EN-AVT-156.

[91] Yilmaz C., Akalin, C. , Gunal, I., Celik, H., Buyuk, M., Suleman, A. Yildiz, M., A hybrid damage assessment for E-and S-glass reinforced laminated composite structures under in-plane shear loading, *Composite Structures* 186 (2018) 347–354.

[92] Yilmaz, C. , Akalin, C. Kocaman, E.S., Suleman, A. Yildiz, M., Monitoring Poisson's ratio of glass fiber reinforced composites as damage index using biaxial Fiber Bragg Grating sensors, *Polymer Testing* 53 (2016) 98-107.

[93] Baere, I.D., Van Paepegem,W., Degrieck, J., On the nonlinear evolution of the Poisson's ratio under quasi-static loading for a carbon fabric-reinforced thermoplastic. Part I: influence of the transverse strain sensor, *Polym. Test.* 28 (2009) 196-203.

[94] Yilmaz C., Yildiz, M., A study on correlating reduction in Poisson's ratio with transverse crack and delamination through acoustic emission signals. *Polymer Testing* 63 (2017) 47- 53.

[95] Liang J., Huang Y., Zhang L., Wang Y., Ma Y., Guo T., Chen Y., “Molecular-Level Dispersion of Graphene into Poly(vinyl alcohol) and Effective Reinforcement of their Nanocomposites”, *Advanced Functional Materials*, 2009, 19, 2297–2302.

[96] Liu L.Q., Barber A.H., Nuriel S., Wagner H.D., “Mechanical Properties of Functionalized Single-Walled Carbon-Nanotube/Poly(vinyl alcohol) Nanocomposites”, *Advanced Functional Materials* 2005, 15, 975.

[97] Ramanathan T., Abdala A.A., Stankovich S., Dikin D.A., Herrera-Alonso M., Piner R.D., Adamson D.H., Schniepp H.C., Chen X., Ruoff R.S., Nguyen S.T., Aksay I.A.,

Prud'homme R.K., Brinson L.C., "Functionalized graphene sheets for polymer nanocomposites", *Nature Nanotechnology* 2008, 3, 327.

[98] Pierre Le Parlouër, *Thermal Analysis and Calorimetry Techniques for Catalytic Investigations Calorimetry and Thermal Methods in Catalysis*. Springer-Verlag Berlin Heidelberg 2013.